UNIVERSIDAD DE CHILE
FACULTAD DE CIENCIAS FÍSICAS Y MATEMÁTICAS
DEPARTAMENTO DE GEOLOGÍA

PRESSURE-TEMPERATURE-TIME PATHS OF THE LIMÓN VERDE METAMORPHIC COMPLEX, CHILE

TESIS PARA OPTAR AL GRADO DE MAGISTER EN CIENCIAS, MENCIÓN GEOLOGÍA

MARÍA FERNANDA SOTO VERDUGO

PROFESOR GUÍA:
FRANCISCO HERVÉ ALLAMAND

MIEMBROS DE LA COMISIÓN:
MAURICIO CALDERÓN NETTLE
KATJA DECKART
CONSTANTINO MPODOZIS MARÍN

SANTIAGO, CHILE
JUNIO, 2013

Abstract

The Paleozoic basement in the Central Andes has been a subject of study in order to determine the tectonodynamic history of the western margin of South América. Particularly, the metamorphic basement has been of interest since it is associated to distinct episodes of crustal recycling and, to a lesser extent, the basement is often associated to the accretion of juvenile material during the Terra Australis orogeny between 900-250 Ma. The metamorphic basement in Northern Chile crops out in north-south stripes of land, which have been infered as allochtonous terrane boundaries by previous authors. The Sierra Limón Verde is one of this north-south stripes of land, and it is part of the Cordillera de Domeyko structural domain. The Paleozoic basement of the Sierra comprises Carboniferous igneous rocks and Permian metamorphic rocks, the latter from the Limón Verde Metamorphic Complex.

The Limón Verde Metamorphic Complex (LVMC) consists of a series of outcrops in a 12x2 km NNE stripe, located nor-west of the Sierra Limón Verde. These are strongly foliated garnet-mica schists, amphibolites, and subordinated quartzites. Whole rock geochemistry analyses show a within plate basalt protolith for the amphibolite, and a psamopelitic protolith for the mica schists reinforced by the appearance of detrital zircon with different provenance, with the youngest depositional age of 300 Ma, this age is similar to late stage magmatism of the Limón Verde Igneous Complex. Nd-depleted mantle model ages are TDM=1.6 Ga for the mica schist and TDM =0.86 Ga for the amphibolite, results consistent with the literature for northern Chile for felsic rocks and basalts respectively. Both rock types seem to have suffered crustal recycling processes.

The rocks from the LVMC show a clockwise path of metamorphism consistent with a subduction zone setting. The peak metamorphim of mica schist (P,T) was achieved in wet (ca. and above 5% H2O) conditions at ca. 280 Ma. according to U-Pb zircon ages. This is shown by textures of anatexis in some areas of the rock, and also in the REE patterns in zircon. Plus, it is reinforced by the PT realm of metamorphism modeled in the pseudosections at 14.5 kbar and ca. 600^oC, reaching to a max. temperature of ca. 650^oC. This is interpreted to be a depth of formation ca. 50 kms. The peak metamorphic conditions of the amphibolite (P,T) were achieved also in wet conditions ca. 5% H2O and with high values of oxygen fugacity averaging $0.11\%O_2$. The metamorphic peak of these samples is at a lower pressure (11.5 kbar), but similar temperature (650^oC) than the mica schist. Which is interpreted to a depth of formation of ca. 40 kms. On the other hand, the age of metamorphism is ca. 260 Ma (U-Pb in titanite and Ar-Ar in hornblende).

Step heating Ar-Ar dating of white micas (ca. 263 Ma) and biotite (ca. 251 Ma) from the mica schist were used to determine cooling rates. Two steps were determined: $11.4 \pm 3.47^oC/My$ for the first step (U-Pb in zircon to Ar-Ar in white mica) and $4.16 \pm 5.03^oC/My$ for a second (Ar-Ar in white mica to Ar-Ar in biotite). Considering the geothermal gradient of a normal continental crust (Ernst, 2009) of $25^oC/km$, the estimated exhumation rates of 0.45 mm/yr and 0.16 mm/yr respectively. Considering clossure temperatures and a normal geothermal gradient, then a fast exhumation may have taken place. A few km. south of these outcrops, Triassic sedimentary units (Agua Dulce Fm.) contain clasts of garnet mica schist, that were part of the LVMC, suggesting that the rocks from the complex were completely exhumed by the mid-Triassic.

RESUMEN DE LA TESIS PARA OPTAR AL GRADO DE: Magíster en Ciencias m/ Geología.

POR: María Fernanda Soto Verdugo

FECHA: 10/06/2013

PROFESOR GUIA: Francisco Hervé Allamand

Trayectorias Presión-Temperatura-tiempo del Complejo Metamórfico Limón Verde, Chile.

El basamento Paleozoico (Pz) de los Andes Centrales ha sido objeto de estudio con el fin de determinar la historia tectonodinámica del márgen occidental de Sudamérica. En el norte de Chile, el basamento aflora en franjas N-S, de las que algunos autores han sugerido como bordes de terrenos alóctonos acrecionados al márgen occidental de Gondwana. La Sierra Limón Verde es una de estas franjas N-S, la cuál es parte de la Cordillera de Domeyko. El basamento Pz de la Sierra comprende rocas Carboníferas intrusivas del Complejo Igneo Limón Verde y rocas metamórficas Pérmicas. El Complejo Metamórfico Limón Verde (CMLV) comprende afloramientos en una franja NNE de 12x2 km ubicada al nor-oeste de la Sierra. Estas rocas consisten en esquistos micáceos y anfibolitas foliadas, además de cuarcitas subordinadas. Análisis de geoquímica en roca total en anfibolita indican como protolito a basaltos con afinidad de intra-placa, y a sedimentos psamopelíticos al protolito de los esquistos micáceos. Circones detríticos que presentan distintas proveniencias reafirman la naturaleza sedimentaria de los esquistos, con una edad mínima de depositación de 300 Ma. Esta edad es similar al la del magmatismo tardío del Complejo Igneo Limón Verde.

Las rocas del CMLV presentan una trayectoria horaria prógrada consistente con un ambiente de subducción. El peak metamórfico del mica esquisto (PT) fue obtenido en condiciones acuosas (ca. $5\%H_2O$) a los ca. 280 Ma (U-Pb en circón). Esto se observa como anatexis en ciertas partes de la roca y también en los diagramas de REE de bordes de circón. El campo PT modelado a través de pseudosecciones indica 14.5 kbar y 600^{o}C, llegando a una temperatura máxima de 650^{o}C, lo que se interpreta como una profundidad de formación cercana a los 50 kms. El peak metamórfico de la unidad de anfibolita también fue formado en condiciones acuosas y de alta fugacidad de oxígeno ($0.11\%O_2$) ,el que se obtuvo a menor presión (11.5 kbar) pero a temperaturas similares a las del esquisto (ca. 650^{o}C), lo que es interpretado como una profundidad cercana a los 40 kms. Por otro lado, la edad del metamorfismo es cercana a los 260 Ma (U-Pb en titanita y Ar-Ar en hornblenda).

Edades plateau Ar-Ar en mica blanca (ca. 263 Ma) y biotita (ca. 251 Ma) provenientes de un mica esquisto fueron utilizadas para determinar tasas de enfriamiento, los que se hicieron en dos pasos: $11.4 \pm 3.47^oC/My$ para el primer paso (U-Pb en circón a Ar-Ar en mica blanca) y $4.16 \pm 5.03^oC/My$ para el segundo (Ar-Ar mica blanca a Ar-Ar biotita). Al considerar un gradiente geotermal de una corteza normal de $25^oC/km$ (Ernst, 2009) se estimaron tasas de enfriamiento de 0.45 mm/yr y 0.16 mm/yr para el primer y segundo paso respectivamente. Al tomar en cuenta las temperaturas de cierre de estos sistemas y un gradiente geotérmico normal, debe de haber ocurrido una exhumación rápida. Al sur del CMLV existen unidades sedimentarias triásicas que contienen clastos de mica esquistos de granate del CMLV (Fm. Agua Dulce), sugiriendo que las rocas del complejo metamórfico se encontraban completamente exhumadas ya en el Triásico medio.

Dedicado a mis padres,

los de Chile...

y los de Canadá.

Agradecimientos

Primero me gustaría agradecer a los miembros de mi comisión Pancho, Caldera, Katja, Cocho; no sólo por su guía y paciencia, sino por ser un equipo. Ha sido muy importante y muy gratificante trabajar con ustedes. Quizás haya sido un poco regalona y/o patuda en ese sentido (además de peleadora) pero me encanta poder tener esa confianza con ustedes, y que me hayan tratado como colega sabiendo que ustedes son tan grandes!. Agradezco al proyecto FONDECYT #1095099 por financiar terrenos, análisis, congresos de este trabajo y por juntar a gente tan genial.

Estoy muy agradecida al programa de colaboración científica BMBF-CONICYT #175 − 2009 entre la U. de Chile y la U. de Stuttgart por la oportunidad de haber podido trabajar con expertos en temas tan abstractos y sutiles como el *forward modeling of PTX pseudosections*. Hans Massonne, Thomas Theye thank you so much for guiding me into the beautiful and chaotic world of mineralogy and thermodynamics. Thank you for your kindness and hospitality. Thanks also to Dr. Opitz.

Thanks a lot to Mark Fanning for providing most of the geochronology data and being approchable, Id also like to thank to Dr. Robert Pankhurst for reviewing part of this manuscript and providing helpful comments. Muchas gracias a Andy Tomlinson y Paul Duhart del SERNAGEOMIN por colaborar y financiar dataciones Ar-Ar para el CMLV, correspondientes a las Hojas Sierra Gorda y Moctezuma del Plan Nacional.

Tambien agradezco a Arne Willner, Estanislao Godoy, Fernando Barra y Diego Morata por hacer preguntas difíciles las que me ayudaron a crecer como investigadora y como persona. A veces se requiere de la pregunta apropiada en el momento apropiado. Muchisimas gracias a mis amigos y colegas piedrólogos: J. Alvarez, P. Molina y J. Navarro. Por su apoyo, cariño, discusiones productivas, y porque tuvieron la paciencia para escucharme alegar acerca de *Perple*χ en más de alguna ocasión. También gracias a Javiera Morandé por colaborar con datos, conversaciones, e ideas para la evolución de la Sierra Limón Verde.

Gracias a todos quienes me han acompañado en estos años de MSc. A la gente que me apoyó en los buenos momentos y tuvo que soportarme en los momentos de desamor, estoy infinitamente agradecida. Ahora al comenzar este nuevo capítulo de mi vida, estoy contenta de haber conocido gente fantástica, me voy con una grata sensación, y es porque ustedes, mis amigos han estado ahi: en lo bueno, en lo malo y en lo feo. A mis amigas hermosas: Susy, Alida, Cata, Valito, Coni; a mis monos queridos: Andrés, Fofito, Palmera, Payacuento, Quirogro, Atax, Pelao; a los no tan monos: Sebi, Basq, Ore, Peibl, Palape y a mis compaeros de aventuras desde la Cordillera al Mar: Lea, Raulí, Roberto, también a Cindy por darme muchos abrazos y hacerme reir, y a mis amigos que están lejos: Felix y Yasna, los quiero mucho!

Cómo olvidar a Maritza, Blanca, María Rosa, Vero, Quilo, y a Don José: gracias por estar ahí, por ayudarme y regalarme un buenos días. También muchas gracias a Juanito y a Roberto por dejarme meter mano en el laboratorio su excelente disposición.

Finalmente, fue gracias a H. Ugalde y a M. Pardo, quienes me incentivaron a hacer un magíster en Chile y me pusieron en contacto con quién sería mi sensei. Pancho: no sólo has sido mi profesor guía, has sido un amigo y un maestro... admiro tu empatía, tu optimismo, y tu capacidad de ver lo mejor en cada persona. Ojalá sigamos trabajando juntos en un futuro (quizás no tan lejano). Muchas gracias por todo.

Contents

Chapter 1

Introduction

The tectonodynamic history of a metamorphic complex formed during an orogeny, or in an orogenic belt, is the ultimate goal of studying crustal recycling and accretionary processes, the history can be built through continuous (or discrete) metamorphic events recorded in the rocks belonging to the afforsaid complex. There exist two different types of orogenic belts based on the size of the components that collide, they are: the *collisional orogen* where two continents collide (large masses), and the *accretionary orogen* where smaller crustal fragments (*terranes*) collide with an active continental margin: one small mass versus a large mass (Ramos, 2008 *and references therein*). There is another type of classification based upon genetic constraints where *collisional orogens* consist of two continents brought together at the completion of a Wilson Cycle, and the two large masses are buoyant resulting in lithospheric thickening. In the case of *accretionary orogens*, metamorphism and crustal growth take place in an environment of long-term subduction and plate convergence without the collision of continental blocks or large scale buoyant lithosphere (Cawood, P. and Buchan, C. *and references therein*, 2007).

One important point to consider is that the two masses involved consist of continental crust, in the opposite case where one (or two) of the masses corresponds to oceanic crust then subduction will take place.

The collisional history, also called tectonometamorphic history, can be interpreted based on a distinct pressure-temperature-time (PTt) paths of the following features normally active in a convergent margin, therefore the study of them is the basis of recognizing large scale processes involving convergence of continents. Here, we present three features normally

involved in collisional and/or accretional processes:

- Accretionary prism: also called an accretionary wedge is a tectonically thickened wedge of sediment found on the edge of an upper plate being subducted. The accretionary prism consists of oceanic sediment scraped off the subducting plate, plus sediment derived from the upper plate and deposited in the trench. Slices of sediment are added to the wedge by underthrusting then the trench migrates seaward (Allaby and Allaby, 2003). The PTt path is normally a steep clockwise pattern, where the path is similar for prograde and retrograde metamorphism (Figure 1.1a) (Ernst, 2009).

- Terrane: a crustal block or fragment that preserves a distinctive geologic history that is different from the surrounding areas and that is usually bounded by faults (Coney, P. 1980). There are several types of terranes, such as *accreted terranes* which are terranes that become attached to a continental margin as a result of tectonic processes, *allochtonous terranes* which are accreted terranes that were emplaced in the present setting derived from other regions, *exotic terranes* which are terranes whose strinkingly different characteristics are different from the surrounding area, and finally *para-autochthonous terranes* which are fragments detached from the continental margin through a period of rifting and formation of oceanic crust, and later accreted to the same continental margin. In the cases where the collision of a terrane is involved, the PTt path can be either clockwise or anti-clockwise with a pressure peak different than the thermal peak for the same metamorphic complex (Figure 1.1b)(Garcia-Casco, A. 2012).

- Mobile belt: these consist of particular types of fold-thrust belts surrounded by cratons where metamorphosed and granitized basement is often associated with fragments of recycled basement. Through these processes, the crust was reworked and homogenized (Ramos, 2008; Lucassen, et al. 2000). The PTt path expected in mobile belts, would involve high temperatures up the point of anatexis, and strong overprinting in the mineral assemblages since it involves several metamorphic events (Figure 1.1c). The mobile belt concept applies to reworked crust in a timescale that spans eons, for example the Limpopo Mobile Belt in Southern Africa that consists of reworked Archaean granite-greenstone terrain with an early Paleozoic cover sequence (Mason, R. 1973).

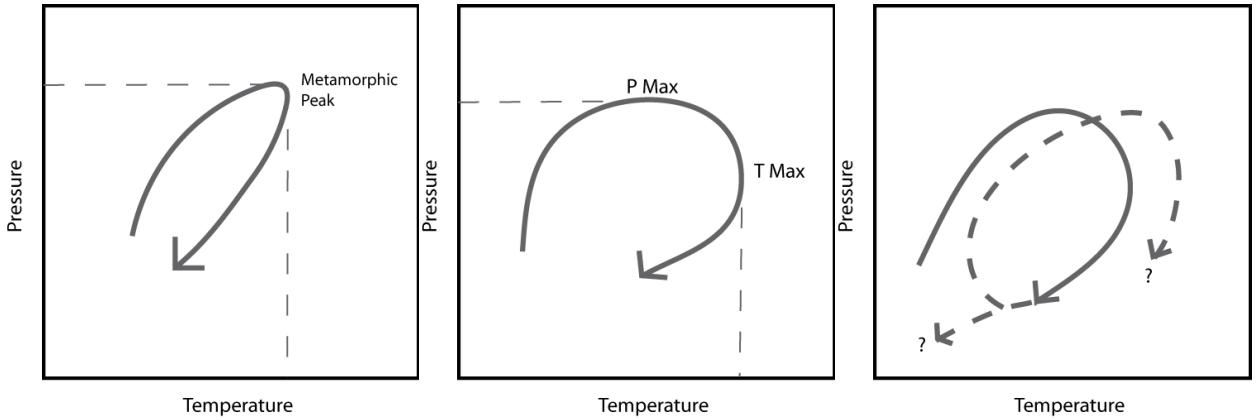

(a) Accretionary Prism (b) Terrane collision with thermal relaxation (c) Mobile Belt

Figure 1.1: Schematic pressure temperature time paths for features involved in a convergent margin.

1.1 Geological Setting

The Limón Verde Metamorphic Complex (LVMC) is part of a series of outcrops in a 12x2 km NNE strip (Godoy, 1983) located west of the Limón Verde Range, in the Antofagasta Region, Chile. The range encompasses a variety of Palaeozoic and Mesozoic rocks and a Cenozoic cover. This study is focused on the rocks only belonging to the LVMC and the Limón Verde Plutonic Complex (LVPC).

This metamorphic complex was first recognized and described by Harrington in 1961 (Godoy, 1983) who assigned a Precambrian age. Later on, the complex was studied by Baeza in 1976 as part of his doctorate thesis at the Freie Universität of Berlin who recognized a series of quartz-mica-schists intercalated with amphibolites and subordinate quartzites (Baeza, 1984). Hervé performed a regional survey of these complexes in 1988: LVPC and LVMC, and bounded the results to the Mejillones Metamorphic Complex.

Marinovic and Lahsen (1993) performed a geologic-structural survey of the area for SERNAGEOMIN and CODELCO, in the frame of the HOJA CALAMA map. Lucassen *et al.*(1999), carried out a petrologic study on a metamorphic petrology base whose results are being compared with results from this study. More recently, the area was surveyed by Tomlinson & Blanco as part of the SERNAGEOMIN Chuquicamata District report (2007). The area surrounding the Limón Verde Range comprises different structural domains: these domains are bound by large scale structures, seen in Figure 1.2 where the Range appears in

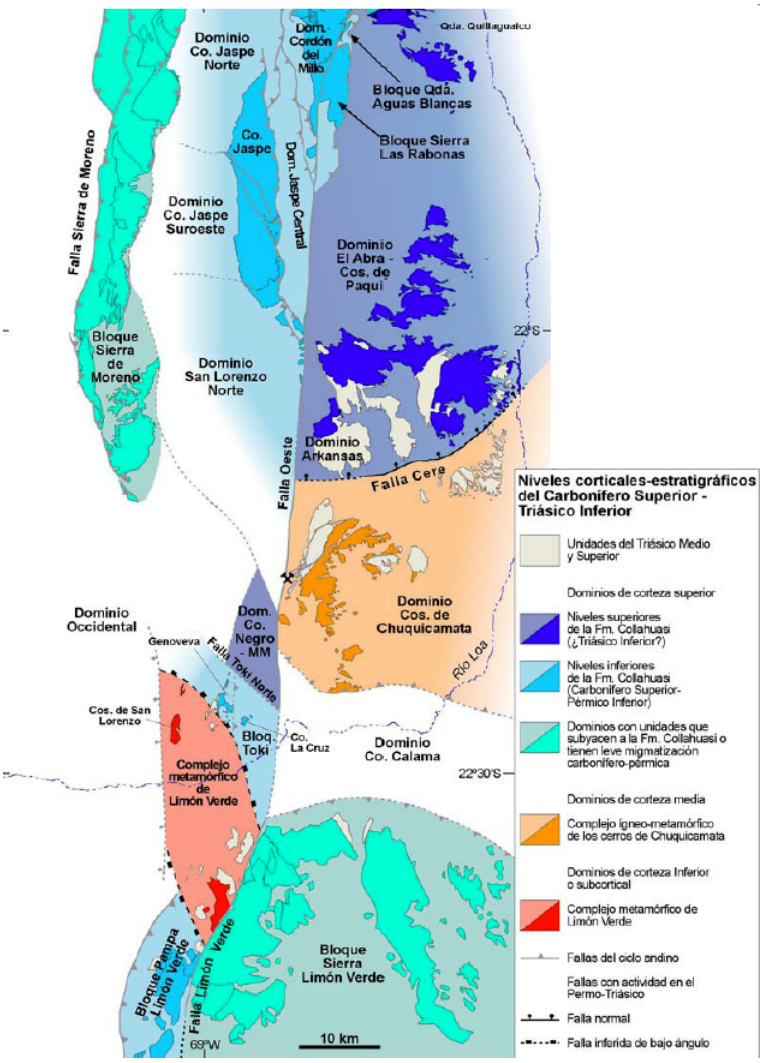

Figure 1.2: Crustal and stratigraphic levels from the Upper Carboniferous-Upper Triassic in the Antofagasta Region, Chile. Tomlinson and Blanco (2007) suggest that the Limón Verde metamorphic Complex (in red) not only includes the outcrops west of the Limón Verde Range, but also includes the Cerros de San Lorenzo, north of the Loa River. According to the same authors, the LVMC is bound by low angle thrust faults.

the bottom half of the image, and the metamorphic complex is in the bottom left part bound by two inferred low angle faults (Tomlinson and Blanco, 2007). Specifically, the LVMC is bound on the east by the Limón Verde Fault which is part of the Domeyko Fault System (Tomlinson and Blanco, 2007, Mpodozis, 2010).

Most of these metamorphic complexes have been associated to accretionary processes, and the afforsaid, have been linked to the hypothetical Arequipa-Antofalla terrane accreted to the Terra Australis Orogen during the late stages of the Gondwana assemblage (Ramos, 2009, Bahlburg et al, 2009, Charrier et al, 2007, Hervé et al, 2007, Lucassen et al. 1999).

Initial investigations in the area, were of a reconaissance nature in the search of an economic potential due to its privileged position with respect to the Eocene-Oligocene Metallogenic belt (Sillitoe, 2010), the major one being Chuquicamata, and its metallogenic district. According to Tomlinson and Blanco (2007), most Cu deposits from the Eocene-Oligocene

are located in the Precordillera in contact with Palaeozoic-Triassic basement or in contact with the Palaeogene-Mesozoic cover. Hence it has been postulated that the knowledge of the Palaeozoic basement and its surroundings is key to the understanding of the processes related to Cu mineralization. For instance, geochronological data indicate that the Carboniferous-Permian magmatism from the district stopped ca. 270 Ma, contemporaneous to the recognized metamorphism within the LVMC on the basis of Sm-Nd ages (Tomlinson & Blanco, 2007, Lucassen et al, 1999).

On a broader scale, there are four main structural domains in the Chuquicamata District: Sierra de Moreno, Western Domain, Sierra de Limón Verde and Chuquicamata Hills. The Sierra de Moreno Domain is specially important because it holds some of the oldest rocks in Chile (Charrier et al, 2007) belonging to the Meso-Neo Proterozoic; mica schists and gneisses, migmatites and amphibolites make part of the Sierra de Moreno Metamorphic Complex (Tomlinson & Blanco, 2007; Marinovic and Lahsen, 1984).

As dating and analytical techniques became more reliable, the interest in the LVMC shifted to a geodynamic perspective since the metamorphic complex seems diachronous with the rest of the rocks of the Sierra. Geothermobarometry studies of Lucassen *et al.*, (1999), determined peak metamorphic conditions (660^0C, 12-13 kbar.) at 270 Ma that have been interpreted as a metamorphic age very close to the age of igneous crystallization of these rocks (ca. 300 Ma) (Morandé, et al. 2012; *this work*) with a posterior rapid exhumation, inferring that there is very little time between emplacement and metamorphism.

The metamorphic block of Limón Verde, is limited at both sides by contemporaneous supracrustal rocks (Fig.1.4). It has been postuled by Tomlinson and Blanco (2007) that a large scale structure is required in order to place these units in contact, as seen in Figure 1.2. They postulate that such structure corresponds to a low angle fault, probably a normal fault, in which the LVMC makes up the footwall while the Collahuasi Fm and the asociated Permo-Carboniferous plutons (Limón Verde Igneous Complex) comprise the hanging wall. In such case, the distribution of these units suggests that the structure corresponds to an structural window, cut by the Limón Verde Fault on its southeast side (the Limón Verde Fault is one of the traces of the N-S trending Domeyko Fault system). Besides, a sudden increase in the thickness of the Jurassic-Cretaceous beds towards the west, suggest that the metamorphic complex is cut by a half graben fault on its western side (Tomlinson and Blanco, 2007).

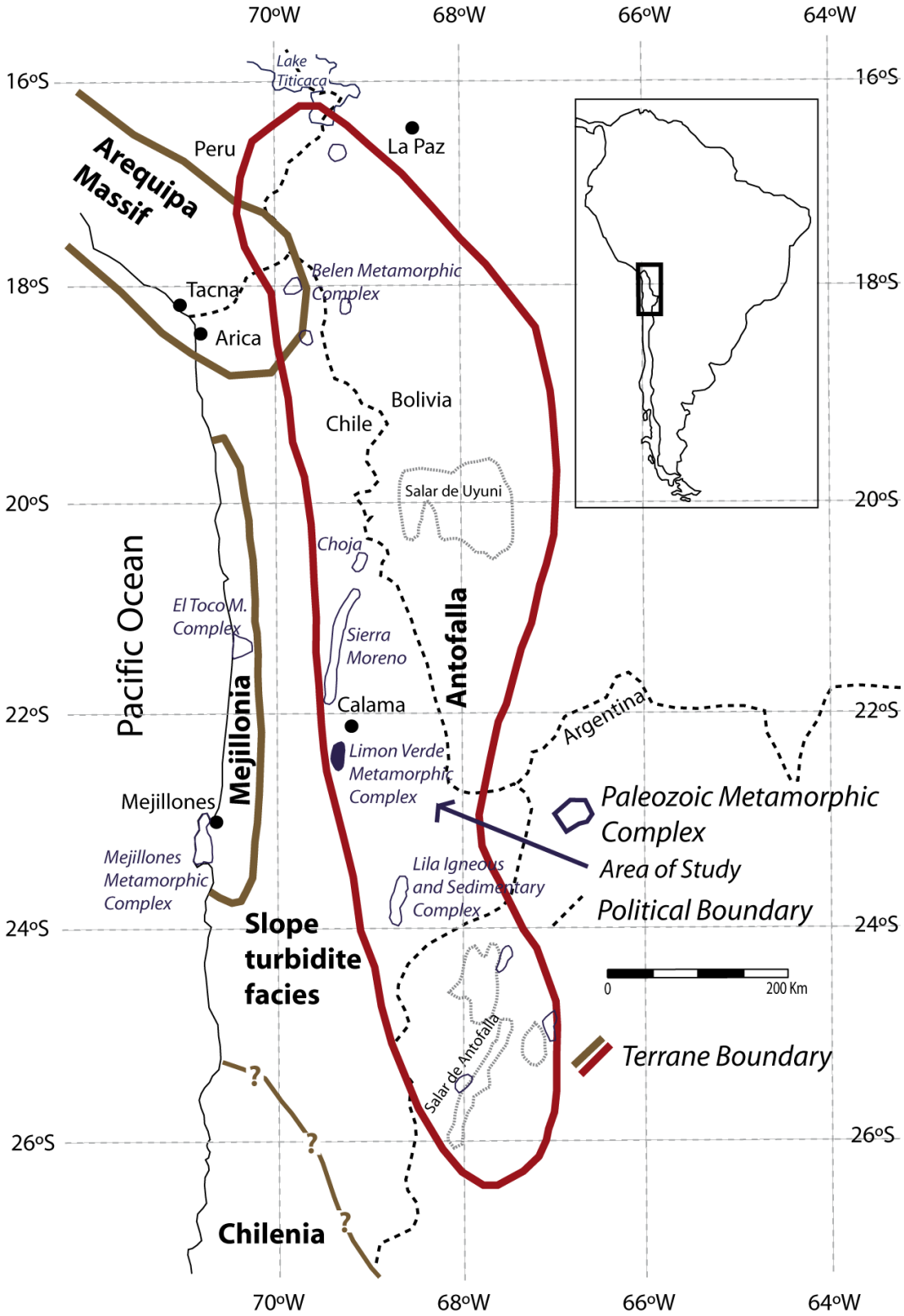

Figure 1.3: Approximate terrane boundary map in Northern Chile modified from Ramos (2008) and Hervé et al. (2007). The Limón Verde Complex is roughly aligned north-south with the Sierra de Moreno Metamorphic Complex and the Choja Metamorphic Complex. This has lead to previous authors to postulate a boundary for the Antofalla Terrane.

1.2 Scientific Problem

The Paleozoic basement in northern Chile has been subject of study in order to determine the tectono-dynamic history of the western margin of South America. Specifically, the metamorphic basement has been of interest, since the latter is associated to different episodes of crustal recycling, and to a lesser extent, to the accretion of juvenile material during the formation of the Terra Australis orogeny between 900-250 Ma (Bahlburg et al, 2009; Ramos, 2006). Exotic terranes can consist of microcontinents with evolved crustal material, or oceanic plateaus and guyots with juvenile material (Bahlburg, 2009).

As mentioned earlier, the metamorphic basement in this area crops out in discrete north-south stripes (Fig. 1.3), from which, it's been inferred they are allochtonous terrane boundaries, terranes which were accreted to the western margin of Gondwana during the Paleozoic (Cawood and Buchan, 2007; Ramos, 2008; Bahlburg, et al. 2009).

The Limón Verde Range is one of this north-south basement stripes and is part of the Cordillera de Domeyko structural domain. The Paleozoic basement of this range comprises intrusive carboniferous rocks from the Limón Verde Igneous Complex (LVIC), Paleozoic metasediments, Jurassic marine sediments and Paleozoic medium-to-high grade metamorphic rocks from the Limón Verde Metamorphic Complex (LVMC).

The hyphothesis of the current work consists on that the Limón Verde Metamorphic Complex was an accretionary prism active during the late Carboniferous, subducted and amalgamated to the western margin of Gondwana during the late Permian. Finally, the complex might have exhumed during the Triassic.

1.2.1 Objectives

The main objective of this thesis work is to precisely determine the pressure-temperature-time path of the Limón Verde Metamorphic Complex, to determine the tectonodynamic history of the area. The approach of this work, is through a comprehensive study of the geochemistry of the metamorphic rocks belonging to the complex. Thus secondary (or specific) objectives are:

- Perform mineral and whole classifications of the metamorphic units based on their geochemistry.

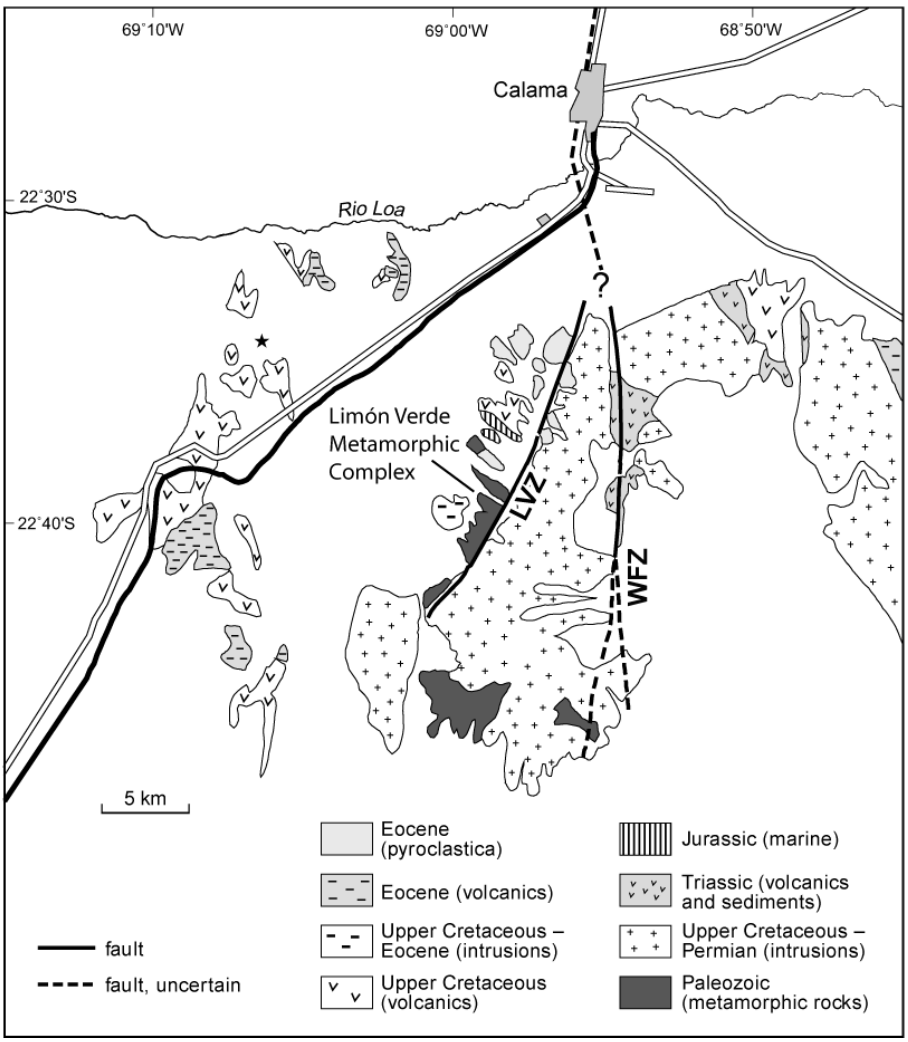

Figure 1.4: Location map of the Limón Verde Metamorphic Complex and its relation with the Limón Verde Fault Zone (LVZ). Map modified after Jansen, et al. 2002; WFZ stands for West Fault Zone.

- To determine protolith of the metamorphic rocks
- To determine the ages of metamorphism and associated igneous events
- Model pressure-temperature fields and paths using the software *Perple*χ.

Chapter 2

Methodology

2.1 Lithologic characterization

2.1.1 Mapping and Sampling

This work has sample contributions from two field campaigns: one with Francisco Hervé, Hans Massonne and Mauricio Calderón in July 2009, and a second one, the main one for this study, in July 2010. The samples for petrographic and geochemical analysis were obtained during a July, 2010 expedition along with Javiera Morandé and Constantino Mpodozis, sponsored by Antofagasta Minerals S.A. and FONDECYT project #1095099. In the field, due to logistics, only schist and amphibolite outcrops were visited. Samples of quartzite were taken as floats in this expedition. The location of where these samples were taken is shown in Table 2.1, and the corresponding location map is shown in Figure 2.1.

Both campaigns have had a sampling nature, and relied on existing maps (eg: Baeza and Venegas, 1984; Tomlinson and Blanco, 2007) hence most large scale structural and/or economical details were omitted from this study. The making of thin sections for transmitted and reflected light petrography was focused on foliated metamorphic rocks, specially the ones containing garnet.

In this work, six representative samples were studied thoroughly, four of these containing garnet: two garnet mica schist (samples FS-10-09 and FS-09-08), two garnet-amphibolites (FS-10-16C and FO-09-07). The remaining two samples, an amphibolite (FS-10-02) and a garnet-biotite schist (FS-10-16A), were analyzed in order to contribute to the reliability of

results.

2.2 Geochemistry

The large majority of geochemical whole rock and mineral analyses were funded by the BMBF-CONICYT collaboration project *Precise determination of P-T-t paths of metamorphic units in northern Chile as a way to identify their tectonic regimes* $\#175-2009$ between the Universidad de Chile and the Stuttgart University.

2.2.1 Whole rock

Major element whole rock analysis of two metamorphic samples containing garnet, garnet-amphibolite (sample FO-09-07) and a garnet-mica schist (sample FO-09-08) were done via Induced Coupled Plasma - AES (ICP-AES) at the Universidad de Chile.

The bulk chemistry of three other samples: two garnet mica schist and a garnet amphibolite, were measured at the University of St*ü*ttgart via X-ray fluorescence (XRF)in 2010. The XRF device was a PANalytical 2400, and measured major and trace elements. Samples FS-10-09, FS-10-16A and FS-10-16C were selected, because of their representativeness of the main metamorphic mineral assemblages present in the Limón Verde Metamorphic Complex and also because these contain garnet

With the results of the above mentioned techniques, several variables were calculated to determine protolith of the rocks.

2.2.2 Mineral chemistry

Major element geochemistry analyses of the main rock forming minerals were also performed at the Stuttgart University through Electron Microprobe Analysis (EMPA). Mineral analyses were obtained with an automated CAMECA SX-100 with 5 measuring crystals (FAP, LLIF, LiPET, TAP, PET). Qualitative analyses and the back scattered electron imaging was done through the Electron Dispersive Spectrometer (EDS) attached to the instrument. Operating conditions for the analysis of silicates in Wave Dispersive Spectrometry (WDS) mode were:

- Energy: 15kV

Table 2.1: Samples from the Limón Verde Range.# *Grab samples, no outcrop visible.*

Sample	Northing	Easting	Strike	Dip	Rock type
FS10-01	7516562	499276	342	90	Limestone interlayered with sandstone
FS10-02	7493049	501521	255	74	Czo- bearing amphibolite
FS10-03	7492983	501537	140	62	Garnet quartz mica schist
FS10-04	7492983	501537	140	62	Garnet quartz mica schist, earthy-hematite alteration
FS10-05	7492244	501137	335	64	Garnet quartz mica schist
FS10-06	7492454	504202	055	65	Foliated granodiorite
FS10-07	7492713	504123	315	42	Foliated gabbro
FS10-08	7493119	503675	335	60	Gneissic diorite
FS10-09	7493765	502196	180	42	Garnet qz-bt schist with amphiboles
FS10-10A	7492826	501050	155	8	Amphibolites with quartz-mica schist
FS10-10B	7492826	501050	180	0	Lineation from a fold axis
FS10-11	7493004	501459	330	69	Bt-amphibole schist
FS10-12	7492982	501541	310	65	Quartz-mica schist
FS10-13A	7479012	503650	rake	#	Diamictite
FS10-13B	4749012	503650	233	30	Diamictite
FS10-14	7482147	505863	165	60	Amphibolite
FS10-15A	7482040	506007	#	#	Quartzite
FS10-15B	7482040	506007	#	#	Calcareous quartzite
FS10-15C	7482040	506007	#	#	Mylonite
FS10-16A	4793761	502174	162	22	Plagioclase schist
FS10-16B	4793761	502174	105	60	Amphibolite intercalated with Quartz
FS10-16C	4793761	502174	050	47	Garnet-bt amphibolite
FO09-07	4795230	500934	045	32	Garnet-bt amphibolite
FO09-08	4795230	500434	*no data*	*no data*	Garnet mica schist
FO09-13	7495629	502773	260	85	Mica schist

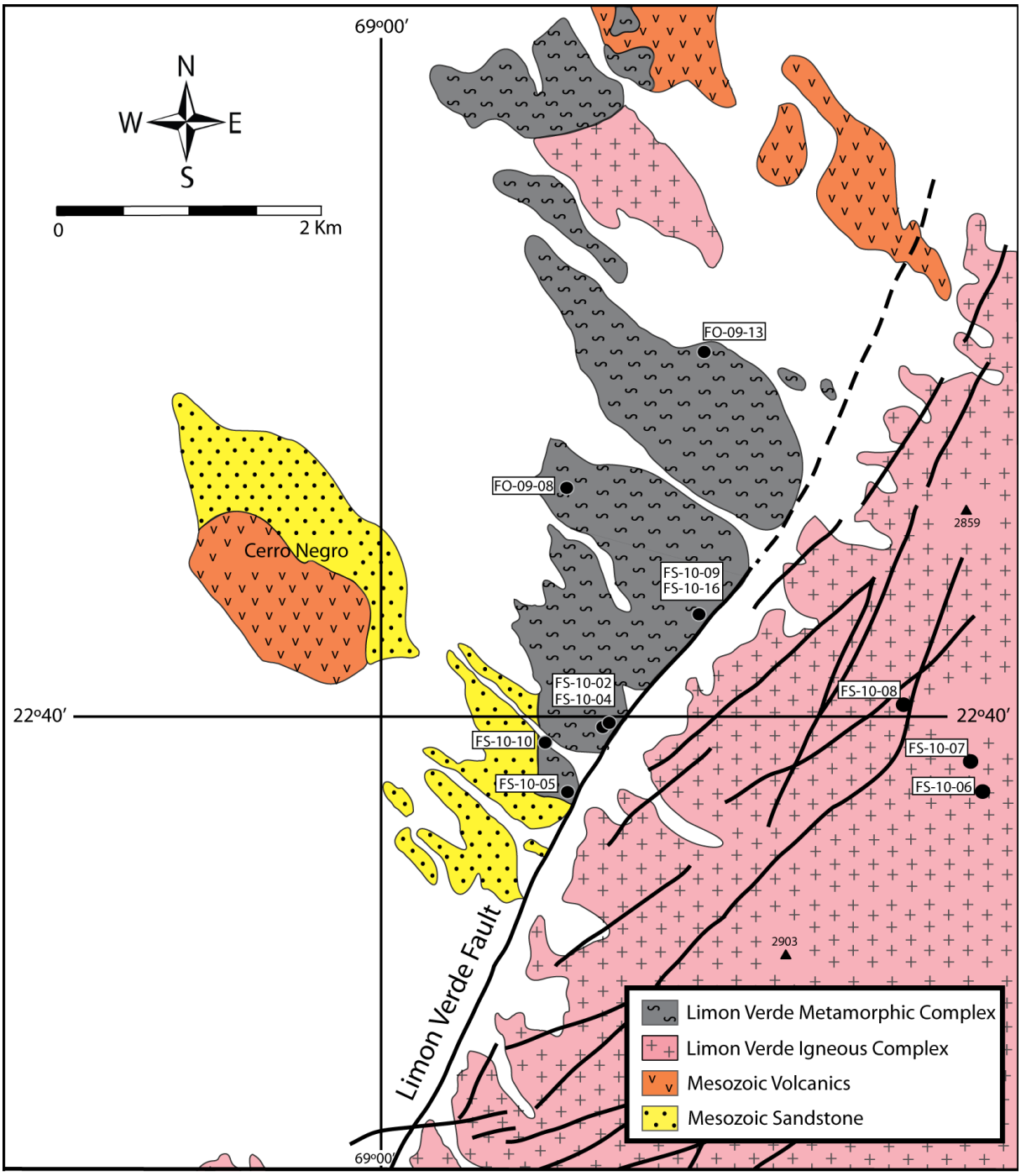

Figure 2.1: Simplified bedrock lithology map west of the Limón Verde Range, based on Baeza and Venegas (1984). The location of where the samples were taken is shown in circles.

- Current: 10 up to 40 nA depending on the mineral
- Detection time: 20 seconds per spot
- Beam diameter: 1 μ

X-Ray intensity maps were also acquired for garnets, micas, amphiboles and zoisites, by step-wise movement of the stage and a WDS constant beam. Average mineral compositions and classification of metamorphic minerals are in the following chapter, as well as the elemental maps showing compositional variation in silicates. In the compositional maps of the above mentioned minerals, color scale refers to counts per second of corresponding K_{alpha} radiation and elemental analyses were measured with the *sil* file.

Mineral formulae were calculated using CALCMIN, an open source Visual Basic Program implemented for EXCEL (Brandelik, A. 2008) or by hand based upon Deer, Howie and Zussman (1992) criteria. Most relations between cations for classification are shown in atoms *per formula unit* (p.f.u.).

For detailed analyses, refer to the Appendix.

2.3 Geochronology

2.3.1 SHRIMP U-Pb

Mica schists in the LVMC were subjected to medium to high temperature metamorphism, and these assemblages are suitable for the formation of metamorphic zircon and growth of metamorphic rims on pre-existing zircon grains. Thus U-Pb Sensitive High Resolution Ion Micro Probe (SHRIMP) dating is the most appropiate method for dating the events of formation of these rocks. Two samples were selected for this work: FO-09-08 and FO-09-13, both corresponding to garnet-mica schists: rocks were crushed and heavy minerals separated in the laboratories at the Departamento de Geología, Universidad de Chile. Then zircon concentrates were sent to the Australian National University (ANU) where Sensitive High Resolution Ion Micro Probe (SHRIMP) was carried out by Dr. C.M.Fanning.

U-Pb analysis for dating zircon was done in SHRIMP I; REE and Ti were measured in zircons from sample FO-09-08 to characterize the environment and temperature of formation respectively. REE and Ti were measured via SHRIMP RG.

Geostatistic analyses were done in the obtained results in order to determine ages of crystallization using the Isoplot 3.7/Excel macro provided by the Berkeley Geochronology Center.

2.3.2 TIMS Sm-Nd

Isotopic determinations of Sm and Nd were performed at the University of Arizona, with the help of Dr. Mihai Ducea and Derek Hoffman. Whole rock and garnet pairs were dated in a garnet mica schist (FS-10-09) and a garnet amphibolite (FS-10-16C).

The isotopic ratios of $^{143}Nd/^{144}Nd$, and the trace element concentrations of Sm and Nd were measured by thermal ionization mass spectrometry (TIMS) on a whole rock sample and a garnet separate. Whole rock samples of ca. 100 mg were collected to be garnet-free and powdered by hand in a small mortar. Garnet cores and rims were micromilled to a precision of a few microns. Milling was performed to avoid mineral inclusions in garnets.

Mass spectrometric analyses were carried out on an automated VG Sector multicollector instrument fitted with adjustable Faraday collectors and a Daly photomultiplier (Ducea, 2013 personal comunication). Whole rock samples were measured as elements, whereas the garnet samples were measured as oxides.

Results are treated and analyzed in Chapter 5.

2.3.3 Step heating Ar-Ar dating

Ar-Ar dating was done in three mineral phases: white mica and biotite from a garnet mica schist (sample FS-10-09) and in hornblende from an amphibolite (FS-10-02). These mineral phases were separated and handpicked at the Departamento de Geología of the Universidad de Chile by Roberto Valles and the author of this work. Then, the mineral separates were sent to the SERNAGEOMIN's Ar-Ar dating laboratory, in charge by Carlos Pérez de Arce, who did the step heating and processed the data obtained from this.

The Ar-Ar dating of the above mentioned samples was funded by SERNAGEOMIN, in the frame of the Moctezuma and Sierra Gorda maps (Plan Nacional).

2.4 Geothermobarometry

When we want to determine the metamorphic peak and metamorphic reactions in a rock, one important assumption to take into account is that the mineral phases present have to be in thermodynamical equilibrium with each other. These balanced reactions depend on pressure (P), temperature (T) and geochemical composition (X), thus the resulting mineral phases will have a specific composition for a given (P, T, X).

One approach is to start with a certain composition in at least a couple of mineral phases in equilibrium with each other and work backwards to find the conditions of formation (P and T). This is called *classical geothermobarometry*. A different approach is to start with a given bulk rock composition and a given P-T range, and model forward the possible rock assemblages until the current one seen in the sample is found. This method is called *forward modeling with PTX pseudosections*.

2.4.1 Classic

Based upon the mineral assemblages seen in the samples from this work, the suitable geothermobarometers were the **garnet-biotite thermometer** and the **garnet-muscovite-plagioclase-quartz (GMPQ) geobarometer**.

2.4.2 Forward Modeling

PTX pseudosections

A P-T-X pseudosection is a diagram that explicitly shows the minimum energy ($\Delta Gibbs$) assemblage in a whole rock composition given as two independent variables: pressure and temperature (P and T). A pseudosection is basically a diagram of phase equilibria and isopleths are isocompositional lines on a P-T field (Powell and Holland, 2010).

The most representative samples to produce P-T pseudosection with James Conolly's $Perple_X$ modelling program, v. 6.6.6 (downloaded on August, 2011) were a garnet-biotite schist (FS-10-09 and FO-09-08) and garnet zoisite amphibolite (FS-10-16C and FO-09-07). $Perple_X$ is a composite program where subprograms were called out: `build.exe vertex.exe` generates the pseudosection, and `pssect.exe` plots the file to a postscript to be later modified in a vectorial image processor such as Adobe Illustrator (Connolly, J. 1990).

For the creation of isopleths and to find out properties for a certain PT the program `werami.exe` was used. `werami.exe` contains several options: the third option plots a contour for a given property on a grid choosing a solution or phase (wt%) to finally use `pstable.exe` and input the ranges of isopleths, and outputs a postscript contour file. The numnber of nodes in the X and Y direction are 100 for each. The thermodynamic database and the solid solutions used to run these calculations were the Holland and Powell 2000 database.

The amount of H_2O was set manually until results were satifactory, and the CaO compositions were corrected for apatite. On the other hand, oxygen fugacity was set to medium values, because the amount of epidote and free oxides is significant enough in the the samples: at the end we considered that partial pressure of O_2 in whole rock is diferent than the amount of O_2 present in each mineral. It it worth mentioning that O_2 can not escape minerals from their structure like H_2O does (Massonne, 2012, personnal communication).

In the current study, temperature and pressure estimates were expected to be that of a medium to high grade system, then pseudosections were calculated between 5 and 15 kbar, simultaneously with temperatures ranging between 500 and 700^oC. All systems considered SiO_2 in excess and no melt in the calculation (because there is an absence of textures of anatexis in the sample). More details on the rest of the parameters used for modelling in the Appendix B. These 4 pseudosections were calculated on the MnNCKFMASHTO system. Field contours were smoothed and different grey intensities in the back of the P-T fields indicate different degrees of freedom: where lighter shades indicates more degrees of freedom than dark ones.

Compositional isopleths

In order to constrain the pressure-temperature fields of paragenesis of these rocks, and to determine P-T paths, isopleths were drawn. The values for isopleths were garnet components (Fe, Mg, Ca and Mn) and the content of Si a.p.f.u. in white micas. During this modeling, it was attempted to construct Fe-Mg isopleths in biotite, and Al-isopleths in phengites: these results were erratic and were dismissed from the final results.

The uncertainty of the obtained results is dependent on reactions, and yet it has not been quantified. There is general agreement among *Perple*χ users that the error associated with temperature is of $\pm 5\%$, and that of the pressure is of $\pm 10\%$.

Chapter 3

Petrography

Although samples were obtained from different parts of the Limón Verde Range, the main focus was on metamorphic and igneous samples which showed some degree of crystallization in a dynamic environment.

3.1 Mica Schists

The mica schist samples are strongly foliated, biotite and muscovite bearing rocks. These are samples: FS-10-03, FS-10-04, FS-10-05, FS-10-09, FS-10-12, FS-10-16A. Of these, only some contain garnet, where the paragenesis of the garnet-biotite schist samples consists of $Grt + wmca + Bt + Qtz \pm Czo \pm Pl \pm Ru$.

These samples bear a marked lepidoblastic texture in medium grained biotite and white mica. Biotite sheets are strongly pleochroic orangy-red flakes with a second order birefringence and strong birdseye extinction. They show up interlayered with white micas, and follow the same foliation orientation (Figure 3.1b). Only few mica flakes cut the main foliation and there is a possibility that these may be pseudomorphs of aluminosilicates.

Plagioclase and quartz with sutured edges and undulose extinction make up to 50% of the sample. Feldspars show exsolution lamellae, and are only present in few samples up to 10% at its most abundant. The samples also show a bimodal size distribution of garnet porphyroblasts. Large garnet porphyroblasts contain many inclusions: quartz, opaques, and rutile, also these garnets are highly fractured and chloritized in edges and fractures. The texture of the larger porprhyroblasts looks mostly skeletal. At the same time, these

porphyroblasts seem to be syn-kinematic, as their quartz and rutile inclusions are oriented (snowball garnet). One sample (FS-10-04) contains up to 5% (large) amphiboles aligned with the main foliation and are very broken, not even conserving a pseudomorph appearance. Smaller second generation garnet is of hypidiomorphic equant crystals, and shows a regular unaltered appearance. Accesory minerals in the sample are zoisite, zircon, rutile, opaques. Retrograde chlorite is colorless and has a low first order birefringence color, its habit is sheeted like and cross-cuts the main foliation of the sample. Sample FS-10-05 is strongly hematitized, and thus not suitable for mineral analysis. Instead, sample FS-10-09 was chosen for mineral analysis.

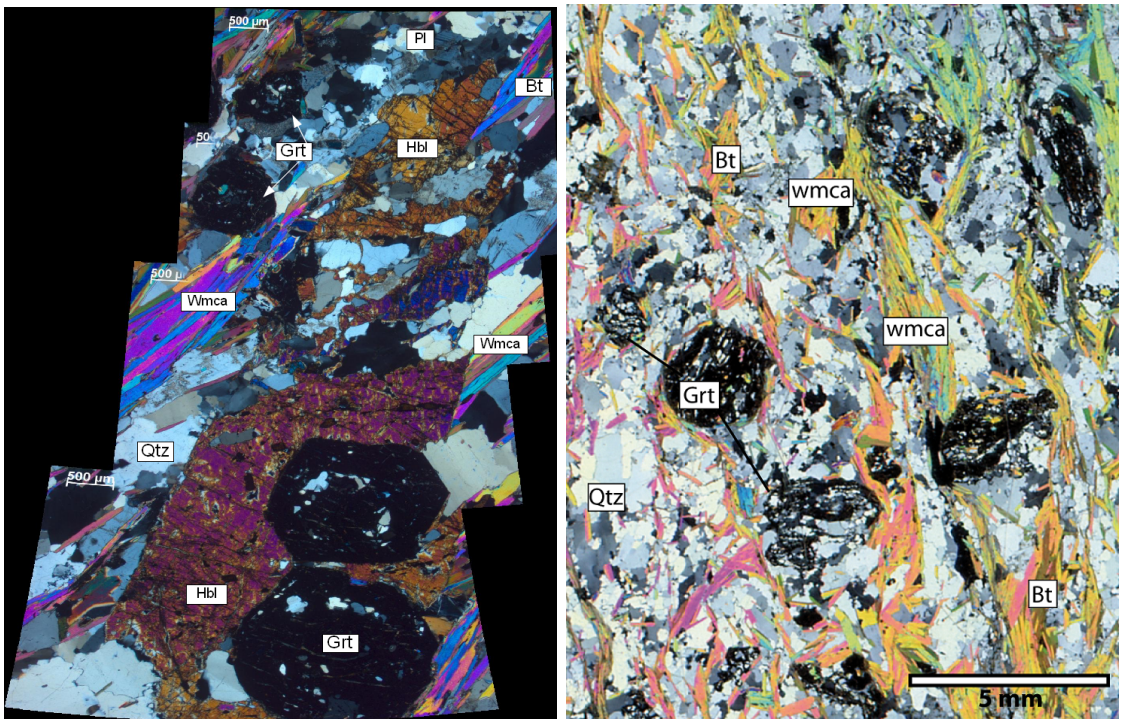

(a) Sample FS-10-04 (b) Sample FS-10-09

Figure 3.1: Qz-Gt-Mica Schist XPL images (sample FS-10-04 and FS-10-09). In the center of the left image a large hornblende oriented parallel to the main foliation is seen. Both images show first and second generation poikilitic garnets in paragenesis with elongated mica fish (white micas and biotite), distinguishable by their very high birefringence colors. Figure 3.1a with an amplification of 2.5X

.

Sample FS-10-16A (Fig. 3.2 is seen as incomplete bands of quartz and feldspathic silicates. Similarly, the thin section shows a pervasive undulose extinction and pressure solution structures in the minerals mentioned above. Some of the zoisite, quartz and feldspar grains possess inclusions and recrystallization textures overprinting the previous twinning. There is

also sericite alteration along twinning. Zoisites are pseudo-parallel to the main foliation with very little alteration, on the other hand biotite and white mica are present in thin bands (less than 1 mm) or as sheets cutting the main foliation. Some of the garnets present in the sample were also strongly altered and sometimes completely replaced by chlorite (smectite?). Unaltered garnets and garnet pseudomorphs have been broken down by shear parallel to the main foliation, and it is visible only part of them.

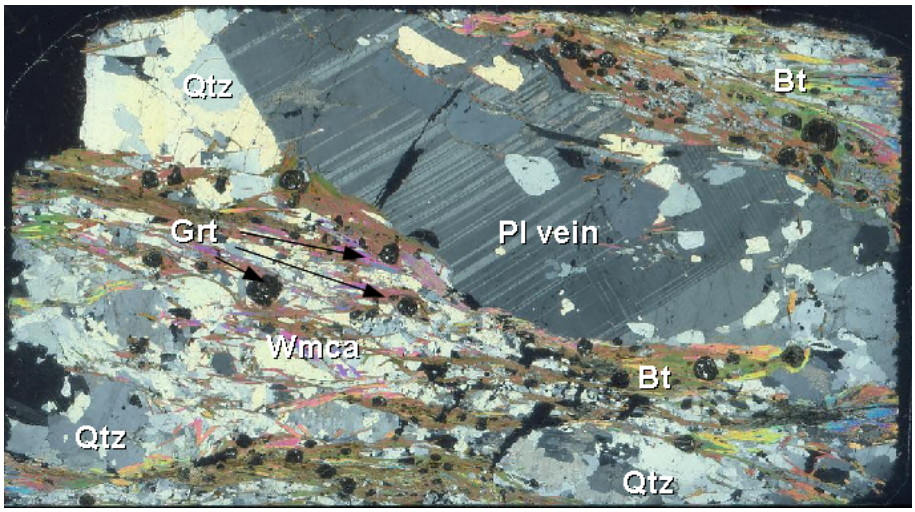

Figure 3.2: Garnet mica schist sample with a large vein of plagioclase cross-cutting the foliation. The size of the image corresponds to the size of a whole thin section. Mineral abbreviations in the appendix

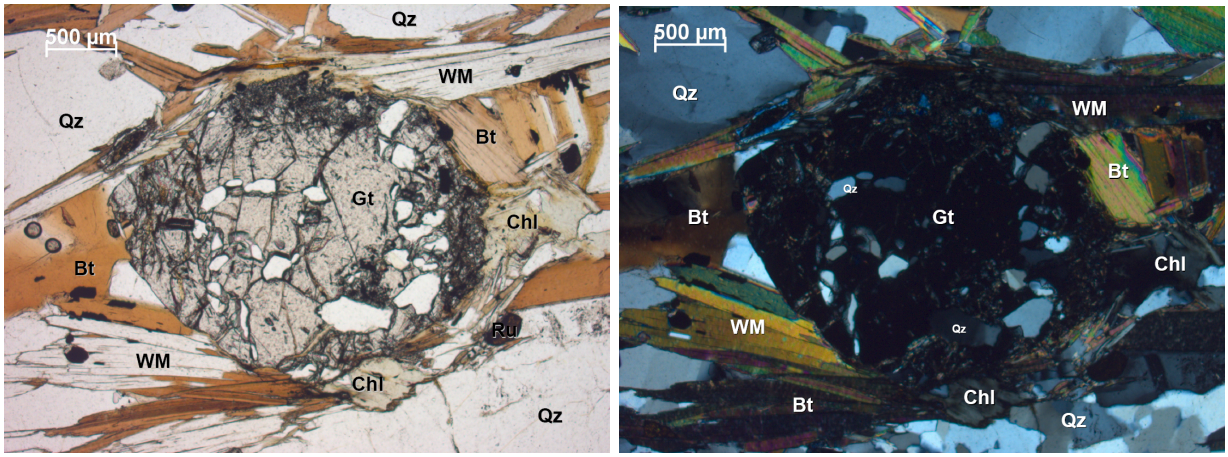

Figure 3.3: Snowball garnet in a garnet mica schist (sample FS-04), looks like a sigma porphyroblast, containing quartz and rutile inclusions following a rotation pattern. PPL on the left side, XPL on the right hand side. *WM: white mica, Bt: biotite, Gt: garnet, Qz: quartz, Chl: chlorite, Ru: rutile.*

3.2 Amphibolites

This rock unit consist of strongly foliated clinozoisite-amphibolites, or biotite-amphibolites. These are samples: FO-09-07, FS-10-02, FS-10-10A, FS-10-14 and FS-10-16C.

Sample FS-10-02 and FS-10-14 present a paragenesis that consists of $Hbl + Qtz + Czo + Pl \pm Ttn \pm Rt$. From this sample, it is important to mention that hornblende and titanite were separated for dating.

The rest of the above mentioned samples contain garnet in different modal proportions: from them, samples FO-09-07 and FS-10-16C were used since their parageneses consist of $Hbl + Qtz + Czo \pm Grt \pm Fsp \pm Ttn$. Thus, the principal rock type used in this study was in this rock type (garnet-amphibolite).

Microfaulting and kink band in biotites, snowball garnets and rutile inclusions indicate a dynamic environment of formation. It was determined (petrographically) that at least two types of amphibole coexist with slight difference in habit and birefringence, these contain titanite, plagioclase and zoisite inclusions. A small amount of in echelon fractures present in amphiboles, have been interpreted as weakness planes with semi-brittle behavior

The amphibolite samples that contain large equant (millimetric) garnet porphyroblasts, containing numerous inclusions and showing chloritization along rims and cracks. Some large garnets that have been broken down, have been stretched in the same direction of the main foliation. These porphyroblasts are in contact with biotite, amphibole, zoisite and strongly altered plagioclase. Also in some garnet, inclusions form trails parallel to the main foliation.

Similarly, most amphibolite samples contain large zoisite (up to 20% of each sample), with tabular habit that makes up a nematoblastic lineation in the rock. Biotite in the sample are elongated orange-red sheets with some degree of chloritization present along edges and cracks (up to 10%), these elongated sheets are in paragenesis with amphibole and garnet. Small white mica crystals normally appear in contact with biotite and garnet, and make up between 3 and 5%.

Accessory minerals in these samples are titanite, rutile, zircon, apatite, and opaque minerals with titanite being the main titanium phase, in some cases pseudomorphed to rutile and ilmenite. Recognizable retrograde minerals are colorless chlorite (with grey first order birefringence) and rutile.

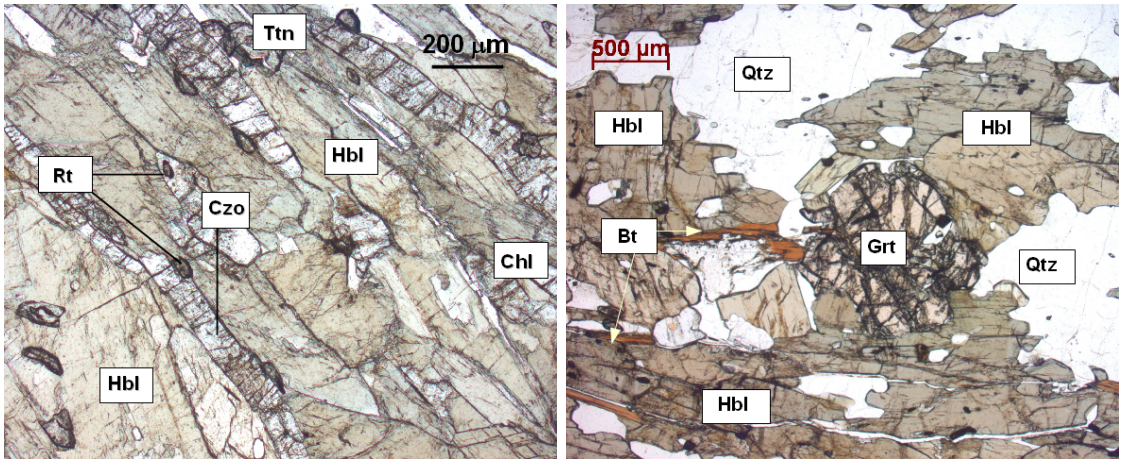

(a) Nematoblastic texture in amphibole and clinozoisite

(b) Garnet in paragenesis with amphibole and biotite

Figure 3.4: Amphibolites. Foliation of these rocks encompasses most tabular minerals present in the sample. A poikilitic texture is visible in both samples, where the most common inclusions are quartz, titanite and rutile. Both images in PPL. *Czo: clinozoisite, Hbl: hornblende, Rt: rutile, Ttn: titanite, Grt: garnet, Bt: biotite, Qtz: quartz.*

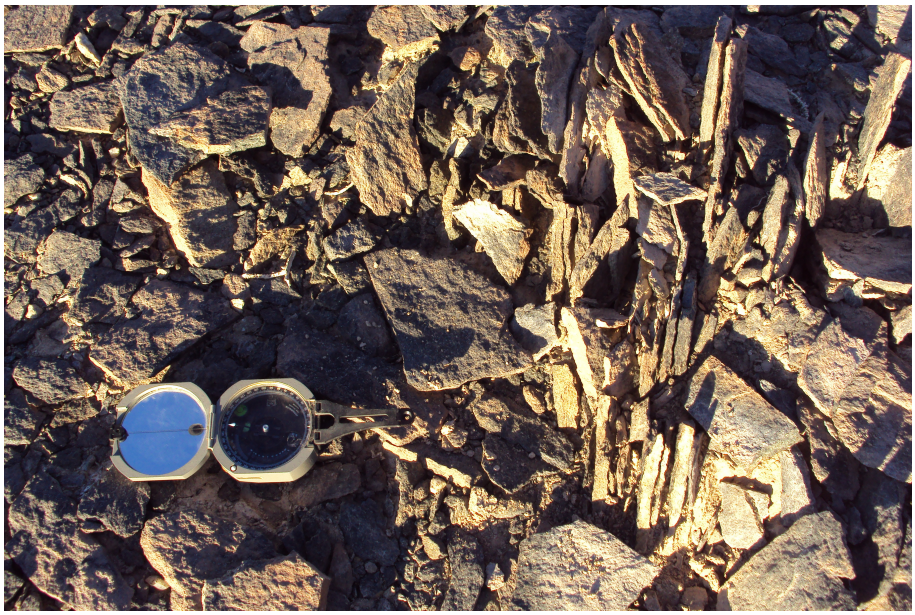

Figure 3.5: Outcrop disposition of the amphibolite from sample FS-10-02. Compass for scale.

3.3 Foliated intermediate igneous rocks

These rocks belong to the eastern part of the Limón Verde Range and their composition varies between tonalite and granodiorite. Described samples are from the locations shown in the simplified geology map from Figure 2.1. According to the literature these rocks belong to the Limón Verde Igneous Complex, active from the Carboniferous to the Permian (Marinovic and Lahsen, 1984). In outcrop, these rocks possess a moderate pervasive foliation and may have been described as gneisses by other authors. Previous interpretations by Baeza and Venegas (1984) have differenciated 4 lithologic types to be part of the Limón Verde Igneous Complex (LVIC): Diorites and gabbroic enclaves, granodiorites and tonalites, coarse grain granites and fine grain granites.

Sample FS-10-14 is a diorite containing strongly altered amphiboles, which looks more like a metadiorite with moderate pervasive foliation. Most feldspars in the matrix have been completely replaced to sericite-epidote. Similarly, most amphiboles (magmatic hornblende? metamorphosing to actinolites) have been chloritized (smectite variety) and relict polysynthetic twinning is visible in plagioclase. No large micas are present in the section. Titanite trails bound groups of amphiboles in the same foliation plane, same as clear rutile laths in feldspars from the matrix.

Sample FS-10-07 is a strongly foliated dark green diorite (Figure 3.6), which contains oriented plagioclase laths (with augen habit), with chloritized green amphibole (actinolite and hornblende) making up to 30%, and subordinated (also chloritized) biotite.

Sample FS-10-08 is interpreted as an extremely altered metagranodiorite, even showing some migmatitic textures. Most plagioclase and potassic feldspars present in the sample have a cloudy looking appearance, with pervasive mottled texture. These contain trails of inclusions (too small to be recognized with the petrographic microscope), with a slight orientation. Ferromagnesian minerals with an amphibole habit have been mostly chloritized (smectite variety). No preferred orientation of minerals present in the sample.

Sample FS-10-06 is a biotite bearing granodiorite which shows sutured quartz with undulose extinction, where the main ferromagnesian mineral is biotite. Slight epidote accumulation between extremely altered plagioclase and biotite. The sample possess a moderate foliation visible only in hand sample.

These samples could be classified as part of the two lithologic types described earlier.

(a) Outcrop disposition of sample FS-10-07

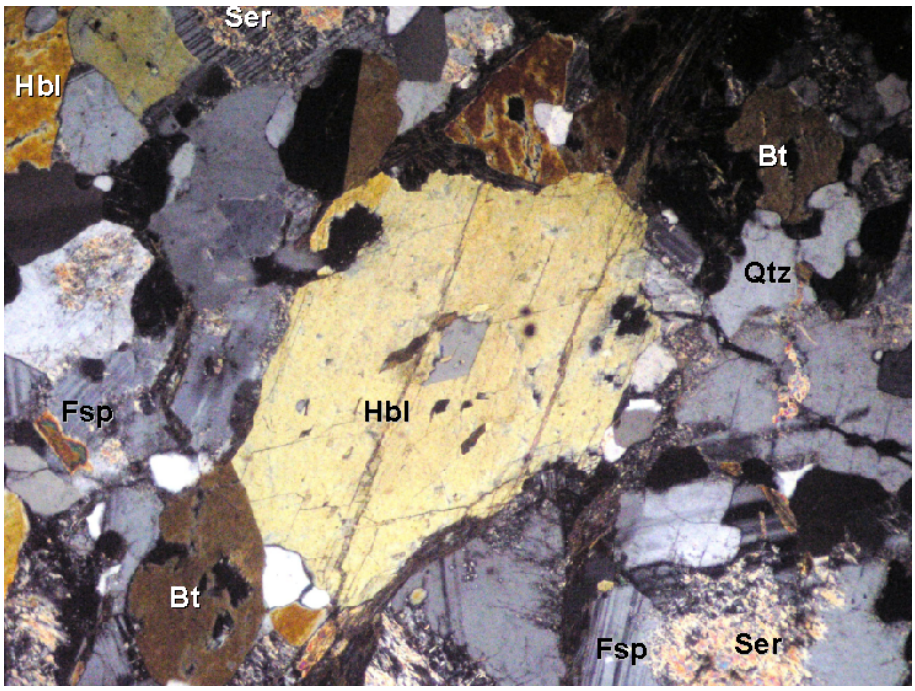

(b) Crossed polars thin section image of sample FS-10-07. Magnification 4X

Figure 3.6: Strongly foliated diorite (sample FS-10-07). *Hbl: hornblende, Bt: biotite, Qtz: quartz, Ser: sericite.*

Chapter 4

Geochemistry

4.1 Whole rock major and trace element chemistry

Whole rock major and trace element analyses done via XRF and ICP-AES are shown in Table 4.1 for the two garnet mica schist (samples FS-10-09 and FO-09-08) and the two garnet amphibolites (FS-10-16C and FO-09-07).

These results, were normalized and recalculated to be input in the pseudosection calculation with the corresponding apatite and Fe^{3+} corrections. At the same time, the bulk chemistry of samples FS-10-09 and FS-10-16C was also plot in an ACF (amphibolite) and AFM (schist) diagrams in order to correlate it with mineral associations present in the samples.

Table 4.1: Major element oxide and volatiles concentration determined by X-Ray Fluorescence and ICP-AES

Oxide (%)	FS-10-09 Grt-Schist	FS-10-16C Grt-Amphibolite	FO-09-07 Grt-Amphibolite	FO-09-08 Grt-Schist
SiO_2	72.173	53.350	52.272	64.888
Al_2O_3	12.519	12.219	11.671	13.688
MnO	0.139	0.156	0.292	0.240
MgO	2.041	8.950	6.415	2.494
CaO	1.190	7.577	4.874	1.296
Na_2O	0.562	1.240	0.576	1.018
K_2O	2.892	1.210	1.799	3.373
TiO_2	0.666	1.694	1.736	1.100
P_2O_5	0.110	0.225		
Fe_2O_3	5.54	11.78	10.377	6.883
Total	**97.839**	**98.387**	**97.839**	**96.483**
FeO	4.992	10.59		
CO_2	1.273	0.762		
H_2O	1.71	2.110	4.874	4.943

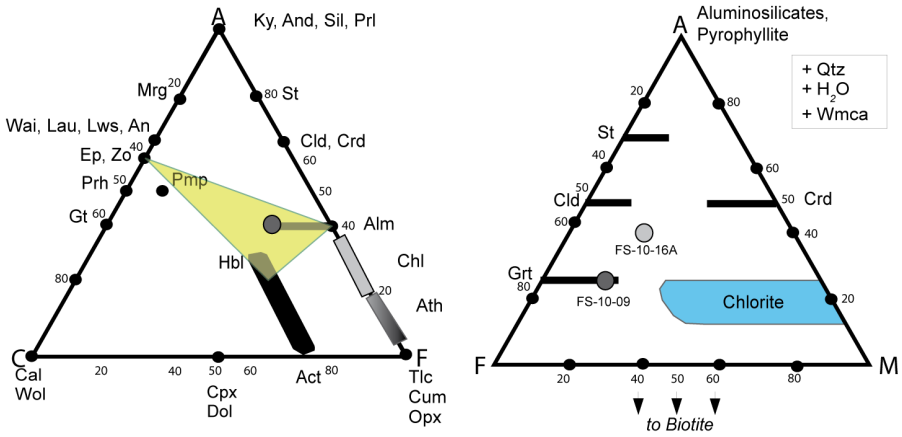

(a) ACF diagram for metabasites (b) AFM diagram for metapelites

Figure 4.1: Figure 4.1a ACF diagram for metabasites in sample FS-10-16C, sample is represented as a grey circle. Paragenesis of this sample consists of $Zo + Bt + Amp + Gt$. Figure 4.1b AFM Diagram for the Bt-Grt Schist in sample FS-10-16A and the Grt-wmca Schist from sample FS-10-09. Paragenesis of these samples consists of $Qtz + wmca + Bt + Grt + Pl$ and $Qtz + wmca + Bt + Grt$, respectively.

A protolith calculation for the amphibolite samples were done in order to determine whether the sample comes from the metamorphism of a sedimentary rock (dolomite marl) or from an igneous origin. The discriminant functions applied (3 functions) are based upon the analysis whole rock non-mobile elements (Shaw and Kudo, 1965): the main two discriminant functions consider minor elements, which were only available for sample FS-10-16C (garnet amphibolite). The minor elements considered are Cr, V, Ni, Co, Sc, Sr, Ba and Zr (values in ppm) for the following two funcions:

$$X_1 = -2.69 \log Cr - 3.18 \log V - 1.25 \log Ni + 10.57 \log Co + \\ + 7.73 \log Sc + 7.54 \log Sr - 1.95 \log Ba - 1.99 \log Zr - 19.58 \quad (4.1)$$

$$X_2 = 3.89 \log Co + 3.99 log Sc - 8.63 \quad (4.2)$$

The calculation of these two parameters indicates that if X_1 or X_2 are positive, the protolith is igneous. In the case that these values are negative, the protolith is sedimentary. For sample FS-10-16C, $X_1 = 2.67$ and $X_2 = 2.91$, indicating that we are dealing with an ortho-amphibolite.

There is a third parameter X_3 that involves the major components of the rock, with the

Table 4.2: Whole rock minor and trace element concentrations determined by X-Ray Fluorescence for a garnet mica schist (FS-10-09) and a garnet amphibolite (FS-10-16C). *BDL* stands for Below Detection Limits.

Element(ppm)	FS-10-09 Grt-mca schist	FS-10-16C Grt amphibolite
Sc	8.767	7.608
V	104.332	261.471
Cr	86.783	406.264
Co	121.591	115.608
Ni	22.543	260.330
Zn	52.360	127.304
Ga	14.993	16.832
Ge	0.528	0.105
As	8.963	5.111
Se	BDL	BDL
Rb	89.133	35.952
Sr	71.607	31.231
Y	26.767	21.064
Zr	160.242	149.568
Nb	12.907	20.826
Mo	0.939	0.149
Cd	1.433	0.539
Cs	2.273	BDL
Ba	918.676	184.717
La	33.242	21.638
Ce	73.181	39.976
Pr	9.289	0.176
Nd	37.768	24.341
Sm	5.329	BDL
Yb	7.429	0.089
Hf	BDL	2.745
Ta	3.710	BDL
W	943.710	590.720
Tl	0.797	BDL
Pb	9.539	4.762
Bi	2.001	3.288
Th	9.416	3.161
U	BDL	BDL

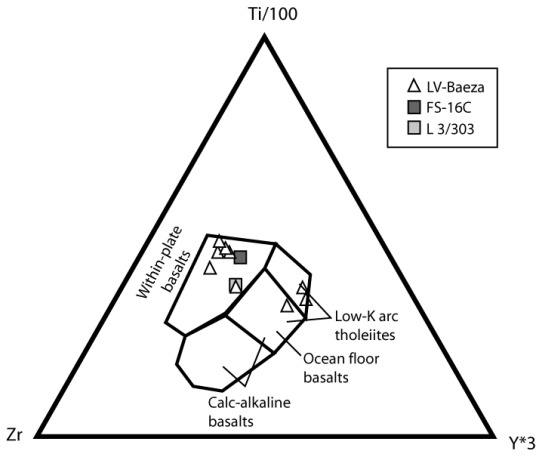

Figure 4.2: Y-Zr-Ti Pearce and Cann (1973) basalt discrimination diagram for samples FS-10-16C (this work), 3/303 (Lucassen, 1999) and LV series from Baeza, 1984. Grt-Zo amphibolites (squares) fall on the *Within plate basalt* field, in addition, more than half samples from the LV metabasite series from Baeza (1984) fall on the same field.

function:

$$\begin{aligned} X_3 = {} & 7.07 \log TiO_2 + 1.91 \log Al_2O_3 - 3.29 \log Fe_2O_3 + \\ & + 8.48 \log FeO + 2.97 \log MnO + 4.81 \log MgO + 7.80 \log CaO + \\ & + 3.92 \log P_2O_5 + 0.15 \log CO_2 - 15.08 \end{aligned} \tag{4.3}$$

$X_3 = 3.54$ in the same garnet amphibolite sample (FS-16C), which is consistent with the previous results. Regretably, we are unable to compare this result with the other garnet-amphibolite sample studied in this work (FO-09-07) because of the lack of CO_2 analysis. CO_2, TiO_2 and P_2O_5 are the most effective oxides for discrimination of protolith in metabasites (Shaw and Kudo, 1965).

Assuming that the discrimination is correct, and that the metabasites have in effect, an igneous origin, the question arises of what kind of basalt this rock come from. Later the garnet-amphibolite sample was plot in a Pearce & Cann basalt classification diagram (Pearce and Cann, 1973) from Figure 4.2 which indicates an intra-plate basalt affinity for this rock.

Previous results by Baeza in his doctorate thesis (Baeza, 1984) are not conclusive for metabasites: he found that the amphibolites came from an igneous origin based upon chemistry and current disposition with other rocks from the complex. Baeza (1984) also calculated several parameters for protolith determination but obtained affinities for intraplate and ocean-floor basalts in the same proportion.

4.2 Major element mineral chemistry of metamorphic samples

4.2.1 Garnet

Garnet as a metamorphic mineral, is specially important for geothermobarometry studies since its main components (Fe=almandine, Mg=pyrope, Ca= grossular and Mn= spessartine) record pressure-temperature changes during the mineral growth (Spear, 1993). Garnets from amphibolite samples are not too different visually from the ones in the mica-schists. In both cases, these are present in at least two visible generation of garnets (mentioned in the petrography chapter): a larger older generation with a characteristic concentric zoning as seen in Figures 4.4 to 4.5, and a smaller secondary generation with no compositional zoning i.e. a relatively homogeneous composition.

In the compositional maps of garnet obtained with a CAMECA SX100 Electron Microprobe, color scale refers to counts per second (c/s) of corresponding K_{alpha} radiation and elemental analyses were measured with the *sil* file.

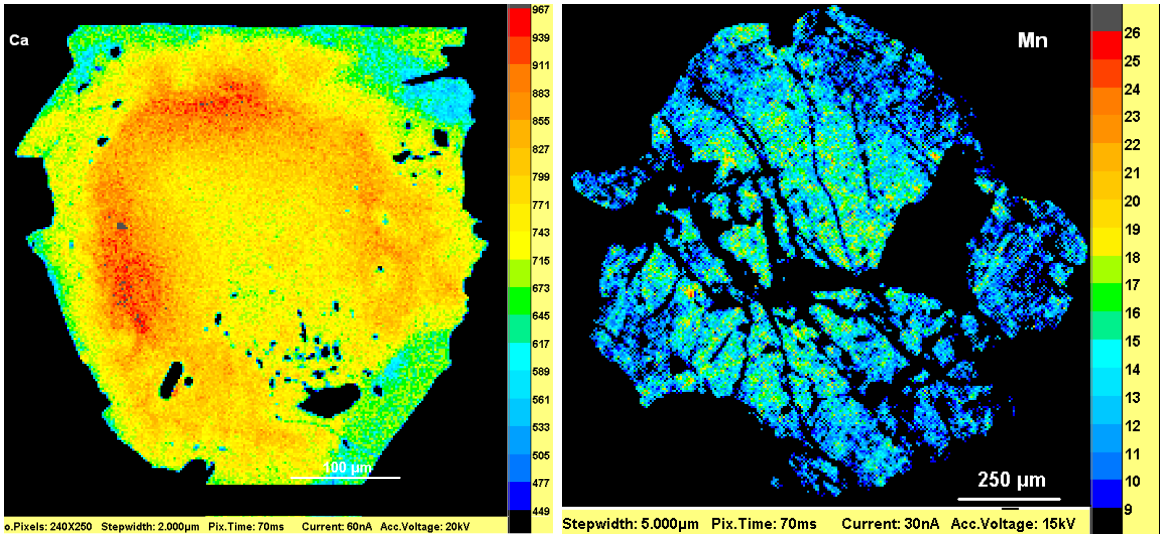

(a) Garnet from schist (b) Garnet from amphibolite

Figure 4.3: X-ray intensity maps for Ca and Mn in small garnets with lack of zoning. Color scale refers to counts per seconds of K_{alpha} radiation

Garnet formulae and fraction component were obtained with the CALCMIN application for excel, which recalculates to 12 oxygens, and gave the following results:

Table 4.3: Garnet component ranges in mica schist and amphibolite

		Garnet mica schist (FS-09)		Garnet amphibolite (FS-16C)	
Element	Component	Min	Max	Min	Max
Ca	Grossular	0.080	0.270	0.200	0.286
Mg	Pyrope	0.116	0.189	0.080	0.175
Fe	Almandine	0.490	0.812	0.530	0.617
Mn	Spessartine	0.010	0.016	0.017	0.110

Garnet from mica schist

Mica schist samples hold garnets with a slight metallic luster (this may be due to the micas in the rim) and possess mica sheets embedded in the crystal structure. Larger broken down garnets have an orange tint with respect to the smaller ones. At the same time, the latter are a lot more euhedral even the ones which have been sheared and show signs of dynamic metamorphism. The composition of garnets from the mica schist samples is very strong in their almandine component, then the pyrope and grossular components have similar values in most samples.

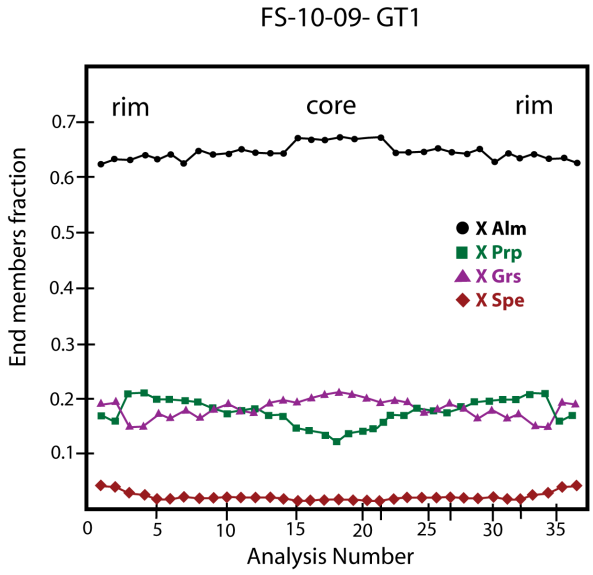

(a) Rim to rim analyses

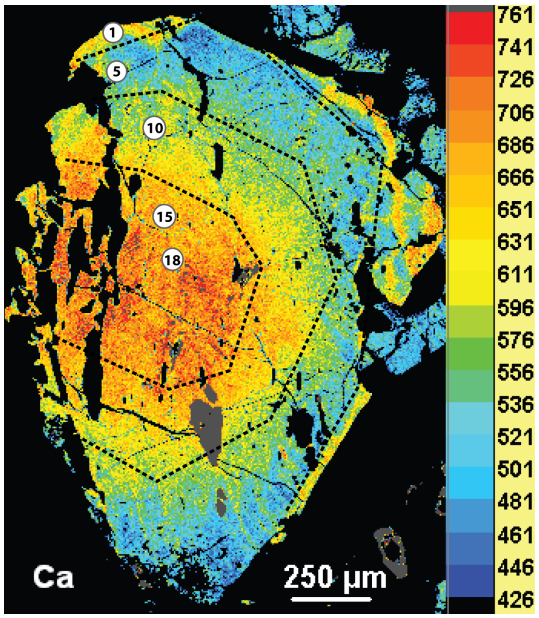

(b) Zoned garnet, notice the yellow rim which indicates retrograde metamorphism

Figure 4.4: A large zoned garnet from a grt-mca-schist (sample FS-09) shows a compositional map for Ca (figure 4.4b)with corresponding graph with zonation pattern for the four components: almandine, pyrope, grossular and spessartine. Sites of analytic numbers are shown in image 4.4b. Color scale refers to counts per second of corresponding K_α ratiation.

Garnet from amphibolite

Amphibolite samples contain strongly chloritized large broken down garnets. These garnets vary from a light to a bright pink. Small unaltered garnets show no zoning and no deformation as opposed to the larger ones which present different degrees of zoning and a visible deformation history. Large garnets have a strong almandine component, seconded by their grossular component where both Fe and Ca were fairly constant from core to rim (Figure 4.5). The pyrope and spessartine components were minor in these garnets, nevertheless these components represent the most prominent zonation (Figure 4.5).

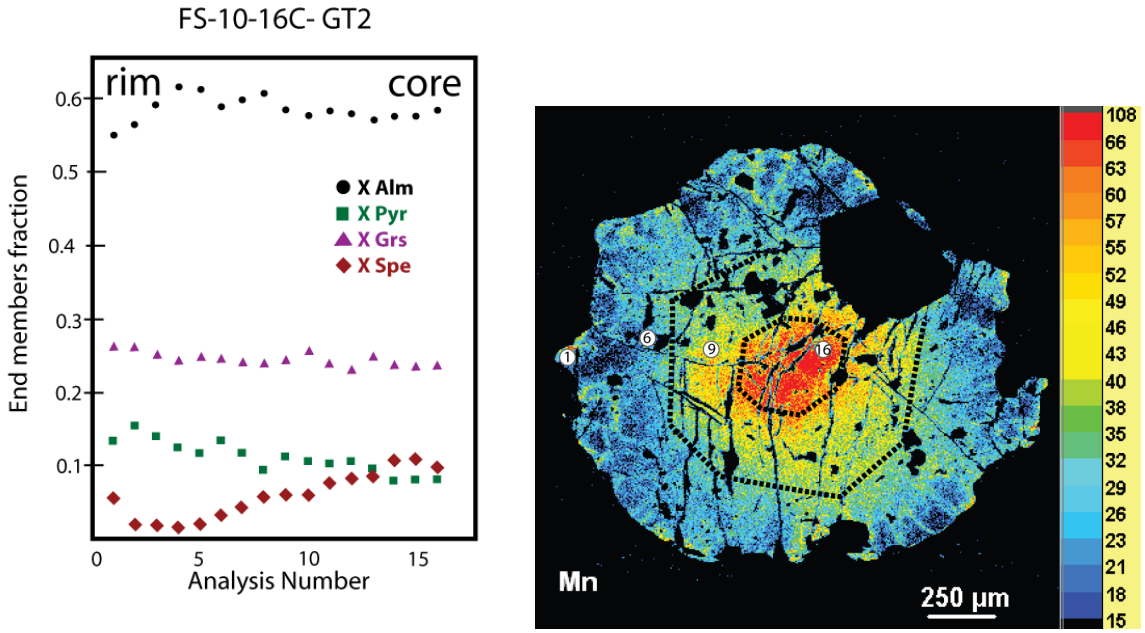

(a) Rim to core analyses

(b) Zoned garnet with inclusions

Figure 4.5: Sample FS-10-16C. Compositional map of a large zoned garnet for Mn with corresponding graph with zonation pattern for the four components: almandine, pyrope, grossular and spessartine. Analytic number are shown in image 4.5b.

4.2.2 Micas

Di-octahedral micas

Di-octahedral (or white micas) are present in the large majority of the samples analyzed in this study, and have been described as phengites by previous authors (Lucassen, et al, 1999). The 'phengite' term is used to describe muscovite in which the Si:Al ratio is greater than 3:1 and in which the increase in Si is accompanied by susbtitution of Mg or Fe^{2+} for Al in octahedral sites (Deer, Howie and Zussman, 1992). It is essential to find out the amount of Fe^{3+} in the mineral phase, specially in white micas because it determines the *celadonite* component which gives information on pressure estimates.

White mica is present in the large majority of the metamorphic samples studied: white mica compositions from four samples (three mica schist and one amphibolite) are plotted in the triangle from Figure 4.6. This diagram is based on the triangular coordinates Si, Al and M^{2+}, but only di-octahedral micas where considered in it. In the same figure, it is seen that most of these compositions overlap, except the ones of sample FS-10-16C (amphibolite), where there is a slight migration towards the *muscovite* end member.

Structural formulae were calculated on the basis of 12 oxygens: table 4.4 shows averages of the number of Si per formula unit for the above mentioned samples.

These samples contain large, up to centimetric sheets of mica. Even if they come from a different lithology (amphibolite versus schist), these are distinct phengite laths following the main foliation. Phengites analyzed from the garnet mica schist (FS-10-09) are quite large (centimetric size) and make up the main component of the pervasive lepidoblastic foliation. Some of these (large) sheets show a slight zonation in the elements Fe, Mg and Ti, where Mg content shows the best zoning pattern. Si content was only x-ray imaged on sample FO-09-08, where it shows an increase in Si content towards the center of the laths.

Table 4.4: Summary table for the *#Si per formula unit (p.f.u.)* ranges for white micas in samples FS-10-09, FS-10-16A and FS-10-16C.

Sample	$\#Si$ p.f.u. Min	$\#Si$ p.f.u. Max
FS-10-09	3.127	3.176
FS-10-16A	3.127	3.152
FS-10-16C	3.119	3.237

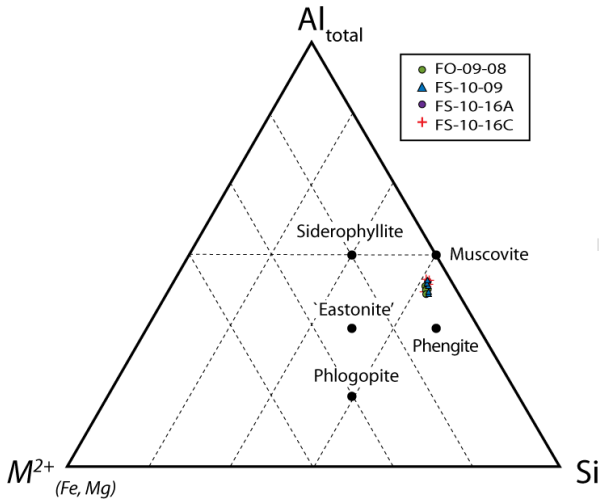

Figure 4.6: Principal variations in mica compositions for white micas based on the triangular coordinates Si, Al and M2+. The latter were calculated as *per formula unit*.

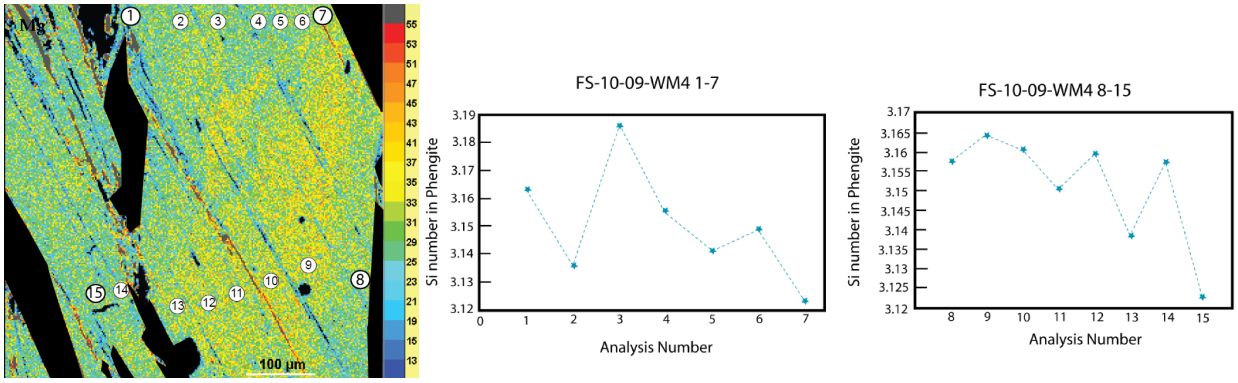

(a) White mica point analyses (b) #Si number in points 1-7 (c) #Si number in points 8-15

Figure 4.7: White mica elemental analyses and variation in the $\#Si$ p.f.u. in a phengite sheet from garnet mica schist (sample FS-10-09).

Tri-octahedral micas

Tri-octahedral micas correspond to the biotite group. Biotites in these metamorphic samples have strong pleochroism from clear to orange-red, showing a strong Mg component (towards phlogopite) although the pleochroism is a lot more marked in the amphibolite sample than in the mica schist, where its relation is almost 1 to 1. In sample FS-10-16A (plagioclase-mica schist), biotite makes up about 20% of the sample, and has a lot more Fe in its structure relative to Mg, leaning towards the Annite member. Classification is seen in Figure 4.8

Biotites in the amphibolite sample have an unusual high amount of Al in their structure: then their structural formula moves from the *annite-phlogopite* solid solution up to *siderophyllite-eastonite*. Ti appears in octahedral sites (up to 1.5% in these samples) replacing Al, but normally balanced by the exchange Al for Si^{4+}, sustitution that is favored by

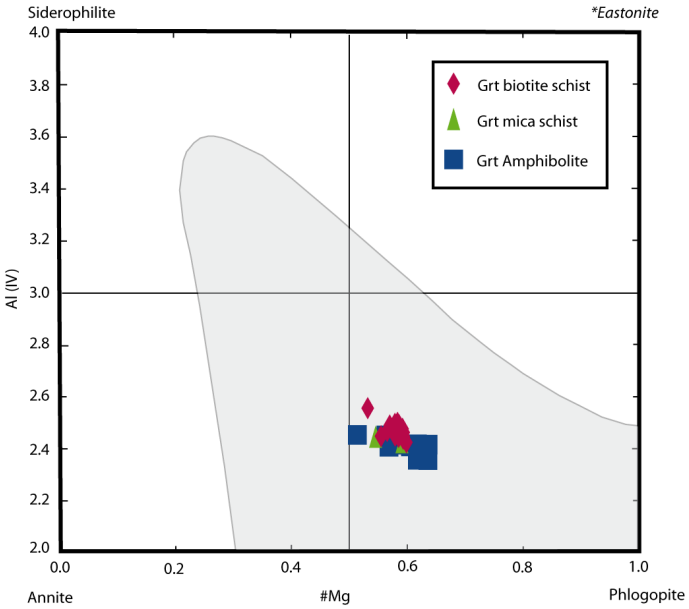

Figure 4.8: Al^4 vs $Mg/(Mg + Fe^{2+})$ diagram for biotite classification for two garnet mica schist (FS-09 and FS-16A) and a garnet amphibolite (FS-16C).

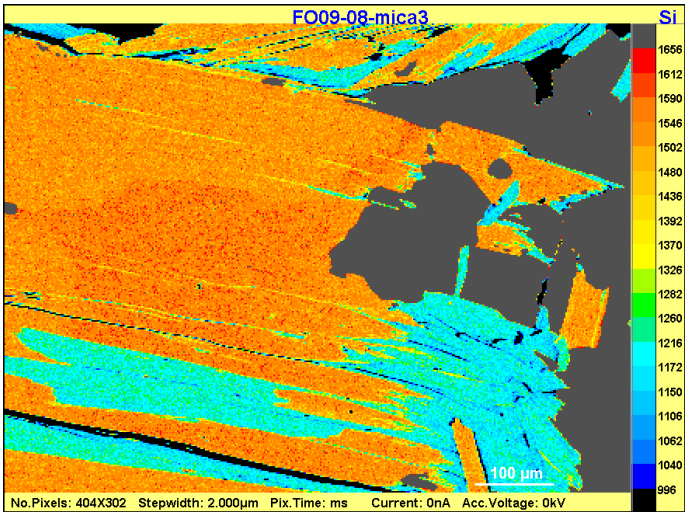

Figure 4.9: X-Ray elemental map of white micas and biotite for Si from a garnet mica schist sample (FO-09-08). White mica in recognizable in orange, and biotite in cyan. Color scale refers to counts per second of corresponding K_α ratiation.

high temperature (Deer, Howie and Zussman, 1992).

Chlorite

Chlorite per se can not be classified as any of the above mentioned micas: although these possess a layered structure which resembles mica, it is normally treated as a group apart (Deer, Howie and Zussman, 1992). The samples examined in this study belong to two main group of rocks: the granodioritic/dioritic samples belonging to the LVIC have chlorites with a composition that is quite different from the ones present in the metamorphic samples from the LVMC.

Chlorites on igneous rocks were not analyzed quantitatively and their petrographic description is already mentioned in Chapter 2. On the other hand, chlorites from metamorphic

are retrograde: overprinting the main foliation and altering previous ferromagnesian minerals, plus their birefringence is in the first order color range. Chlorite was only analysed with EMPA in sample FS-10-16A, and the formula calculated to 28 oxygens (Brandelik, 2009) gives the components: XSi=0.64, XMg=0.63 and XFe=0.36.

4.2.3 Amphibole

This phase is one of the most prominent phases in the studied samples. These make up the main component of the amphibolites, hence were studied exhaustively. Amphibolite samples studied with microprobe analysis were FS-10-11, FS-10-16A and FS-10-16C, and were classified with the $Ca-amphibole$ scheme seen in Diagram 4.10 (Hawthorne and Oberti, 2007). This scheme takes into account Mg and Fe^{2+} going in the C site, versus Si number (all cations are considered p.f.u.).

The majority of these analysis cluster in the pargasite field (because their Al^{4+} content was three times as their Fe^{3+} content), and the rest of them show a slight migration to the edenite field regardless of the sample.

Pargasite and edenite are phases in the boundary between calcic amphiboles and sodic-calcic amphiboles (Deer, Howie and Zussman, 1992); on the other hand, edenite seems to be a phase that comes from the temperature sensitive reaction $tremolite + albite = edenite + quartz$ (Spear, 1993), indicating a medium temperature field in the amphibolite facies.

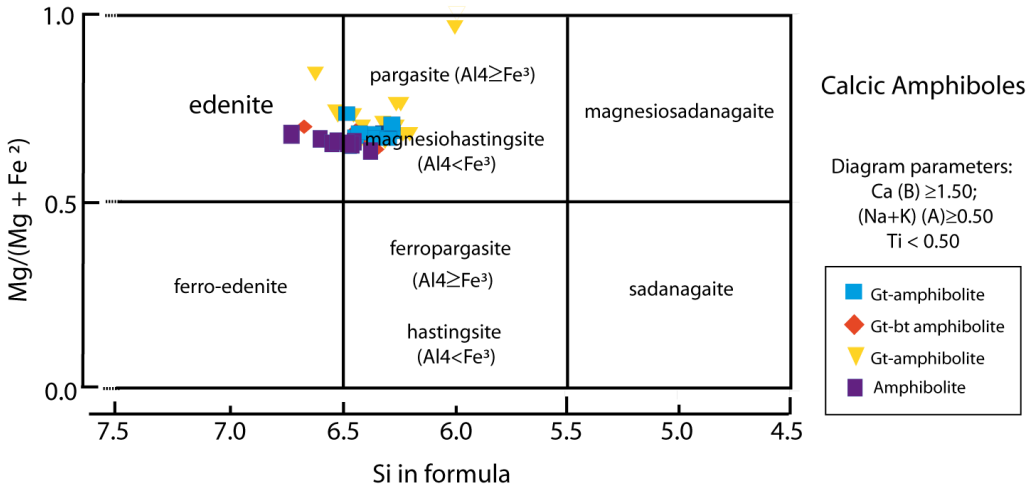

Figure 4.10: $Si p.f.u.$ vs $Mg/(Mg + Fe^{2+})$ diagram for Ca-Amphibole classification for the amphibolite samples FS-10-02 and FS-16C, and Grt-bt schist FS-10-16A *based on Hawthorne and Oberti, 2007.*

Although intermediate plutonic rocks were described in the petrography section which contained actinolite-hornblende, these amphiboles were not analyzed for major elements.

4.2.4 Epidote group

Epidote is also an important phase and used as mineral indicators in most samples. Epidote group phases were clinozoisite (CZo) and zoisite (Zo)on one hand, and Ce-bearing allanite on the other. Large CZo and Zo crystals were present throughout the amphibolite samples, making part of the nematoblastic foliation in them. These constitute 10 to 15% of the samples, and the mineral formulas were determined either with the aid of CALCMIN (Brandelik, 2008) or by hand and calculated to 12.5 Oxygens p.f.u.

Due to their optical characteristics (specially cleavage) CZo and Zo was easily confused with amphiboles, and then analyzed as such, which gave analysis only for sample FS-10-16A. These have an average formula of $Ca_2Al_2O \bullet Al_{0.9}Fe0.1(Si_2O_7)SiO_4$ (18 analysis). Representative oxide analyses are seen in Table B.5 from Appendix **??**.

Ce-bearing allanite is not a major phase and was only recognized in the same sample: fine grain, high relief, euhedral crystals that were located in the surroundings a the large plagioclase vein. These crystals have a strong concentric zoning, seen in the back-scattered electron image seen in Figure 4.11. Besides Ce, these were analyzed for La and Pr, their content were as high as 0.7% whereas Ce had 1.7% at its maximum.

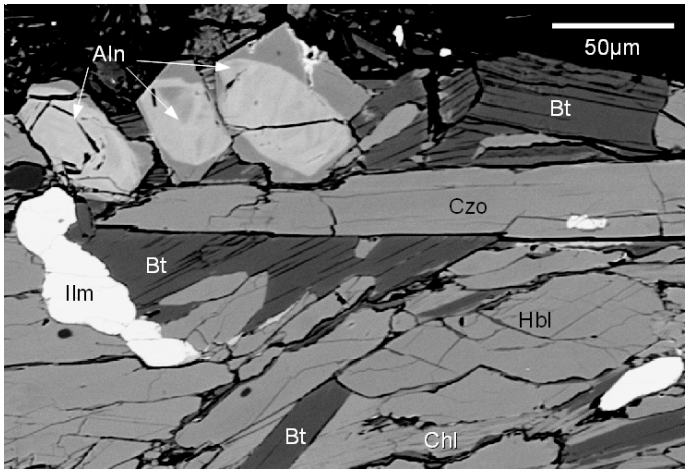

Figure 4.11: Back scattered electron image of nematoblastic minerals in a grt-bt schist (sample FS-16A). Note concentric zonation patterns in allanite (Aln).

4.2.5 Feldspars

It should be mentioned that feldspars represent around 10% of the metamorphic samples, and were analyzed in two amphibolite samples (FS-02 and FS-16C) and in a garnet biotite schist (sample FS-16A). The oxide analyses of these samples are seen in Table B.6 from Appendix B, and spots are plot in the feldspar classificatrion triangle from in Figure 4.12.

Feldspar in the amphibolite samples are strongly altered in the edges and completely anhedral, then these were measured only in the center of the crystals: these are both *alkali feldspar* and *plagioclase*, the plagioclase has a fairly homogeneous composition of $Ab75-79\%$. Because of their degree of alteration, it was not recommended to measure anywhere else in the crystals. Some plagioclase crystals also presented mechanical twinning and suturing.

As mentioned earlier, sample FS-16A is basically a sample of a deformed plagioclase vein cutting a garnet-biotite schist. Plagioclase from this sample has a composition that varies from 72 to 81% albite.

Hence, plagioclase belonging to these samples is *oligoclase* in composition.

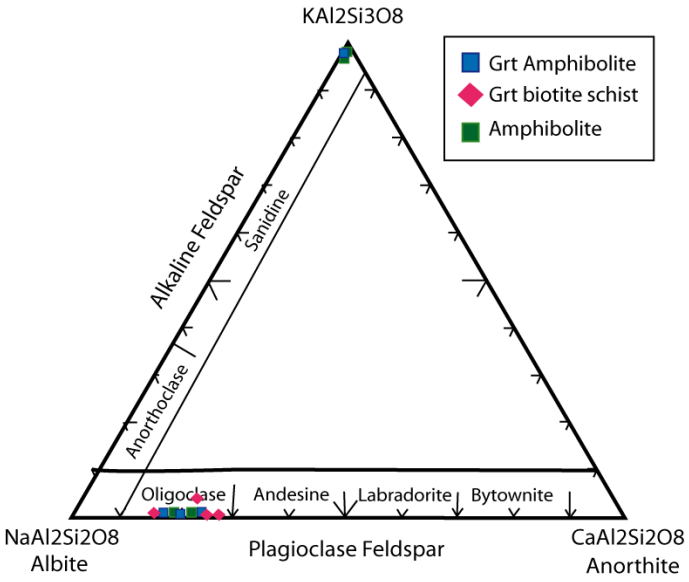

Figure 4.12: Feldspar classification triangle, for two amphibolite samples and a garnet-biotite schist.

4.2.6 Opaques and Accesory Minerals

Rutile

This Ti phase is present in all analyzed samples, but it was specially significant in sample FS-10-05 (strongly hematized garnet mica schist). Rutile crystals are really abundant making up to 5% of the sample and are present as inclusions or as independent phases in the sample. On the other hand, Ilmenite breaks down to rutile + chlorite: phases seen throughout most metamorphic samples.

Rutile was also a major inclusion in garnets, where in most cases had random orientations, but in other made up for a textbook-example of snowball garnet (Figure 3.3).

Opaques

Opaques are also a minor component in these samples, making up to 3% in amphibolites and mica schists. Opaques were mostly iron oxides and ilmenite, in special, one sample (FS-10-05) with a strong hematitization contained a large amount of opaques, even giving a red-rusty appearance to the rock.

Intermediate igneous rocks contain up to 5% opaques, these being hematite and magnetite mostly. Nevertheless, elemental analyses were not performed in opaque phases.

Other accesory minerals

Apatite, titanite and zircon are phases present in the above mentioned metamorphic samples, and each of these made up to 1% of the sample. A Ca-rich phase was only found as an inclusion in a garnet from the FS-10-16C grt-bt amphibolite sample, shown in Figure 4.13 and it is pressumed to be graphite.

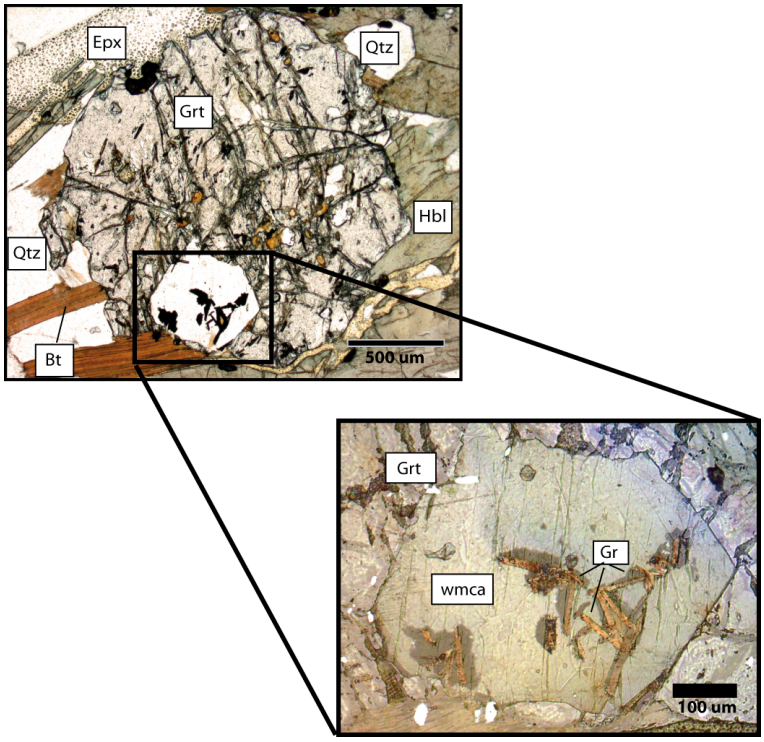

Figure 4.13: Poikiloblastic garnet with a phengite inclusion with a C-rich phase (possibly graphite) embedded in its surface. Garnet from a garnet amphibolite sample (FS-10-16C). Mineral abbreviations: *Epx*=epoxy, *Grt*=garnet, *Hbl*=hornblende, *Bt*=biotite, Qtz=quartz, *wmca*= white mica and *Gr*=graphite.

Chapter 5

Trace element geochemistry and geochronology

A critical stage in investigating the formation of a metamorphic complex is to determine the age at which the rocks assemblages were formed. For this purpose, a combination of different geochronometers (U-Pb in zircon, U-Pb in titanite and Sm-Nd in garnet) and thermochronometers (Ar-Ar dating in micas and hornblende) were used in order to develop a temporal history of the rocks of the Limón Verde metamorphic complex (LVMC).

The isotope data obtained were processed using the Isoplot 3.7/Excel macro provided by the Berkeley Geochronology center: the 'Probability Density' and 'Weighted Average' subroutines were used for plotting U-Pb data from zircon, and the 'Sm-Nd' routine was used for plotting garnet Sm-Nd isochrons.

Previously plublished geochronology results for the LVMC range through a wide span of geological time. Initial studies made by Hervé et al. (1985), gave Rb-Sr whole-rock isochron ages of 309 ± 11Ma, K-Ar ages in muscovite of 270-280 Ma, and K-Ar biotite ages between 230 and 250 Ma. On the other hand, data by Lucassen et al. (1999) determined a Sm-Nd age of peak metamorphism at ca. 270 Ma, and K-Ar ages of 236 ± 6 Ma in hornblende for metabasites, and 234 ± 5 Ma in biotite for gneiss (Lucassen calls gneisses what we call schists in the current study).

Age data presented in this work complement the existing ages and contribute to the development of a time history of the Limón Verde metamorphic complex (LVMC).

5.1 U-Th-Pb SHRIMP dating of zircon

Mica schist in the LVMC were subjected to medium to high temperature metamorphism (equivalent to amphibolite facies), these assemblages are suitable for the formation of metamorphic zircon and growth of metamorphic rims on pre-existing zircon grains. Two garnet bearing mica schist samples from different locations were selected for this work: sample FO-09-08 corresponds to a garnet-zoisite schist and FO-09-13 corresponds to a garnet bearing mica schist.

Representative cathodoluminescence (CL) images of the zircons from both samples are shown in Figure 5.1a and b, with circles on spots where the ages were obtained. Since the main scope of this study was to determine the age of metamorphic events, most of the analyses were performed on rims assuming that these represents the last stage of crystallization.

In sample FO-09-08, 41 grains and 47 spots were analysed; in sample FO-09-13, 50 grains were analysed. The individual calculated ages and their corresponding histograms plus probability density plots are seen in Figure 5.2 with errors within $1-\sigma$.

Zircon with a Th/U ratio higher than 0.5 most probably crystallized during igneous events (Hoskin and Schaltegger, 2007) rather than metamorphism. When such ages are obtained from the cores of zircon grains they are taken as representing provenance from igneous sources with a wide spread of ages. On the other hand Th/U ratios equal to or less than 0.1 are considered to represent metamorphic zircon. The zircon ages obtained were divided according to these characteristics and treated as different sets with the 'Probability Density' and the 'Weighted Average' sub-routines.

There is no radiogenic $^{207}Pb/^{206}Pb$ nor $^{207}Pb/^{235}U$ ratios for these analyses because there is too much common Pb and the ages are too young (less than 1 Ga.) thus the correction method used was the ^{207}Pb. Therefore we were unable to assess condordance in the normal manner for ^{204}Pb corrected data.

In general, the U-Pb zircon ages from these two samples are too young (less than 1 Ga.) to be treated with a *Concordia* diagram (neither Wetherill nor Tera-Wasserburg) because the lower portion corresponding to the youngest ages has a steep slope and no longer a curve but a straight line. This line overlaps with the *Discordia* curve (when Pb loss exists) making the Concordia analysis unclear (Kamo, S. 2012 *personal comunication*).

Ti and rare earth elements were also measured as part of trace element study in the

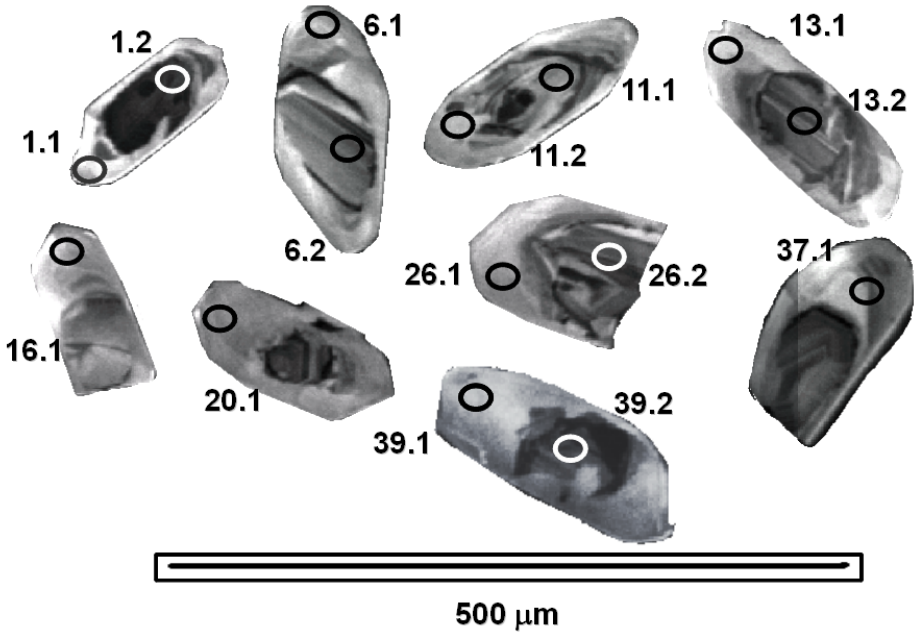

(a) Zircons from a garnet zoisite schist (FO-09-08)

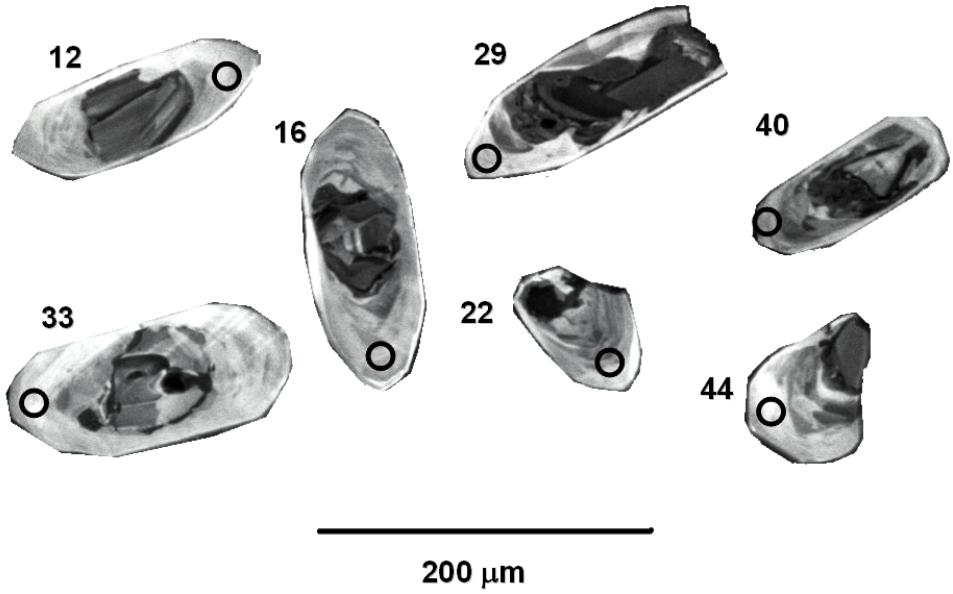

(b) Zircons from a garnet mica schist (FO-09-13)

Figure 5.1: Cathodoluminescence images of representative zircons, showing a dark detrital core and a brighter metamorphic rim. Circles and numbers represent the spot and number of analysis.

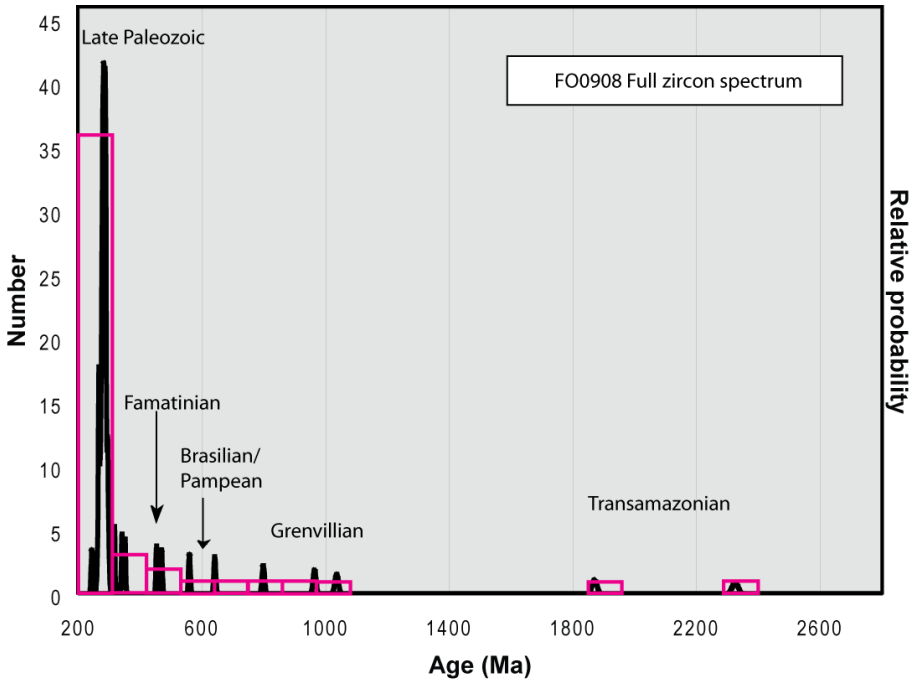

(a) Sample FO-09-08: 41 grains

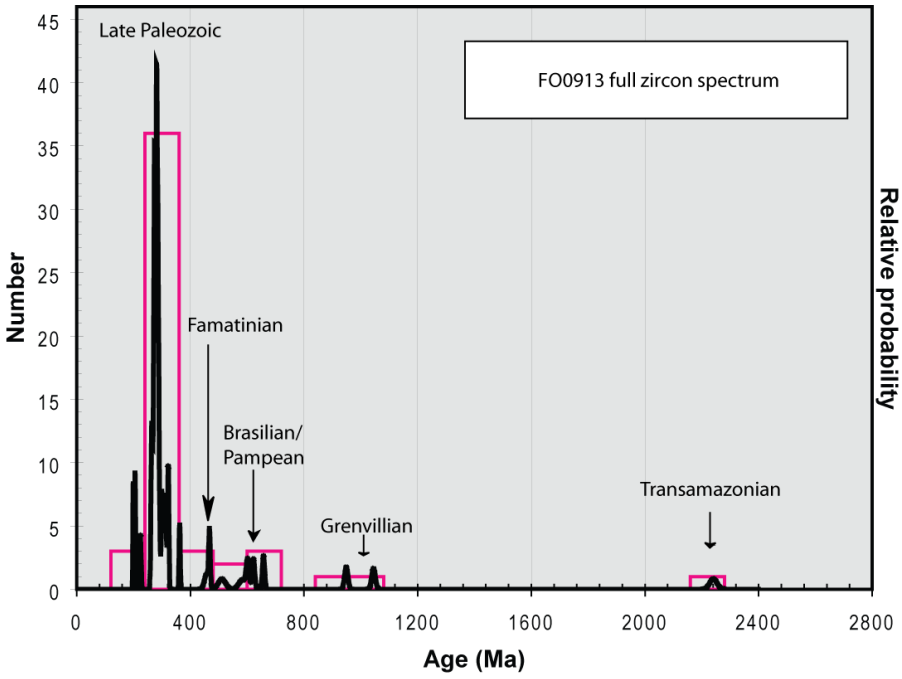

(b) Sample FO-09-13: 50 grains

Figure 5.2: Probability density ages for U-Pb zircon dating for the two samples of mica schist: FO-09-08 and FO-09-13.

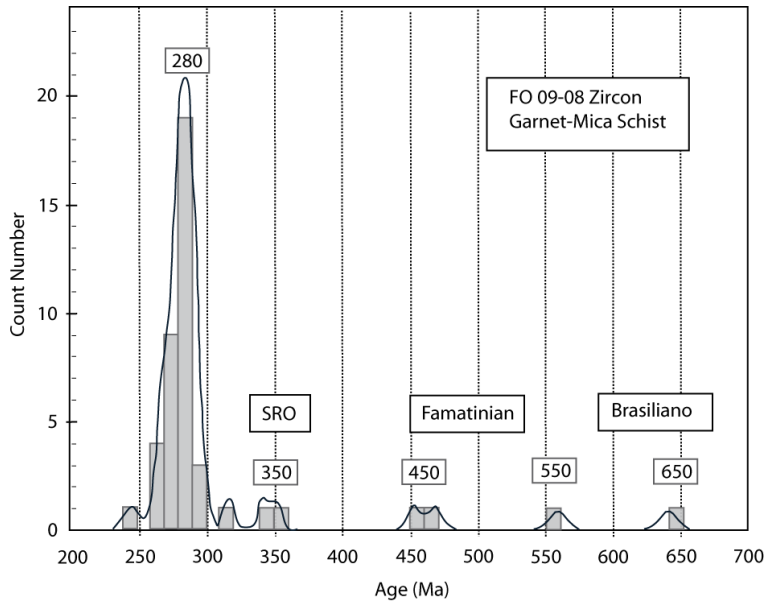

(a) Sample FO-09-08: 41 grains

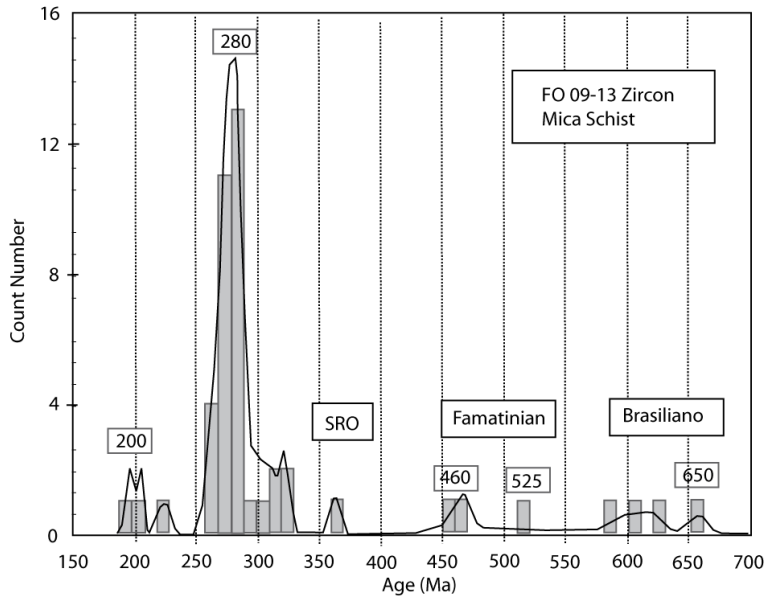

(b) Sample FO-09-13: 50 grains

Figure 5.3: Probability density ages for U-Pb zircon dating for the two samples of mica schist: FO-09-08 and FO-09-13 considering all the grains younger than Neo-Proterozoic (700Ma). Events older than 700 Ma are largely scattered and shift the peaks of this ages. SRO stands for San Rafael Orogeny. Events younger than than 250 Ma may represent sample contamination or Pb loss, thus are excluded from the rest of the analyses.

same spots measured earlier for U-Th-U in the same mica schist sample (FO-09-08). Ti was measured in order to determine the temperature of crystallization of zircon, by using the Ti-in-zircon thermometer of Ferry and Watson (2005). On the other hand, rare earth elements and their patterns help to understand the conditions of formation of zircon, indicating whether they were formed in an igneous or a metamorphic setting (Hoskin and Schaltegger, 2002).

Zircon rims from sample FO-09-08 present a clear metamorphic rim (cathodoluminescence image in Fig. 5.1), and their chondrite (OC) normalized-REE paterns are seen in Figure 5.4a. On the same figure, there is an image summarizing Hoskin and Schaltegger experiments concerning REE partitioning during metamorphism. Both images have REE plot in the same scale for easier comparison, then it is seen that the rims of zircon from sample FO-09-08 (Fig. 5.1) present a slight enrichment in heavy REE.

The REE patterns appear in between prismatic crystal growth in equilibrium with melt and, subsolidus growth in equilibrium with garnet according to Hoskin and Schaltegger's experiment (2002). This feature may indicate possible anatexis and/or migmatization during the crystallization of rims in zircon (visit `www.dropbox.com/sh/upm3e53ps45nn1g/5rm2rabhh4` for full sets of isotope and geochronology data).

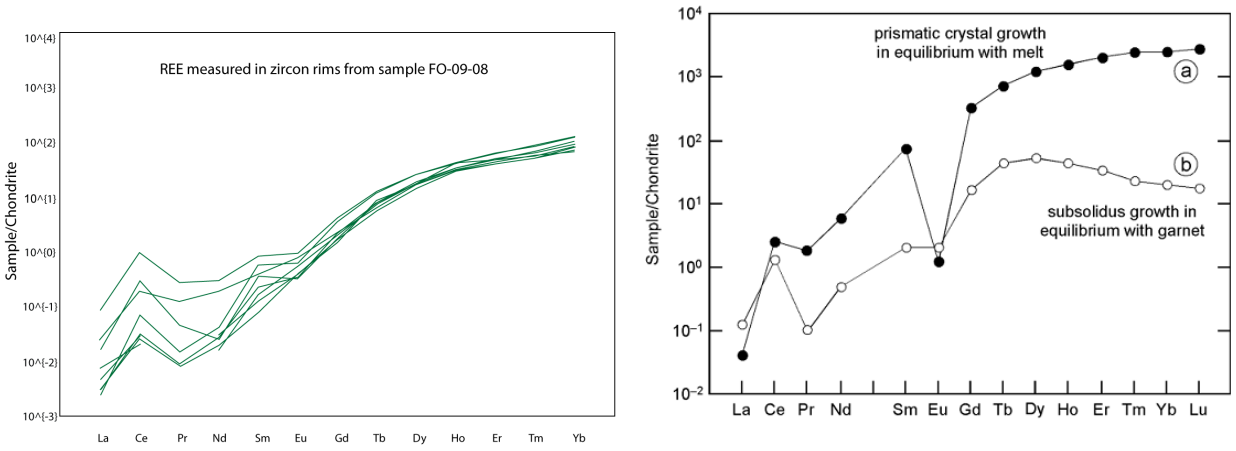

(a) Metamorphic rims (sample FO-09-08)

(b) Hoskin and Schaltegger experiments

Figure 5.4: Chondrite normalized representative REE patterns for metamorphic zircon equilibrated with a melt phase (a) and zircon equilibrated with garnet (b) under subsolidus conditions (Hoskin and Schaltegger, 2002).

5.1.1 Igneous core in zircon

Although both samples present zircons with one or two igneous characteristics (igneous textures and Th/U ratios higher than 0.5), zircons from sample FO-09-13 have particularly clear igneous patterns as a whole and thus are used in a separate analysis. Zircon grains from sample FO-09-08 do not present Th/U ratios higher 0.5, and even their cores present Th/U values between 0.2 and 0.5. Nevertheless, their REE information (seen in the Appendix) shows that they had a prismatic crystal growth in equilibrium with melt indicating that they are probably igneous.

Typical zircons with igneous characteristics from sample FO-09-13 and their corresponding ages are shown in Figure 5.5: all such ages obtained in this sample are from the cores of zircon grains. It is noted that these cores have strongly zoned cathodoluminescence patterns: both concentric oscillatory and euhedral oscillatory (Corfu, 2003). It is also seen that the igneous cores show a darker cathodoluminescence compared to the rest of the zircon from the same sample seen better in Figures 5.1a and 5.1b

At least, one interpreted igneous inheritance in sample FO-09-13 is plotted in Figure 5.6 in a weighted average diagram. In this case, the weighted average is 311 ± 11 Ma. Where there is only two million years of concordance.

However, many of these ages fall in the range 295-325 Ma, strongly suggesting a predominant Late Carboniferous igneous provenance in the sedimentary protolith of the FO-09-13 schist. A few other ages range from approximately 470 to 620 Ma with a single determination of ca. 2240 Ma.

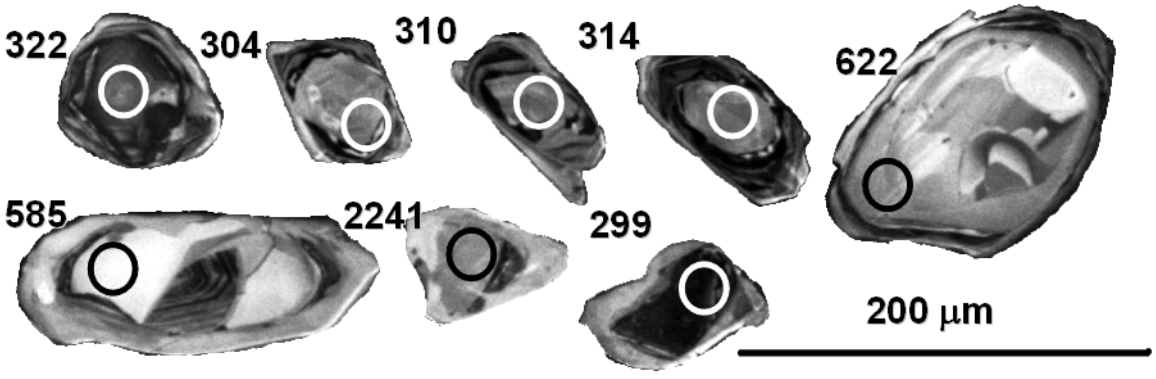

Figure 5.5: Zircons interpreted to be igneous detrital from sample FO-09-13 with their corresponding age sites. Ages in Ma.

Table 5.1: U-Pb ages from igneous zircon in sample FO-09-13

Grain. spot	**U-Pb age (Ma)**	**error (Ma)**	**Th/U**
14.1	322	5	1.496
15.1	323	4	0.552
17.1	310	5	1.235
18.1	585	28	1.292
27.1	299	3	0.671
31.1	467	5	0.486
41.1	622	9	0.831
43.1	2241	26	0.681
48.1	304	5	0.619
49.1	314	7	1.042

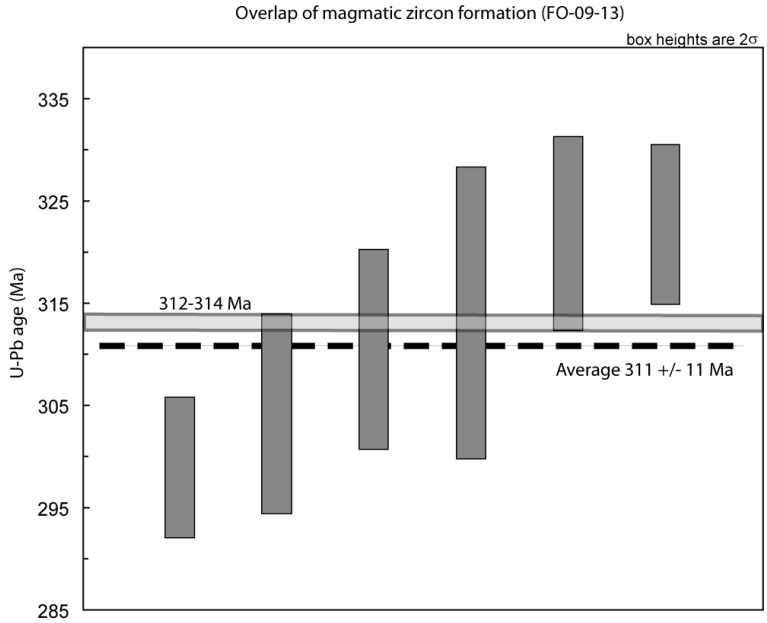

Figure 5.6: Weighted average plot of the U-Pb ages from zircons interpreted to be igneous. Ages greater than 400 Ma are excluded. The weighted average is 311 ± 11 Ma and it is observed that there is an overlap roughly between 312 to 314 Ma.

5.1.2 Metamorphic rims in zircon

Mean closure temperature of the U-Pb system has been calculated to be less than 900^oC, based on its experimentally determined diffusion parameters (Cherniak and Watson, 2000). The minimum temperature for the growth of zircon crystals is about 300^oC (in hydrothermal systems). Thus there is a 600^oC range where metamorphism could potentially contribute to the formation of zircon rims.

The analysed detrital zircons, exhibit at least these two stages of growth, which is explained by the igneous nature of the detrital core, in many cases reduced by sedimentation and erosion overgrown by new metamorphic zircon. Figure 5.7 shows a group of representative zircons from sample FO-09-08 where the core is inherited and the rim is overgrown, the dates and spots of the analyses are also shown in the same image.

As mentioned earlier, the REE analysis of zircon rims in sample FO-09-08 present patterns that are a mixture between zircon in equilibrium with a melt phase, and also subsolidus crystallization in equilibrium with garnet. This is important to consider, because garnet will be used as the principal geothermometer in the mica schist, in addition, the Ti in zircon thermometer, will deliver the necessary information to calculate the metamorphic crystallization of zircon.

Rim analyses which have Th/U less than 0.1 give ages that cluster around a 280 Ma peak in both samples (seen in histogram versus probability density ages from Figures 5.9 and 5.8) which constraints the time of metamorphic zircon crystallization. The probability plot of calculated radiogenic ages in sample FO-09-08 shows a dominant peak at ca. 280 Ma, There is a slight tail on the younger age side what may reflect that some areas have suffered radiogenic lead loss. In the probability plot, the ages range between 260 to 300 Ma with a weighted mean of 281 ± 3 Ma (MSWD=2.5, excluding some ages from the peak Fig.5.8).

Metamorphic ages from sample FO-09-13 range from 250 to 310 Ma, seen in the probability plot from Figure 5.9 with a simple dominant gaussian distribution in the Permian, inferring that this is the crystallization age for the metamorphic zircon. On the other hand, the sample has a weighted mean of 278 ± 3 albeit with an unacceptably high MSWD of 3.6. In both cases a few extreme values were excluded from the means as indicated in Figure 5.9b.

Table 5.2: U-Pb ages from zircon rims interpreted to be metamorphic

FO-09-08				FO-09-13			
Grain. spot	**U-Pb age (Ma)**	**error (Ma)**	**Th/U**	**Grain. spot**	**U-Pb age (Ma)**	**error (Ma)**	**Th/U**
1.1	243	5	0.006	1.1	275	4	0.004
2.1	263	7	0.006	2.1	268	4	0.004
3.1	266	3	0.013	3.1	287	4	0.005
5.1	278	4	0.005	4.1	273	5	0.005
6.1	273	5	0.014	5.1	277	5	0.004
7.1	280	6	0.008	7.1	280	4	0.004
8.1	277	4	0.004	8.1	279	6	0.005
9.1	294	4	0.004	9.1	279	4	0.005
10.1	281	5	0.004	10.1	264	7	0.005
11.2	287	5	0.004	11.1	273	6	0.005
12.1	280	4	0.005	12.1	276	5	0.007
13.1	282	5	0.004	16.1	281	5	0.005
14.1	289	3	0.018	20.1	511	26	0.004
15.1	286	5	0.012	22.1	273	4	0.004
16.1	283	5	0.004	23.1	281	6	0.004
17.1	283	4	0.004	24.1	275	5	0.004
19.1	316	4	0.058	25.1	282	4	0.004
20.1	282	5	0.004	26.1	286	5	0.006
21.1	286	5	0.004	28.1	264	6	0.004
22.1	294	4	0.005	29.1	283	4	0.004
24.1	271	4	0.004	30.1	283	5	0.004
25.1	278	4	0.005	32.1	281	4	0.007
26.1	282	9	0.004	33.1	286	5	0.005
27.1	298	5	0.046	34.1	306	17	0.005
28.1	286	5	0.005	35.1	285	3	0.05
29.1	273	11	0.004	36.1	263	4	0.009
30.1	266	4	0.005	37.1	458	17	0.004
31.1	287	4	0.005	38.1	224	5	0.005
32.1	287	6	0.005	40.1	273	4	0.004
33.1	275	4	0.011	44.1	271	4	0.004
34.1	277	6	0.006	46.1	290	5	0.004
35.1	288	4	0.004	47.1	288	9	0.004
36.1	277	6	0.005				
37.1	266	4	0.005				
38.1	280	5	0.006				
39.1	283	5	0.004				
40.1	350	4	0.066				
41.1	288	4	0.004				

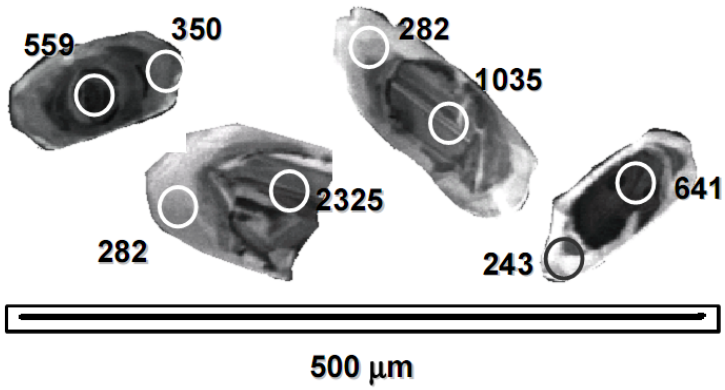

Figure 5.7: Representative detrital zircons from sample FO-09-08 with their corresponding age sites in the inherited core and rim. Ages in Ma.

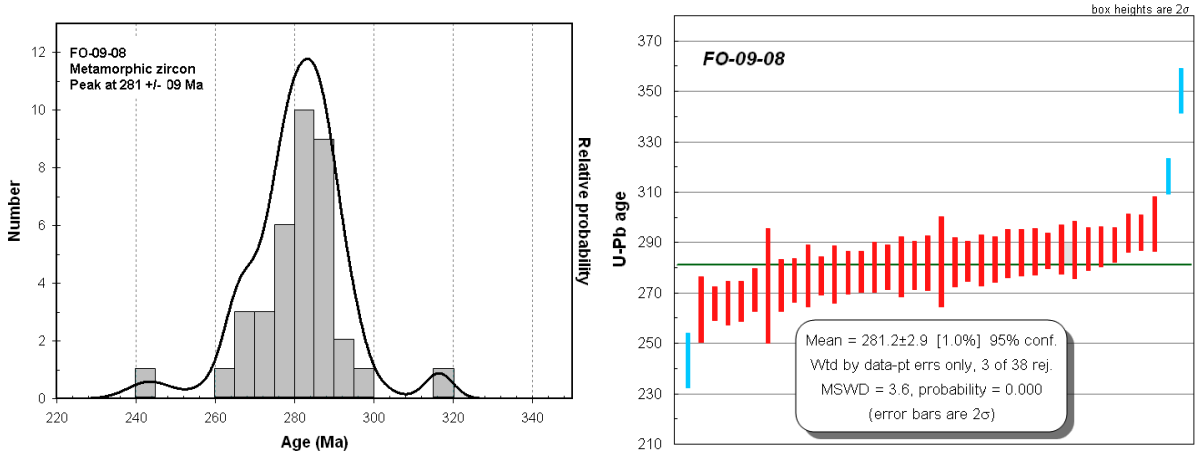

(a) Histograms and probability density plots

(b) Weighted average

Figure 5.8: U-Pb ages from sample FO-09-08 interpreted to be metamorphic

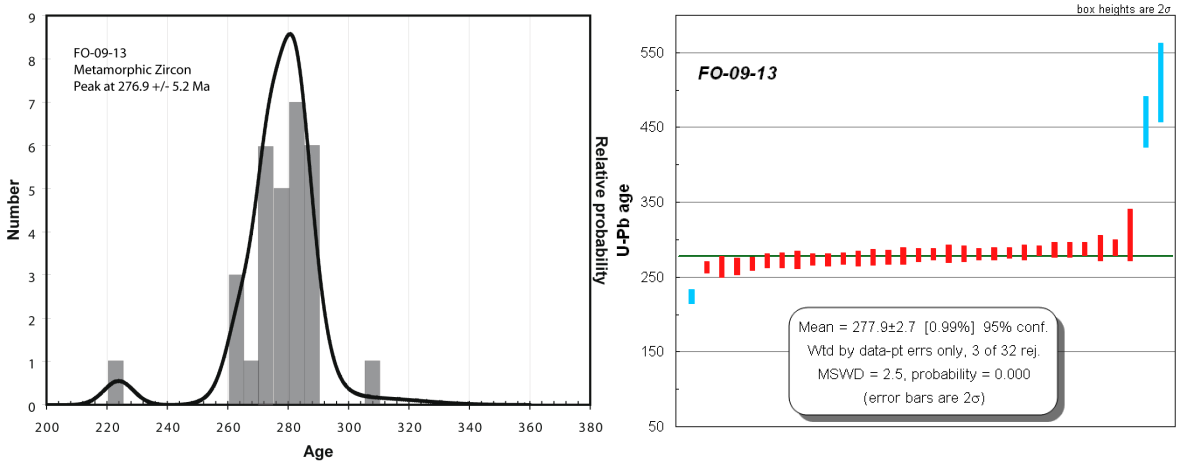

(a) Histograms and probability density plots

(b) Weighted agerage age determination

Figure 5.9: U-Pb ages from sample FO-09-13 interpreted to be metamorphic

5.2 U-Pb SHRIMP dating of titanite

The dating of mafic metamorphic rocks has presented a problem since it does not form zircons to be easily dated with U-Pb. On the other hand, titanite is a fairly abundant metamorphic mineral phase in the amphibolite samples from this study, and a good candidate for dating the metamorphism of mafic rocks with U-Pb. The blocking temperature of the system is at ca. 625^{o}C (Dickin, 2005).

Sample FS-10-02 contains up to 2% titanite thus it was chosen for U-Pb dating. It is also seen in this sample that some titanite crystals present a rutile corona or vice-versa (rutile reacting to titanite), seen in Fig.5.10b. On the same image, a back-scattered electron image shows titanites glowing agains a dark background (Fig. 5.10a).

Detailed mechanical and analytical procedures are described in Ch.2: Methodology. Titanite mineral concentrates were handpicked and dated by SHRIMP II, where U, Th and Pb (and their isotopes) were measured. 20 titanite crystals were analysed, from which 21 ages were obtained.

Metamorphic titanite from this amphibolite sample (FS-10-02) is colorless and translucent, it is also depleted in U and dominated by common Pb so the normal means of calculating radiogenic 206Pb/238U ages using the 207Pb correction method does not work (Fanning, 2013 personal communication). Using the 'zircon extractor age' routine in ISOPLOT, the obtained age is 272.88 + 25.91 -37 Ma, with 97.9% confidence from a coherent group of 10. But this age is not reliable due to the common Pb correction.

However, one can do a 3 dimensional linear fit to the measured ratios, using the method of ISOPLOT/Ludwig (2012) for Tera-Wasserburg (T-W) concordia. One uses the measured 204Pb/206Pb as the third dimension; which constrains the common Pb. There is a considerable extrapolation to the radiogenic intersection on the T-W concordia curve seen in Figure 5.10, and so necessarily the uncertainty in that intersection is high. Nevertheless one can see that the likely crystallization date for the titanite is Triassic ca. 243 ± 26 Ma, generally in accord with the zircon data for FO-09-08 and FO-09-13. Despite the large error in the calculated age, the MSWD is only 0.66, proposing that the age of metamorphism is reliable.

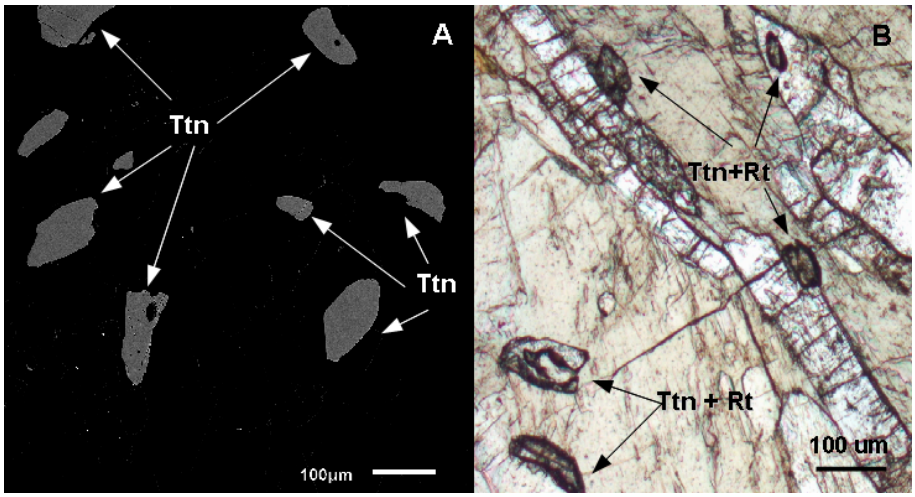

(a) A: Back scattered image of titanites from amphibolite sample FS-10-02. B: Thin section image of the same amphibolite sample with emphasis in Ti bearing phases

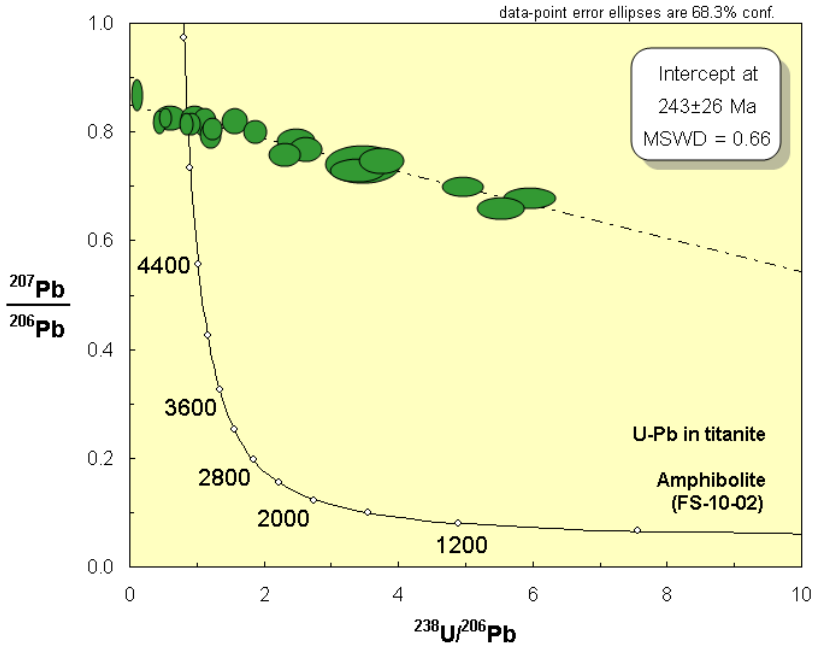

(b) 3D linear regression of Tera-Wasserburg concordia of 21 points

Figure 5.10: U-Pb dating of titanites from the amphibolite sample FS-10-02.

5.3 Sm-Nd isochron dating of whole rock-garnet

Sm-Nd dating is based on the alpha decay of the ^{147}Sm to ^{143}Nd isotopes, with a half life of $1.08x10^{8}$ years (Vernon and Clarke, 2008).

One important advantage of this method with respect to Rb-Sr and K-Ar dating is that the ratio of parent to daughter isotope concentration are not thought to vary significantly during metamorphism. In the case of the other mentioned methods, metamorphism distorts this ratio and the radiogenic daughter isotopes may be preferentially lost to the system, yielding unreliable dates.

It is possible to use this method to date metamorphic events by applying it to minerals that grow during the metamorphism, providing that they have reasonably high Sm/Nd ratios. Such a mineral is garnet and an age may be calculated from the Sm-Nd isotope data of garnet compared to another phase with which it was in equilibrium during metamorphism - the bulk composition is often taken as this second phase-. In the case of zoned garnets the contents of REE, Y and also Sm/Nd may vary significantly from one zone to another. Providing that the zones grew during the same metamorphic and geochemical conditions, isochrons may be constructed from a data for bulk rock and different zones.

Garnets for analyses were handpicked from a garnet-mica schist (sample FS-10-09) and a garnet-bearing amphibolite (sample FS-10-16C).

- FS-10-09: This sample contains a seriate size distribution of equant garnets. *It is assumed that the chosen garnets for sample were large (1 to 2 mm) and that these also possess a strong major element zoning pattern.* The isochron age obtained from whole rock - garnet core - garnet rim is 375 ± 13 Ma.

- FS-10-16C: This sample contains a bimodal size distribution for garnet, most of these contain inclusions such as quartz, graphite, rutile, white mica and titanite. No monazite inclusions were observed in BSE. The isochron age obtained from whole rock - garnet core - garnet rim is 380 ± 21Ma.

In a first set of analysis, whole garnets were crushed into powder and these and the whole rock powder were analyzed with TIMS: the point age calculations are shown in Table 5.3 and in Fig. 5.11. The garnet mica schist sample (FS-10-09) keep an age 227 ± 14Ma.

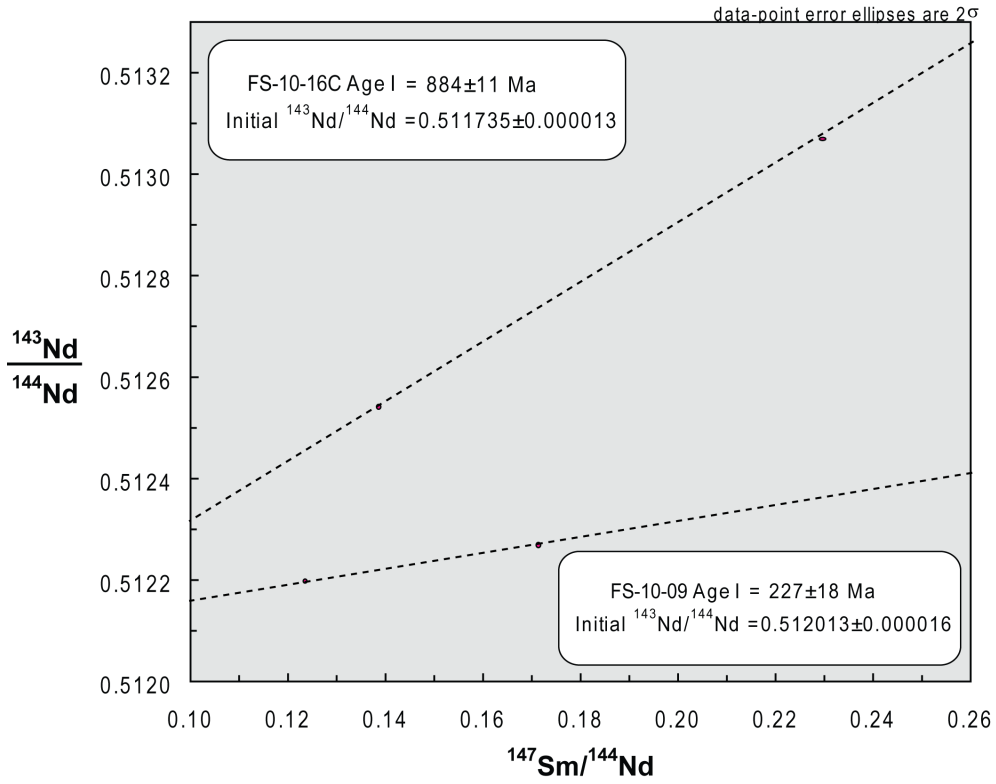

Figure 5.11: First set of Sm-Nd isochron ages in garnet and bulk rock for a garnet mica schist (FS-10-09) and a garnet bearing amphibolite (FS-10-16). Error ellipses are equivalente to 2σ.

Table 5.3: Sm-Nd data sets obtained from TIMS analyses in garnets and whole rock for samples FS-10-09 and FS-10-16C. I. For first set of analyses. *WR* stands for Whole Rock, *Gt* stands for garnet, *c* for core and *r* for rim.

Sample	Sm	Nd	Sm/Nd	147Sm/143Nd	143Nd/144Nd	std%
09 WR I	5.351	26.127	0.2048	0.12380	0.51219	0.0006
09 Grt I	1.345	04.750	0.2839	0.17162	0.51226	0.0009
16C WR I	3.947	10.381	0.3802	0.22988	0.51306	0.0006
16C Grt I	2.450	10.888	0.2296	0.13879	0.51254	0.0008

A second (isochrons from Figure 5.12)and a third set (Fig. 5.13) of Sm-Nd age determinations were made using three analyses for each of these sample: whole rock and two points in garnet (core and rims). The garnets were sampled with a micromill on the core and rim of the garnet, and the dust obtained was analysed by TIMS (*it is assumed that the selected garnets were larger and showed a strong zoning pattern*). In the second set, the isochron ages obtained correspond to 380 ± 21 Ma for the garnet amphibolite (FS-10-16C), and 375 ± 13 Ma for the garnet mica schist.

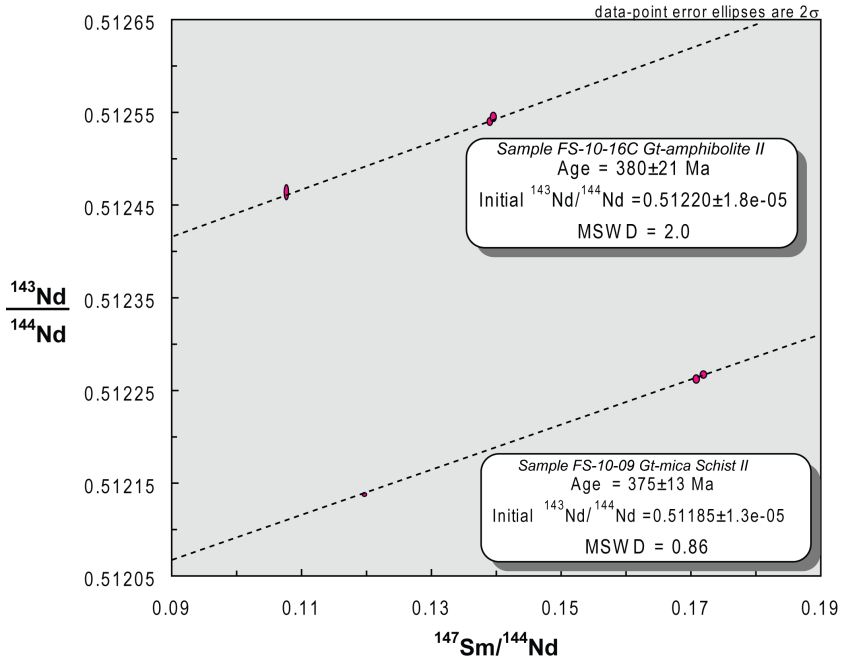

Figure 5.12: Second set of Sm-Nd isochron ages in garnet and bulk rock for a garnet mica schist (FS-10-09) and a garnet bearing amphibolite (FS-10-16). Error ellipses are equivalente to 2σ.

Despite the heterogeneity and lack of concordance of Sm-Nd results, one final attempt to get an isochron age was done. Seven data points from the garnet mica schist (sample FS-10-09) were plotted in Figure 5.13: data point ellipses are equivalent to 2σ, and there is a dotted isochron with a scarce correlation between the points, exposed by the MSWD number of 173.

Finally, the isochron age from these seven points is 384 ± 58, reinforcing the ca. 380 age obtained with earlier results and seen in isochrons from both samples in Fig. 5.12.

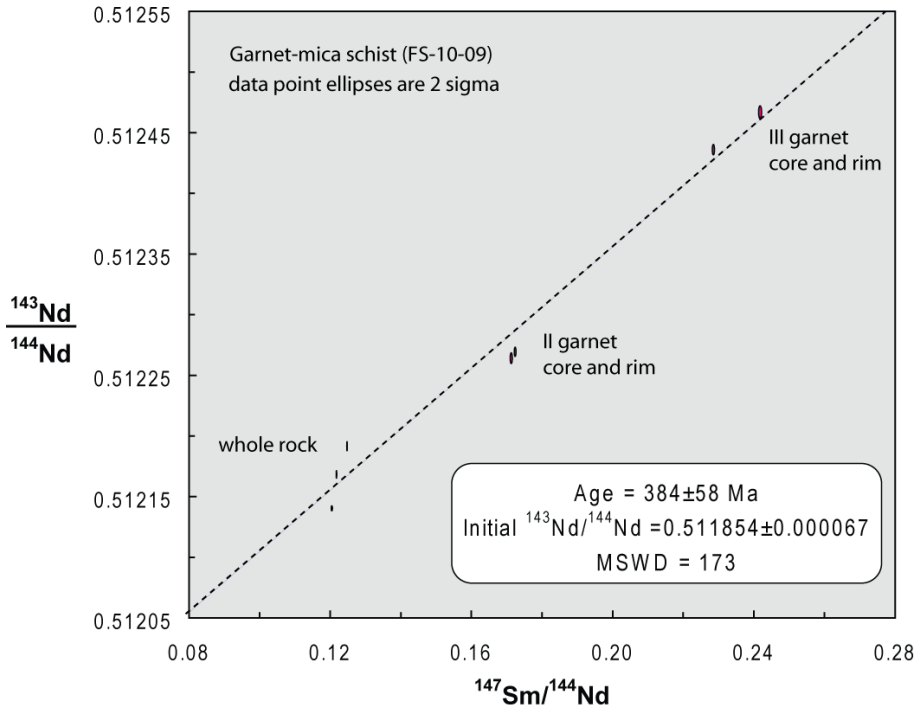

Figure 5.13: Sm-Nd isochron age in garnet and bulk rock for a garnet mica schist considering 7 points (FS-10-09). Error ellipses are equivalent to 2σ.

Table 5.4: Second (II) and third (III) sets of Sm-Nd data. *WR* stands for Whole Rock, *Grt* stands for garnet, *c* for core and *r* for rim.

Sample	Sm	Nd	Sm/Nd	147Sm/143Nd	143Nd/144Nd	std%
09 WR II	4.963	25.103	0.1977	0.119517	0.512139	0.0003
09 Grt-c II	1.345	4.750	0.2839	0.171624	0.512268	0.0006
09 Grt-r II	1.348	4.782	0.2819	0.170544	0.512263	0.0007
09 WR III	9.075	45.387	1.999	0.120870	0.512167	0.0005
09 Grt-c III	1.129	2.825	0.3993	0.241381	0.512466	0.0008
09 Grt-r III	1.211	3.224	0.3756	0.228002	0.512435	0.0007
16C WR II	5.013	28.212	0.1777	0.107511	0.512464	0.00013
16C Grt-c II	2.661	11.552	0.2302	0.139362	0.512545	0.0008
16C Grt-r II	2.450	10.888	0.2296	0.138797	0.512540	0.0007
16C Grt-c III	3.384	15.047	0.2249	0.135950	0.512482	0.0006
16C Grt-r III	3.391	15.102	0.2245	0.136296	0.512484	0.0006

5.4 Calculation of ϵNd and T_{DM}

Calculated epsilon Nd values are a measure of the difference between the initial ratio of the sample suite and *Chondritic Uniform Reservoir* (CHUR) at the time of formation (Rollingson, 1993). Also, the Nd model ages (T_{DM}) are generally applied to dating the time of crustal separation from the mantle (Dickin, 2005).

The Nd isotopic compositional ranges can also indicate a possible source for the amphibolite. When comparing the $^{143}Nd/^{144}Nd$ value of the garnet amphibolite sample of *0.51246* with reference values in literature (Rollingson, 1993 *and references therein*), it is obtained that:

- Continental flood basalts (Western USA and Paraná) flucuate between 0.51224 and 0.51278, and
- Subcontinental lithosphere (Scotland, Eastern China and Mass. Central) fluctuate between 0.510967 and 0.513203.

Also, the isotope values obtained in the previous section (5.3), were used (garnet-mica schist FS-10-09 and garnet amphibolite FS-10-16C) for the calculation of the ϵNd and Nd mantle model ages: these were based on two ages, one obtained from the U-Pb age of metamorphism in zircons, and the other from Sm-Nd whole rock-garnet isochron data. The data calculated is shown in Table 5.5.

Table 5.5: ϵNd data for a garnet mica schist (FS-10-09) and a garnet amphibolite (FS-10-16C). $t_1 = 280Ma$ and $t_2 = 380Ma$. M refers to Michard et al. and G refers to Goldstein et al. calibration

Sample	$^{147}Sm/^{144}Nd$	$^{143}Nd/^{144}Nd$	ϵNd t_0	ϵNdt_1	ϵNdt_2	T_{DM}(M)	T_{DM}(G)
FS-10-09	0.11956	0.51213	-9.91	-7.16	-6.17	1456	1682
FS-10-16C	0.10747	0.51246	-3.47	-0.28	0.86	865	1014

The garnet mica schist sample has an ϵNd t_0 value of -9.91, indicating that this sample comes from a strongly differentiated crust, moreover this is consistent with the hypothesis that the protolith for this sample is sedimentary.

The garnet amphibolite sample has an ϵNd t_0 value of -3.47 which is a lot lower than expected for a basaltic protolith: this may indicate that there is significant addition of juvenile material or that it is highly differentiated either confirming that the protolith is a

within-plate basalt with significant crustal contamination. As mentioned earlier in the same section, the $^{143}Nd/^{144}Nd$ value of this sample is similar to that of continental flood basalts and subcontinental lithosphere, making the origin of the amphibolite unclear.

According to Balhburg, et al. (2009) *and references therein* data, the II region in Northern Chile holds a felsic basement crust has an average Nd T_{DM} of 1.6 Ga, which is comparable with the data obtained from the garnet mica schist from the LVMC. Data by Lucassen et al, 1999 indicates an average T_{DM} of for felsic rocks from Sierra Morreno and Caleta Loa in agreement with the current data. Nevertheless, data from amphibolites (garnet and zoisite bearing, similar to the ones used in this sudy) by Lucassen, et al (1999) presents T_{DM} ages of 0.80 and 0.87 Ga.

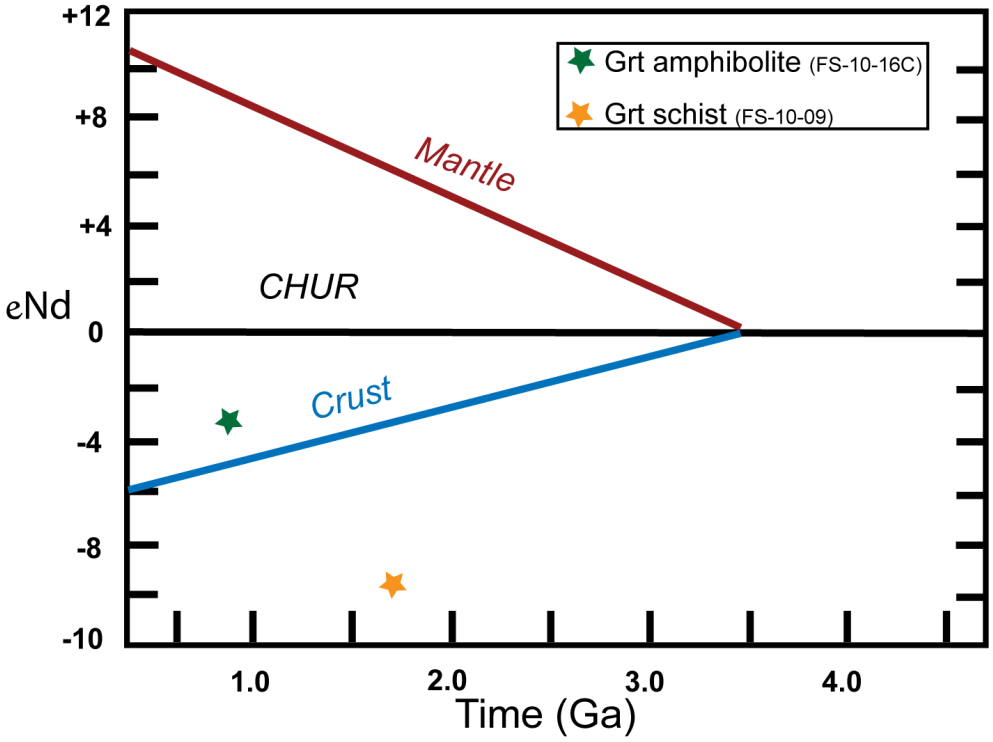

Figure 5.14: Evolution of bulk earth, crust and mantle for ϵNd diagram. Samples FS-10-09 and FS-10-16C are also included in the diagram for comparison.

It is important to notice that even though the Sm-Nd ages of metamorphism obtained in this work are not in agreement with ages from Lucassen et al. (1999), who indicate that the age of metamorphism occurrs at ca. 270 Ma, they have similar Nd-depleted mantle model ages. Therefore, they can be related to a similar crustal recycling process.

5.5 $^{40}Ar/^{39}Ar$ dating

$^{40}Ar/^{39}Ar$ dating is based upon the K-Ar dating, where K is a major element making up ca. 1.5% in the Earth's Crust. K is abundant in rock forming minerals such as K-feldspars, amphiboles and micas (Dickin, 2005; Braun et al. 2006).

Argon, although a secondary constituent of the crust, is rare enough that it is usually not considered as part of the mineral at the time of crystallization. Specially in subcortical conditions of high pressure and high temperature, such as the ones found in metamorphic settings.

Ar can be extracted stepwise by heating the sample over a range of temperatures below that of fusion. ^{40}Ar and ^{39}Ar behave essentially identically during extraction (Braun et al. 2006). Systems that open and may lose argon by diffusision, must be studied by the Ar-Ar technique (Dickin, 2005).

Blocking temperatures of these systems in different minerals makes the $^{40}Ar/^{39}Ar$ method suitable to date retrograde metamorphism or cooling of a rock. Muscovite has a blocking temperature of 350 ± 50^0C, whereas hornblende has a blocking temperature of 530 ± 30^0C (Rollingson, H. 1993). Biotite has a blocking temperature that varies according to the crystallization setting i.e. if biotite forms in a hydrothermal setting the blocking temperature will be different than in an igneous environment, this difference in bocking temperature can be of at least 150^0C (Braun, et al. 2006). Nevertheless, biotite is often ascribed a nominal closure temperature for argon of ca. 300 ± 50^0C.

The initial $^{40}Ar/^{36}Ar$ atmorpheric ratio=295.5±0.5. Note that the errors in ages represent 2σ confidence level.

Three mineral phases from two samples were studied by this method funded by SERNA-GEOMIN, in the frame of the Moctezuma and Sierra Gorda maps (Plan Nacional): hornblende from an amphibolite (FS-10-02) and, biotite and white mica from a garnet mica schist (FS-10-09), from where it was obtained that:

- Hornblende from amphibolite: The step heating of fresh metamorphic amphibole (hornblende) was done in 6 steps, with no loss of Ar involved. The Apparent age versus Cumulative %^{39}Ar Released in Figure

  As mentioned earlier, the blocking temperature of this system is 530 ± 30^0C. Thus it is

used to date early stages of retrograde metamorphism, even some authors (Lucassen et al, 1999) have used Ar-Ar dating of hornblende in amphibolite to date the metamorphic peak. This will be subject of discussion in following chapters.

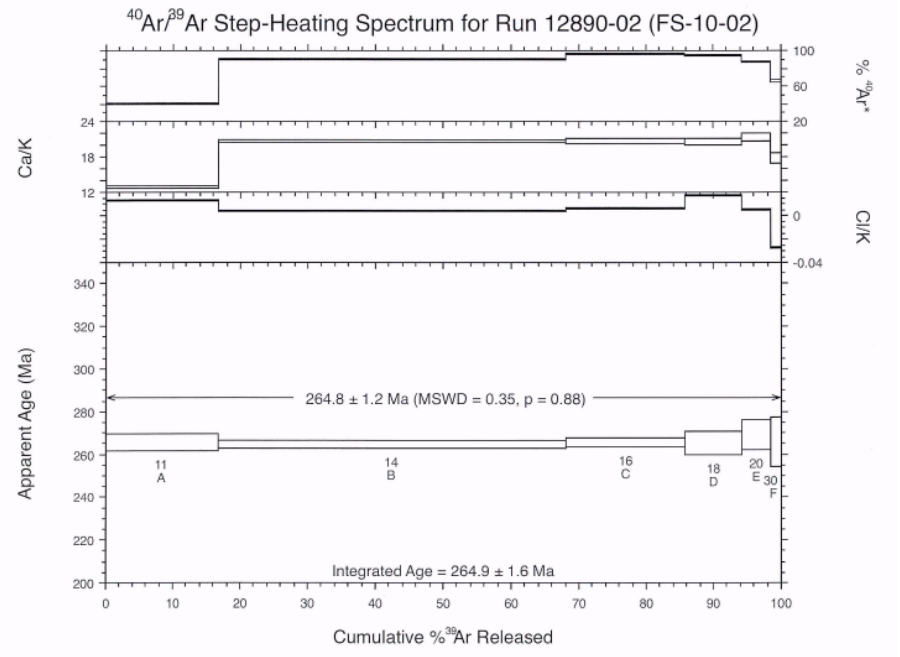

Figure 5.15: Ar-Ar step heating for hornblende in amphibolite (sample FS-10-02).

- White mica in grt-mica schist: Fresh laths of metamorphic white mica were obtained from sample FS-10-09, where the step heating of white mica was done in 7 steps, with no loss of Ar involved. 6 of these steps were used to obtain a plateau age of 263.0 ± 0.6 Ma, with an MSWD=0.93 (Figure 5.16. On the other hand, the isochron age obtained in the same run is of 262.9 ± 1.2 with an $^{40}Ar/^{36}Ar$ intercept of 300 ± 30.

  The blocking temperature of the Ar-Ar system in white mica is 350 ± 50^0C, therefore the age obtained in this run suggests a stage in the cooling history of the rock.

- Biotite in grt-mica schist: Fresh metamorphic biotite crystals were obtained from a grt-mica schist (FS-10-09) where step heating of biotite was done in 7 steps, from which 5 of them give a plateau age of 251 ± 0.5 Ma (Figure 5.17). The isochron age obtained with 5 points is 250.6 ± 0.7 Ma, MSWD=0.29 with an $^{40}Ar/^{36}Ar$ intercept of 312 ± 14.

  Eliminating the low temperature first two steps it was possible to obtain an isochron with little excess Ar, obtaining an age slightly younger than the one obtained in the plateau but concordant.

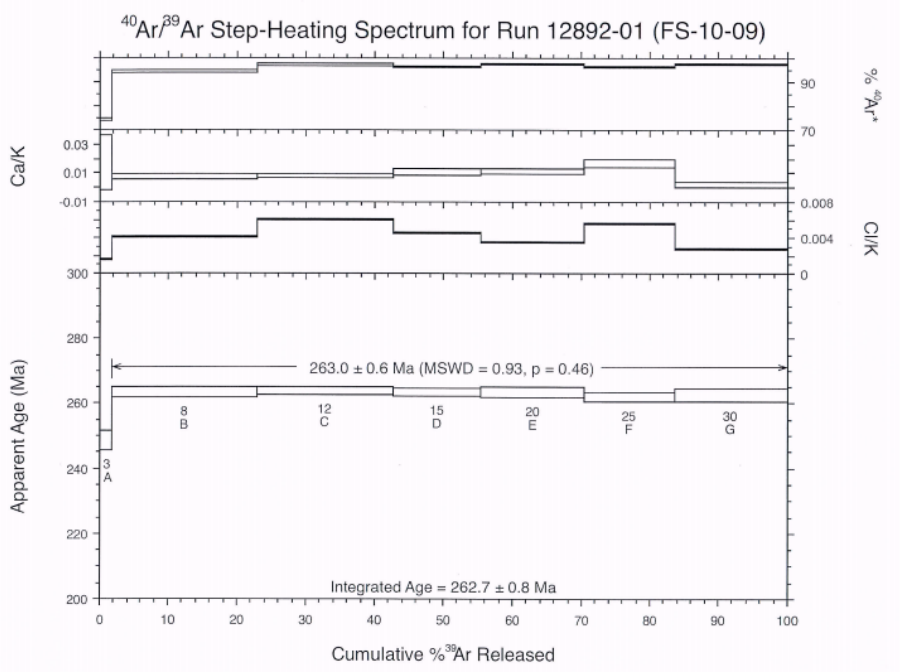

Figure 5.16: Ar-Ar step heating for white mica in grt-mica schist (sample FS-10-09).

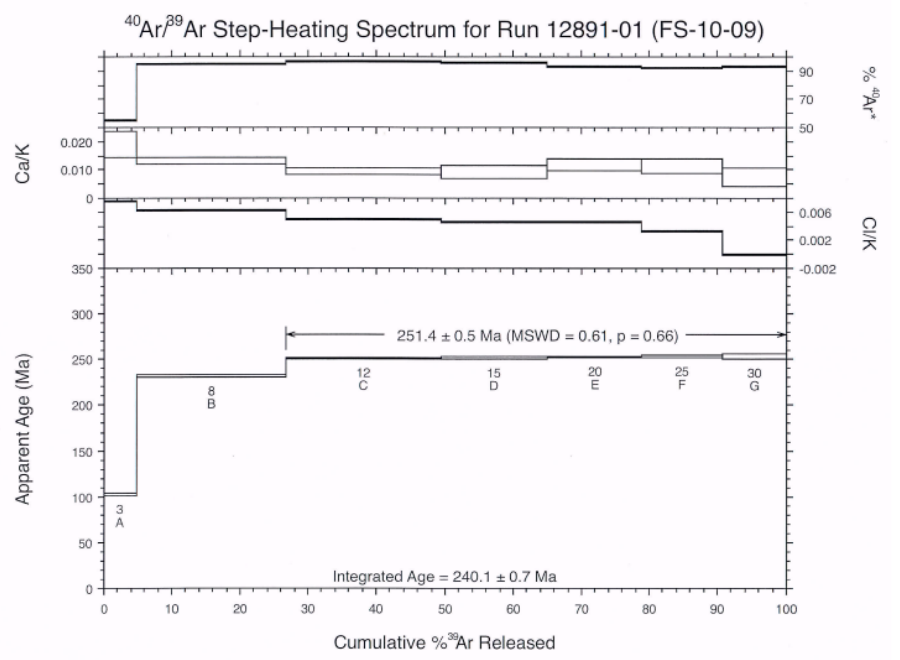

Figure 5.17: Ar-Ar step heating for biotite in grt-mica schist (sample FS-10-09).

Ar-Ar dating in the schist, gave a white mica plateau age of 263 ± 1.2 Ma and a biotite plateau age of 251.4 ± 1 Ma. The ages of white mica and biotite are not concordant, thus it is possible that biotite has minor alteration which did not affect white mica (probably chloritization).

Chapter 6

Geothermobarometry

6.1 Classic geothermobarometry

Although initial calculations were obtained with forward modeling (PTX) pseudosections in $Perple_{\chi}$, we also performed classic thermobarometric calculations in order to get another parameter to compare the results to. The chosen geothermobarometers were the garnet-biotite thermometer, the garnet-muscovite-plagioclase-quartz geobarometer (a variation of the $garnet - aluminosilicate - SiO_2 - plagioclase$ barometer) using the mineral chemistry results from Chapters 4.

6.1.1 Garnet-Biotite Cation Exchange Geothermometer (Ferry & Spear, 1978)

This thermometer, probably the most used geothermometer, is based on the temperature sensitive reaction: Almandine + Phlogopite = Pyrope + Annite.

$$Fe_3Al_2Si_3O12 + KMg_3AlSi_3O_{10}(OH)_2 = Mg_3Al_2Si_3O_{12} + KFe_3AlSi_3O_{10}(OH)_2 \quad (6.1)$$

The simplified equation for this calculation is given in equation 6.2

$$\ln K_{Fe-Mg}^{gt-bt} = (\frac{52108}{3R})\frac{1}{T} + \frac{19.51}{3R} - P(\frac{0.238}{3R})\frac{1}{T} \quad (6.2)$$

where

$$K_{Fe-Mg}^{gt-bt} = \frac{\frac{X_{Fe}^{bt}}{X_{Mg}^{bt}}}{\frac{X_{Fe}^{bt}}{K_{Mg}^{bt}}} = \frac{(Fe/Mg)^{bt}}{(Fe/Mg)^{gt}} \quad (6.3)$$

`GPTmodified.xls` is a program that calculates pressure-temperature estimates based on the above mentioned reactions. This program is a simplified version of the `GPT.xls` program created by J. Reche and F. Martinez in 1996 and published in Computers and Geosciences. `GPTmodified.xls` makes use of cation p.f.u. on the basis of 12 Oxygens for both biotite and garnet. These calculations use $R = 8.1314 J/mol \cdot K$, P in bars and T in Kelvins. Core-to-rim garnet analyses were correlated with edge-to-center biotite data.

Table 6.1: Temperature estimates modeled with `GPTmodified.xls+`

Sample	Position Grt	Position Bt	T intersection ^oC
FS-10-09	Core	Core	525-540
FS-10-09	Rim	Rim	590-610
FS-10-16C	Core	Core	370
FS-10-16C	Rim	Rim	525

6.1.2 Garnet-Muscovite-Plagioclase-Quartz (GMPQ)

The GMPQ barometer is a solid solution barometer, which is thermodynamically independent from other barometers suitable for metapelitic compositions. The GMPQ barometer has the advantage of giving pressure estimates between 0.8-11.1 kbar with an error of ± 1.5 kbar in the absence of aluminosilicates and biotite (Wu et al, 2006.) It is based on the reactions:

$$pyrope + grossular + muscovite + quartz = anorthite + Mg - celadonite$$
$$almandine + grossular + muscovite + quartz = anorthite + Fe - celadonite$$

This geobarometer could only be used for sample FS-10-16A, where a large plagioclase vein (most of the thin section) cross-cuts a garnet- biotite schist. Results obtained were:

$$T = 751^oC - 803^oC \text{ and } P = 12.9 - 13 \pm 1.5 kbar$$

6.2 Ti in zircon thermometry

Zircon is a common accessory mineral in felsic rocks: in the case of schists it is an abundant mineral phase used for dating metamorphism. Isotope results are shown in the previous chapter (chapter 5). Zircon has the characteristic that its essential structural constituents

Zr, Si and Ti can replace one another to a limited extent in depending on temperature. Therefore the amount of Ti in zircon is used as a thermometer.

The combined experimental and natural results of Watson (2006) define a log linear dependence of the content of Ti in equilibrium (*parts per mil*) upon inverse temperature (Watson, et al. 2006).

$$log(Ti_{zircon}) = (6.01 \pm 0.03) - \frac{5080 \pm 30}{T(K)} \tag{6.4}$$

Zircon crystallization temperature estimates have been calculated with the Ferry & Watson (2007) equations assuming saturated activities for $a_{SiO_2} = 1$ and $a_{TiO_2} = 1$.

Zircons from sample FO-09-08 were analyzed for Ti and REE in the same spots where the ages were obtained in metamorphic rims and inherited cores with SHRIMP II. The spots where the analyses were taken are seen in Figure 5.1.

Crystallization temperature estimates for the metamorphic rim average 556 ± 7^oC for 9 points with respect to the 91500 zircon standard, using the calibration mentioned earlier and have a median of 556^oC. On the other hand, inherited cores from the same sample range between 673 and 743^oC.

Table 6.2: Temperature of metamorphic zircon crystallization based on the content of Ti. Content of Ti en ppm relative to standard 91500

Grain spot	Age (Ma)	error (Ma)	Ti (ppm)	error (ppm)	T (^oC)
FO0908-1.1	243	5	0,91	0,48	562
FO0908-6.1	273	5	0,77	0,41	551
FO0908-11.1	280	6	0,74	0,49	549
FO0908-13.1	277	4	0,84	0,46	556
FO0908-16.1	283	5	0,91	0,51	562
FO0908-20.1	282	5	0,86	0,47	558
FO0908-26.1	282	9	0,83	0,37	556
FO0908-37.1	266	4	0,98	0,43	566
FO0908-39.1	283	5	0,68	0,38	543
Average					**556**
median					**556**
std deviation					**7**

6.2.1 Summary classic geothermobarometry

Previous work by Lucassen, et al (1999) gave a reference temperature of 660^oC, and a pressure of 11 kbar for peak metamorphic conditions.

In the samples where the Ferry and Spear (1993) garnet-biotite thermobarometer was applied, i.e. in garnet mica schist (FS-10-09) and garnet amphibolite (FS-10-16C), the temperature obtained ranges between $525 - 610^o$C. It is worth to mention that metamorphic zircon crystallization temperatures from a similar garnet mica schist (sample FO-09-08) range between $543 - 566^o$C with an average of 556^oC.

In sample FS-10-16A the temperature obtained is specially high compared to the rest of the samples. This plagioclase vein represent an open system and normally this result would be dismissed: on the contrary, the temperature obtained from this sample represents the temperature when this veining was active.

Regarding geobarometers, it was difficult to calculate pressure estimates in the amphibolite samples, because most of the pressure-sensitive reactions involve a combination of garnet-aluminosilicates-plagioclase. And the samples worked in this thesis lacked the above mentioned paragenesis.

6.3 Forward modeling with PTX pseudosections

6.3.1 Garnet bearing mica schist

Samples FS-10-09 and FO-09-08 correspond to this lithology, a garnet-bearing mica schist with a paragenesis of $Wmca + Bt + Grt + Qtz + Plag + Zo \pm Rt$.

A detailed analysis of the phases present in these two samples is described in Chapter 3. Because of their psamopelitic nature, these were expected to contain aluminosilicates (Al_2SiO_5), which does not happen, neither does contain Al-rich minerals such as staurolite or cordierite.

It is important to consider that the Ar-rich phases mentioned early have very narrow temperature ranges, and as found through pseudosections and classic thermobarometry, metamorphic peak temperatures do not match the temperatures stable for formation of them. Nevertheless, phyllosilicates and garnet do contain Al in excess in their structure.

Water was considered in excess ($3 - 6\%$) in the modeling of these pseudosections and the *melt* phase was considered into the calculations taking into account that a granitic and/or pelitic composition would melt at temperatures as low as 500^oC as seen in Figure 6.1 according to Ernst's 2009 experiments. The pseudosections produced for these samples are seen in Figures 6.2 and 6.4.In both samples, the melt curve in has a similar behavior: at pressures lower than 5 kbar, they start melting at an unusually low temperature of ca. 670^oC, then shifting to even lower temperature as the pressure rises. In sample FS-10-09 the lowest melting temperature (610^oC) occurs at 10-11 kbar; in sample FO-09-08 the lowest melting temperature (600^oC) occurs at a similar pressure.

- FS-10-09: It was observed petrographically that there is a strong chloritization of garnet and biotite in certain areas of the slide, at the same time, there are laths of white mica with no preferred orientation and overprinting older textures. The pseudosection from Figure 6.2 indicates that white mica present in all the fields except for one, and that sillimanite and melt are created to the expense of white mica.

  Magnetite and ulvospinel are present in the whole section: some major reactions are highlighted in the pseudosection, for instance where chlorite dissapears from the sample.

  There is currently no evidence of anatexis in the sample which may be due to two

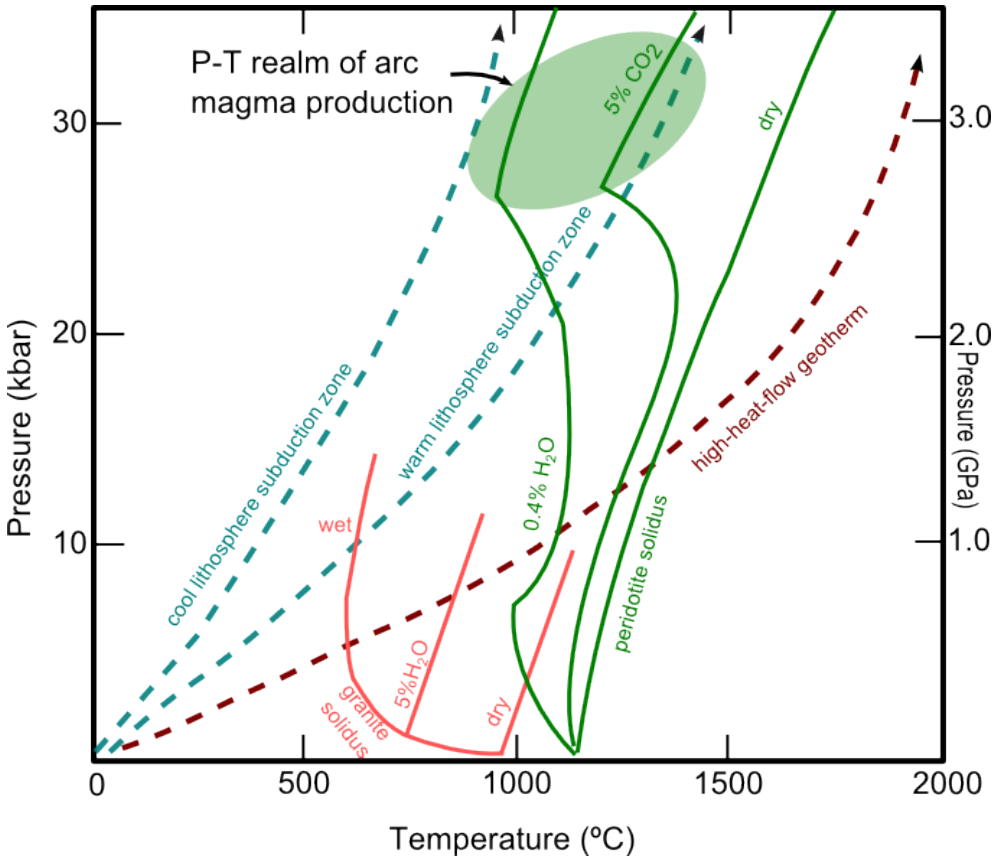

Figure 6.1: Experimentally determined melt curves for granite (continental crust) and peridotite (oceanic crust) at different amounts of water (Ernst, 2009).

reasons: there was never the necessary conditions for melt to appear in this sample. Or that, if the melt formed, it later recrystallized with a similar stress regime.

- FO-09-08: This sample is quite similar to the one described previously, and the pseudosection shows a sharp line with the disappearance of chlorite from the sample. In thin section it is seen that chlorite is altering biotite, nevertheless, the rock is fresh.

The compositional isopleths of this sample were created from the garnet major fraction components (Fe, Mg, Ca, Mn) and for the number of si per formula unit in white mica (formula based on 12 oxygens). These numbers were obtaine dfrom the existing geochemistry results from Chapter 4. A summary chart for both samples are seen in Table 6.3.

The spessartine (Mn) component of garnet was very low in both samples, and its high diffusion rate makes the Mn isopleths unrealiable, therefore they were dismissed from the final result.

In sample FS-10-09, the almandine (Fe) and grossular (Ca) components have similar but opposite patterns and depending on the PT range, they are good barometers or good termometers. The pyrope component (Mg) in garnet has a well defined pattern for a good termometer, in the same way the Si number in white mica has also a well defined pattern as a good barometer.

In sample FO-09-08, isopleth results are not as clear as in sample FS-10-09 for the almandine and grossular components, where these have patterns that are neither good termometers nor good barometers. On the other hand, the pyrope component isopleths are a good termometer and the Si number in white mica isopleths are a fairly good barometer. The intersection of the analyses from core and rim of Grt #1 are seen in Figures 6.5e and f.

Table 6.3: Isopleths values for samples FS-10-09 and FO-09-08 for the phases garnet, phengite and biotite

		FS-10-09		FO-09-08	
Phase	Component	Min.	Max	Min	Max
Garnet	Grossular	0,08	0,21	0,18	0,24
	Pyrope	0,12	0,19	0,10	0,18
	Almandine	0,49	0,81	0,57	0,63
Phengite	# Si p.f.u.	3,13	3,18	3,10	3,20
Biotite	# Mg	0,53	0,58	-	

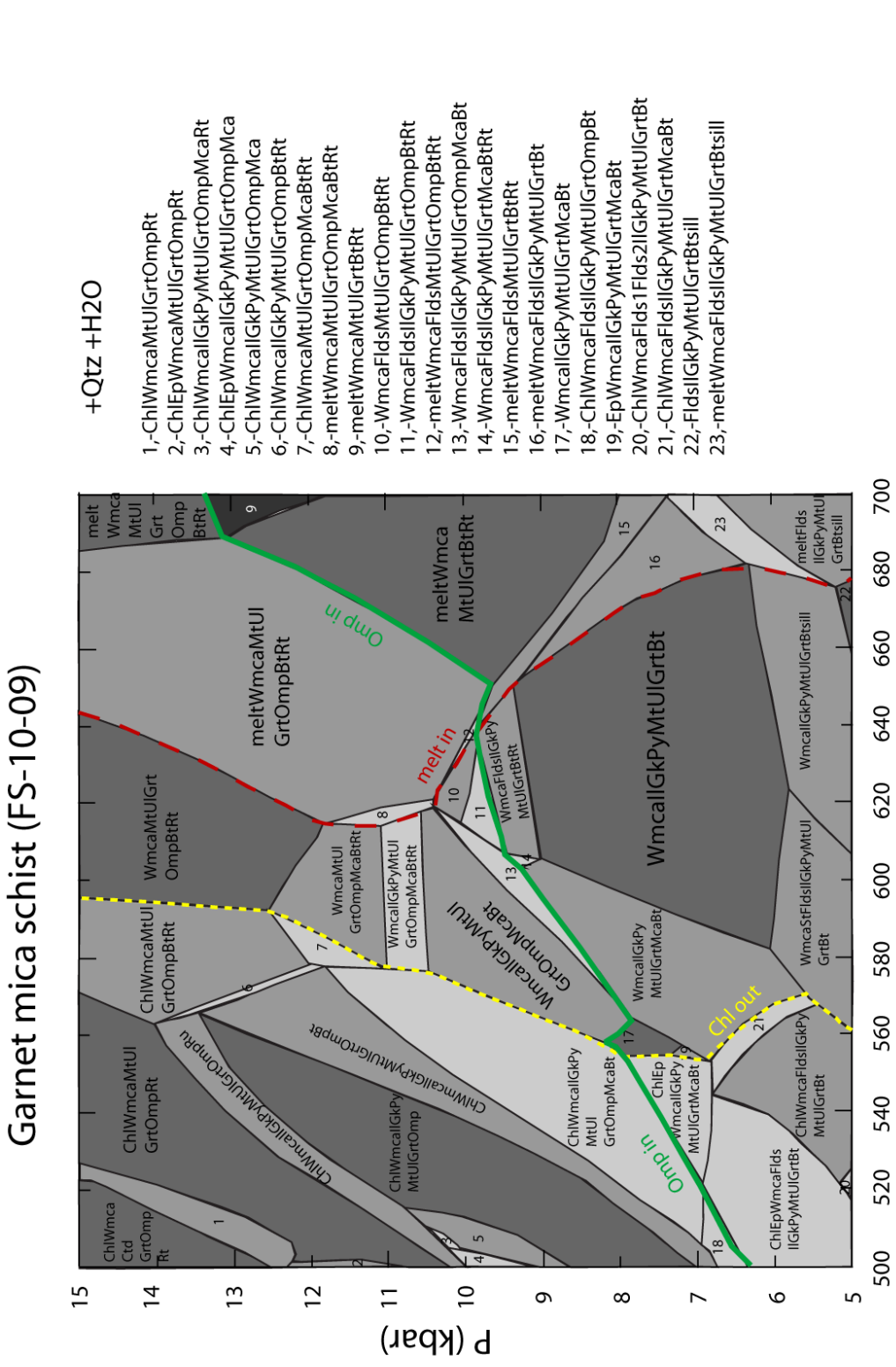

Figure 6.2: Pseudosection for sample FS-10-09: Garnet mica schist. Grey intensity in fields indicate degrees of freedom.

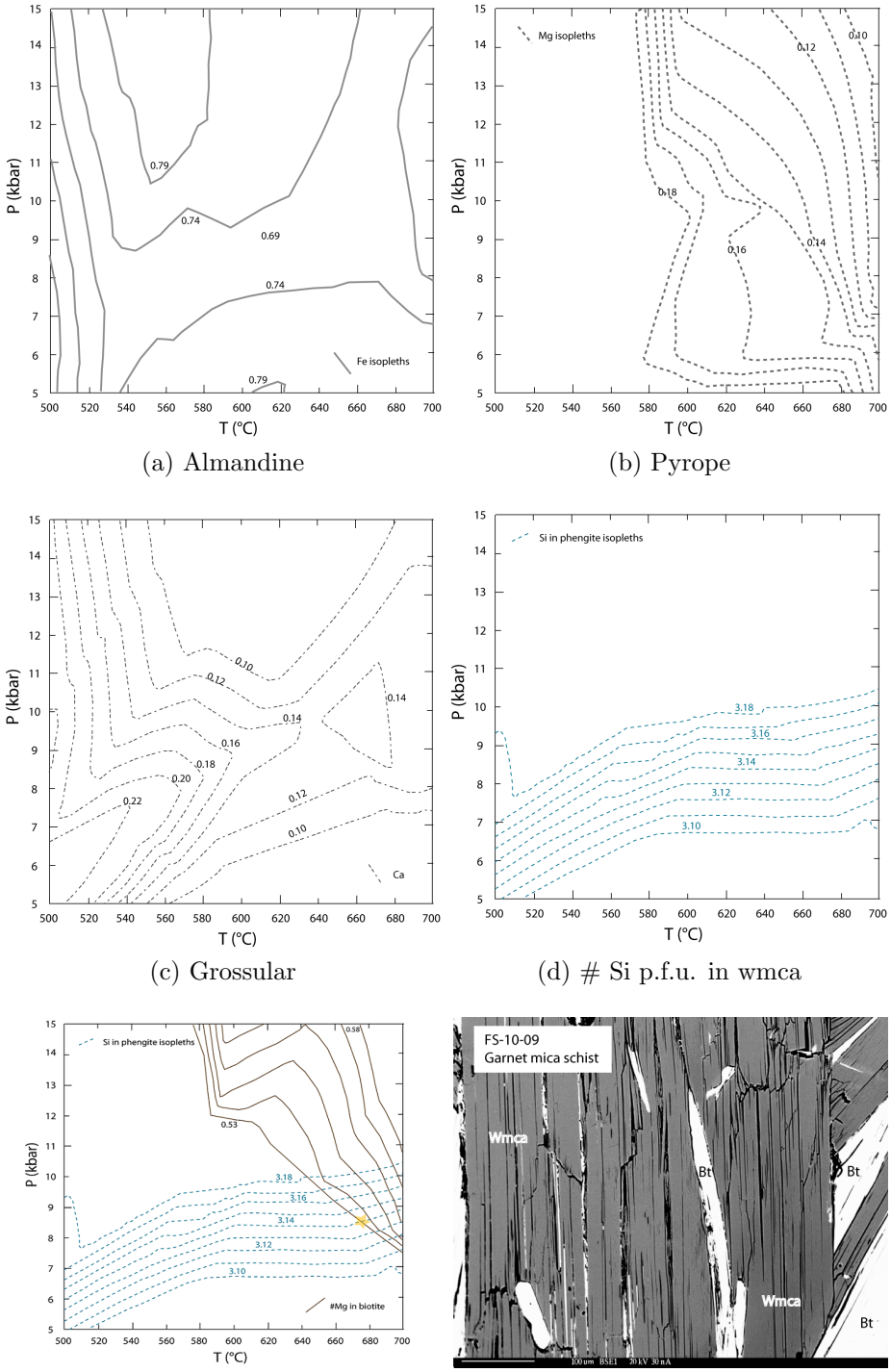

(a) Almandine (b) Pyrope

(c) Grossular (d) # Si p.f.u. in wmca

(e) Bt and wmca isopleths (f) BSE image micas

Figure 6.3: Isopleths of molar fractions of Fe, Mg and Ca in garnet, and content of Si p.f.u. in white mica, in garnet mica schist (FS-10-09). The yellow star shows the composition of white mica in equilibrium with biotite seen Figure 6.3f.

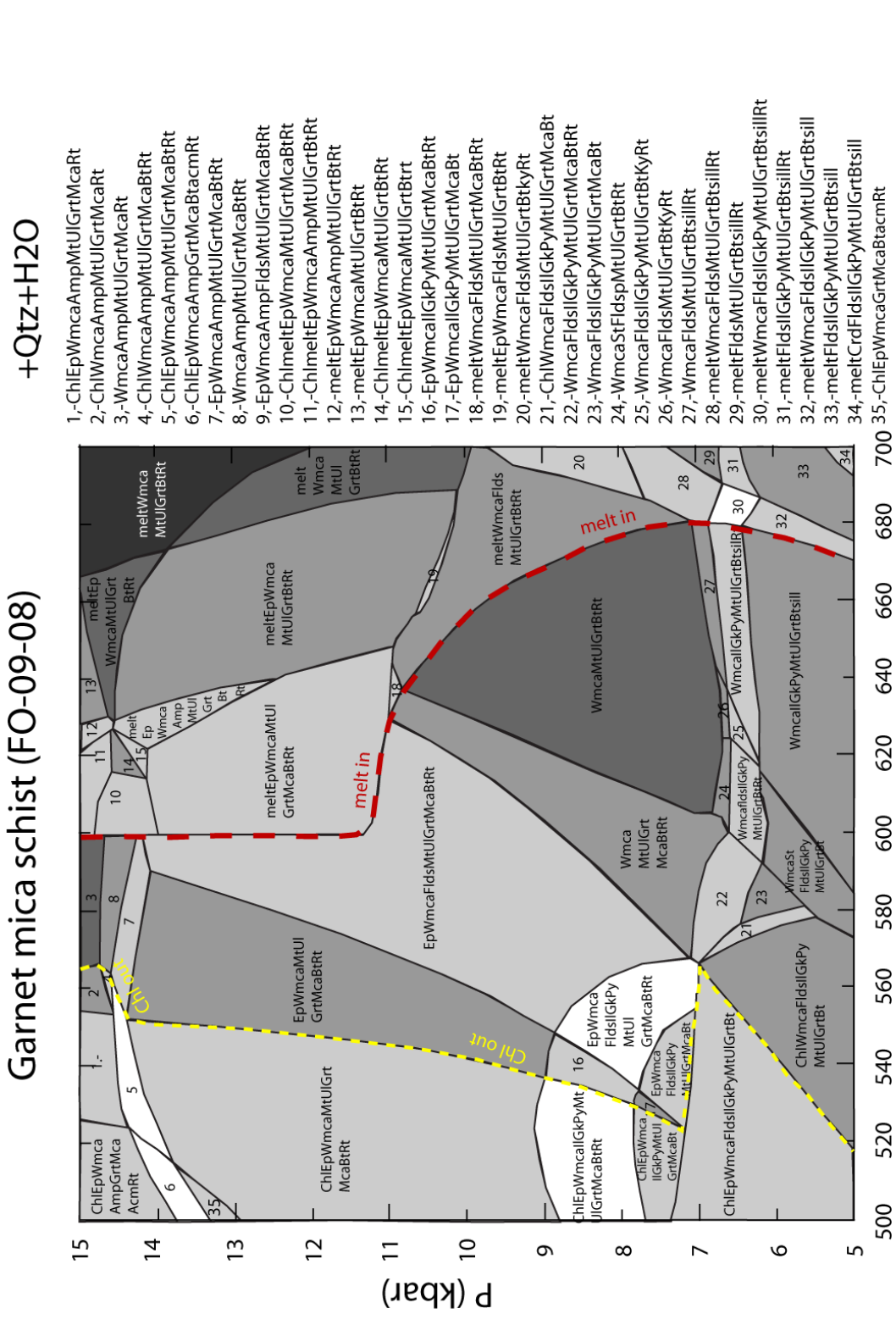

Figure 6.4: Pseudosection for sample FO-09-08: Garnet mica schist. Grey intensity in fields indicate degrees of freedom.

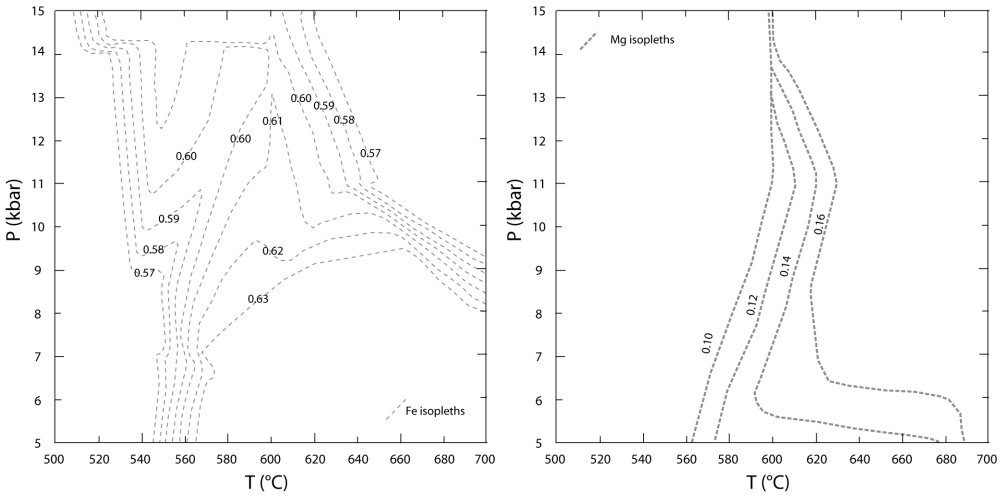

(a) Fe

(b) Mg

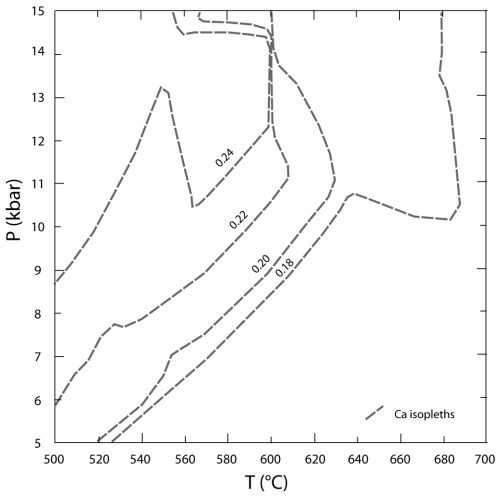

(c) Ca

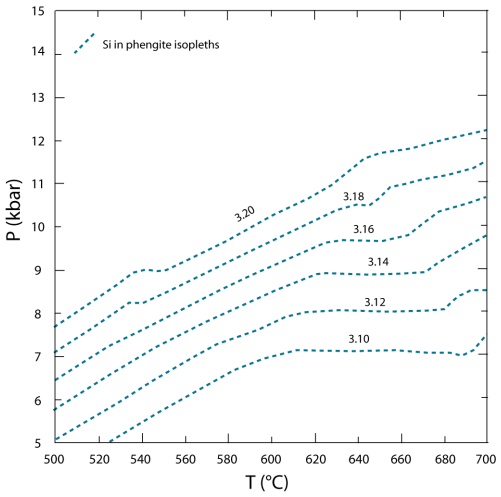

(d) Si

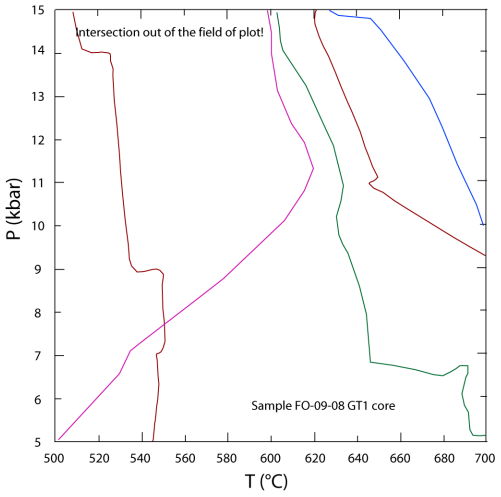

(e) Grt 1 Core

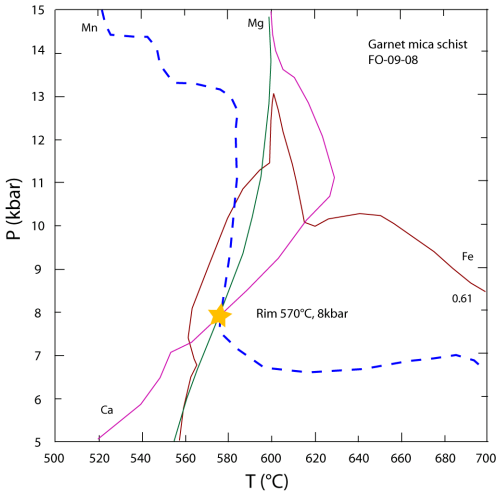

(f) Grt 1 Rim

Figure 6.5: Isopleths of molar fractions of Fe, Mg and Ca in garnet, and content of Si p.f.u. in white mica, in garnet mica schist (FO-09-08). Isopleth intersection between at core and rim of Garnet 1 from the same sample.

6.3.2 Garnet-biotite amphibolite

Samples FS-10-16C and FO-09-07 correspond to garnet bearing amphibolites containing a large percentage of zoisite, mineral whose occurrence indicates high oxygen fugacity, aspect which is considered in the parameters of the creation of the pseudosection.

These amphibolites were considered for analysis because they contain garnets (making up to 15% in some cases) as it was difficult to find garnets in the other amphibolite samples. The paragenesis of this sample consists of $Grt+Hbl+Bt+Wmca+Zo+Qtz\pm Ilm\pm Pl\pm Ttn$ and has retrograde chlorite in the edges of most ferromagnesian minerals. The pseudosections are seen in Figures 6.6 and 6.7.

The phase *melt* was excluded from the calculations, assuming that these are metabasites, their melting temperatures would be at much higher temperatures than the calculated ranges as seen in Figure 6.1. Instead, the hydrous mineral phase that dissappears as temperarure increases is *chlorite* around 650^oC in both amphibolite samples (Figs. 6.6 and 6.7.

It is worth to mention that *feldspars* do dissappear from the pseudosections as pressure surpasses the 7-8 kbars, and that *omphacite* is a phase that is present in most fields between the PT range plotted but in quantities as low as 0.5%. Petrography of these samples indicate that there is no visible pyroxene: considering that the pseudosection predicts less than 1% in most fields, it may be just a thing of luck not finding pyroxenes in the thin section.

Brunstmann et al (2000), mention in their work about zoisite and clinozoisite segregation in metabasites that during alpine exhumation, omphacite was pseudomorphosed to amphibole, albite, quartz and clinozoisite, case that could be applied to this sample. Massonne (2012) mentioned in his work that often omphacite is replaced by symplectites of plagioclase and amphibole.

In these thin sections, garnet appears in equilibrium contact with biotite, white mica and amphibole in both samples; these also have quartz, graphite and white mica inclusions, inclusions whose number of Si atoms p.f.u. were used for the construction of isopleths in sample FS-10-16C. On the other hand, $\#Mg$ in biotite did not vary, hence there was only one isopleth for that mineral phase at $\#Mg = 0.62$.

Garnet component isopleths in Figure 6.8 present diverse but complementary patterns from sample FS-10-16C. Mg isopleths show a very constrained temperature range, showing prograde zoning, similar to Ca. On the other hand, Fe represents a larger range of pressure,

but constraints from a minimum pressure of formation of these garnets (line of garnet-in).

The isopleth components corresponding to core and rim were plot in each case for both amphibolites (results seen in Fig. 6.9). In sample FS-10-16C, the Ca, Fe and Mg components from garnet GT2 were intersected, where core and rim constrain a temperature and pressure of formation. Besides, in this sample, most garnets are in paragenesis with biotite thus the rim intersection was crossed by the $\#Mg$ in biotite obtained earlier, which confirms that these two phases are in equilibrium.

The same procedure was done for garnet Gt1 from sample FO-09-07 (Figs. 6.9c and d) where; the core does not present a clear intersection but a range instead, on the contrary, the rim presents a clear intersection at 590^oC and 7 kbar.

Table 6.4: Isopleths values for samples FS-10-16C and FO-09-07 for the phases garnet, phengite and biotite

		FS-10-16C		FO-09-07	
Phase	Component	Min.	Max	Min	Max
Garnet	Grossular	0.20	0.286	0.20	0.24
	Pyrope	0.08	0.175	0.13	0.16
	Almandine	0.53	0.617	0.57	0.60
Phengite	# Si p.f.u.	3.119	3.227	-	
Biotite	# Mg	0.62		-	

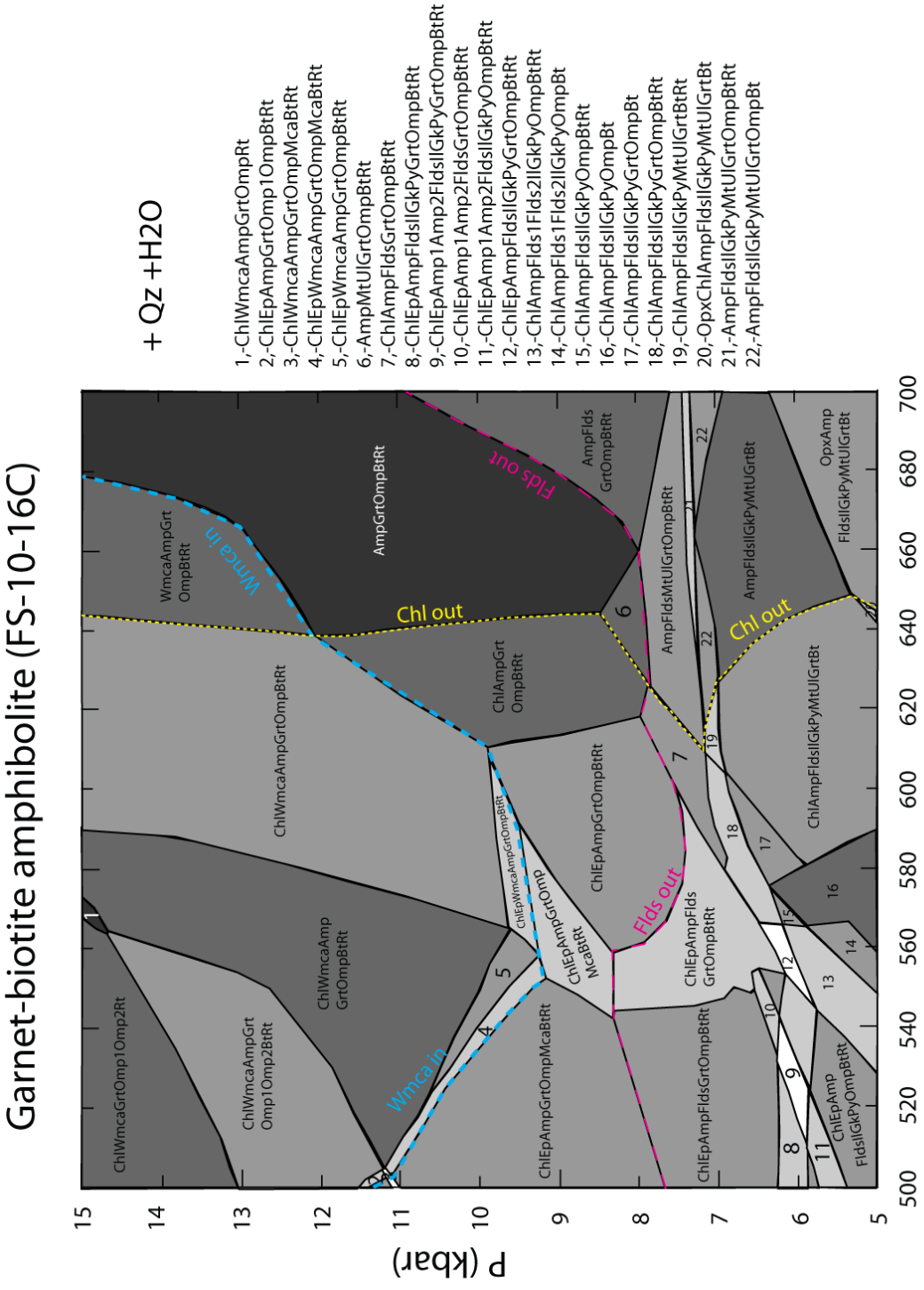

Figure 6.6: Pseudosection for sample FS-10-16C: Garnet-biotite amphibolite. Grey intensity in fields indicate degrees of freedom.

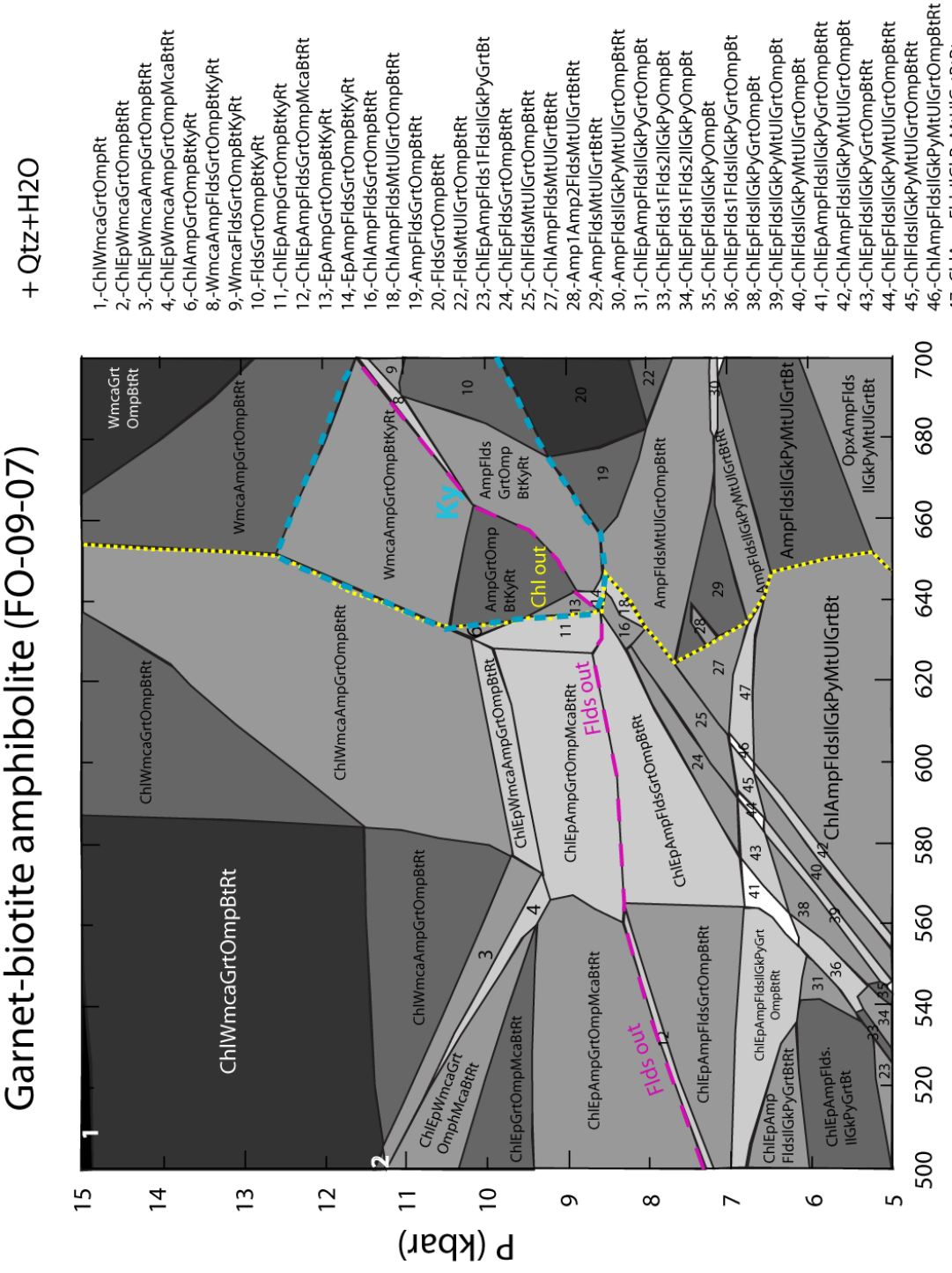

Figure 6.7: Pseudosection for sample FO-09-07: Garnet-biotite amphibolite. Grey intensity in fields indicate degrees of freedom.

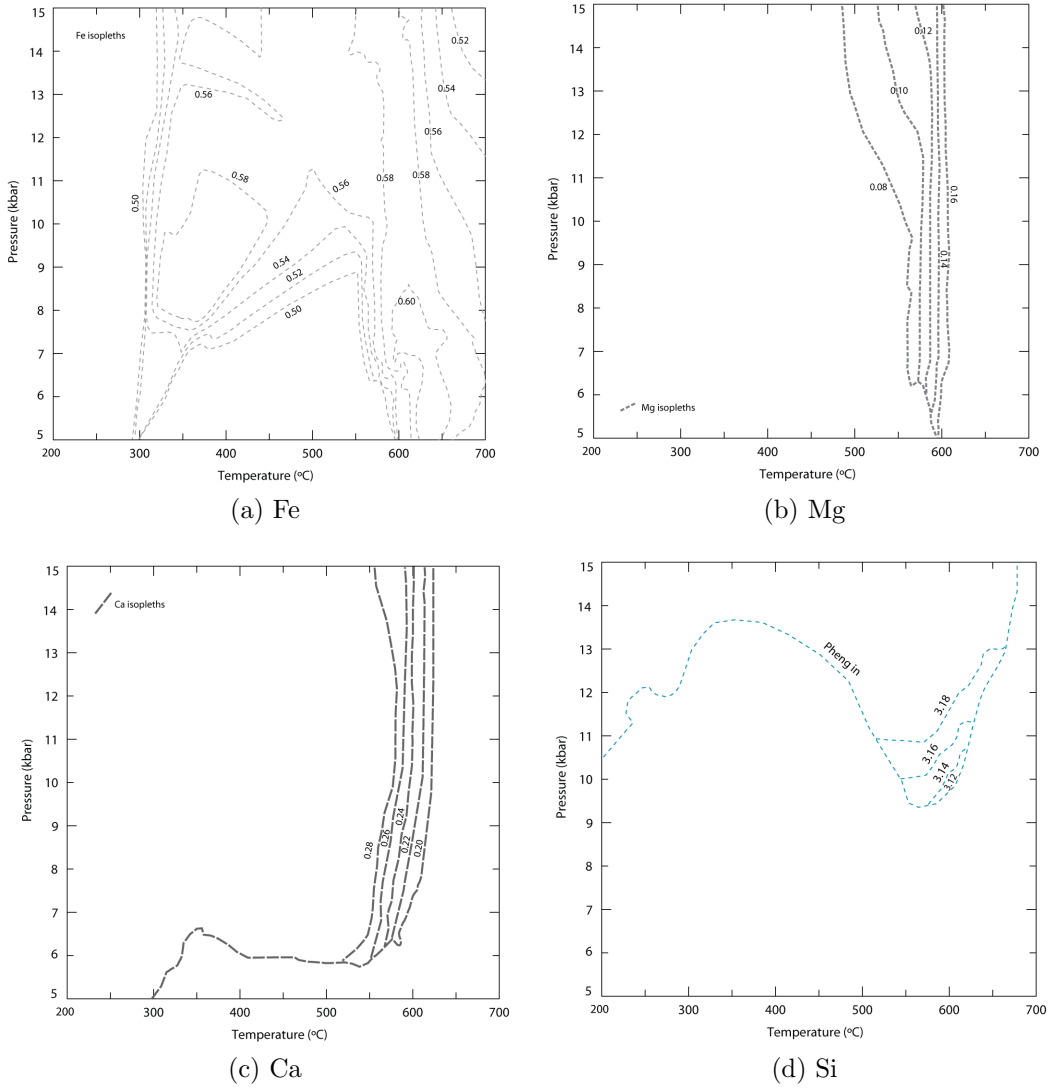

(a) Fe (b) Mg

(c) Ca (d) Si

Figure 6.8: Isopleths of molar fractions of Fe, Mg and Ca in garnet, and content of Si p.f.u. in white mica, in garnet amphibolite (FS-10-16C).

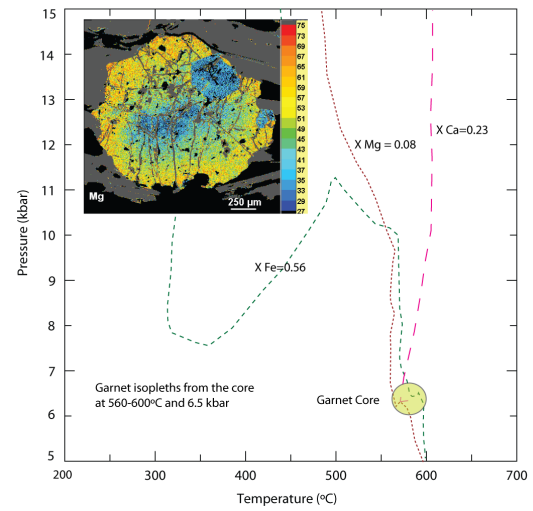

(a) Grt core FS-10-16C

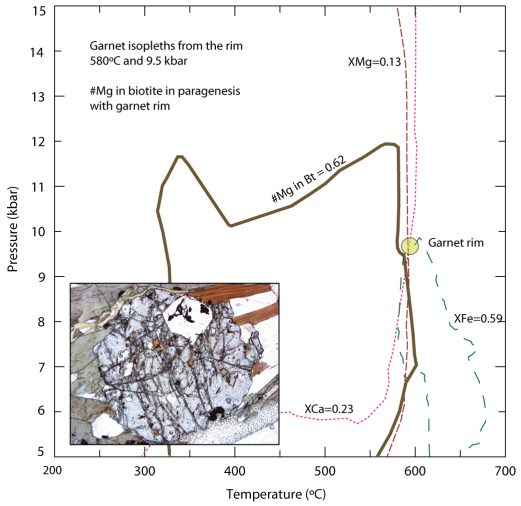

(b) Grt rim FS-10-16C

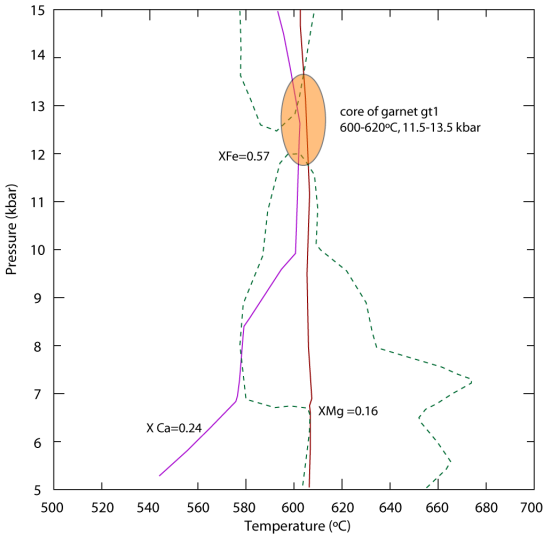

(c) Grt FO-09-07

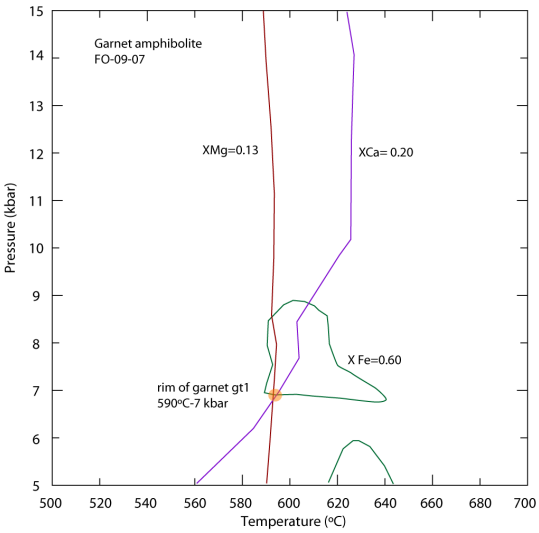

(d) Grt rim FO-09-07

Figure 6.9: Core and rim garnet isopleth intersections. In figure 6.9b the garnet isopleths were intersected with the biotite Mg

Chapter 7

Discussion

7.1 Protolith

7.1.1 Protolith of the mica schist

The protolith of the mica schist was determined to be sedimentary, with a composition similar to that of a greywacke (Ch. 4). The strongest evidence is the spread in ages of igneous detrital zircons, which can be interpreted as that the protolith was sedimentary. The same zircon grains present a metamorphic rim at ca. 280 Ma. with similar characteristics (Ch. 5).

The cores of zircon graines present ages with a large scatter, from where it is obtained that their REE patterns are also quite varied (REE data as part of the Appendix). If the cores of zircon had the same genesis, these would present similar ages and REE patterns. There is no similarity in ages, neither in their REE patterns, suggesting that the sources of zircon were different.

Similarly, there is no clear age of sedimentation seen in detrital zircon: it can only be obtained that the youngest age of deposition is ca. 304 ± 5 Ma in sample FO-09-13. The youngest crystallization age in magmatic zircon from the surrounding area is $288 \pm 2Ma$ from a granitoid from the Limón Verde Igneous Complex (LVIC). Also, the age from an extrusive body south of the Limón Verde Metamorphic Complex is $299 \pm 5Ma$. This extrusive unit corresponds to the rhyolites from the Cas Formation (Morandé, J. 2013 *personal communication*) assigned to the upper Carboniferous.

The garnet mica schist sample has an ϵNd t_0 value of -9.91, indicating that this sample

comes from a strongly differentiated crust, moreover this is consistent with the hypothesis that the protolith for this sample is sedimentary and has suffered several epidodes of crustal recycling. Its $^{143}Nd/^{144}Nd$ ratio of 0.51213 is quite comparable to present day $^{143}Nd/^{144}Nd$ ratios of the Huasco beds, Huentelauquen Formation and El Tránsito Metamorphic Complex, which range between 0.512105 and 0.512342 (Bahlburg, et al, 2009).

This rock unit is likely to have been deposited either in a fore-arc basin, or in the trench as flysch sediments from the uplifting Gondwanide orogeny.

7.1.2 Protolith of amphibolite

The protolith of the amphibolite was found to be igneous through a geochemical discrimination based upon whole rock minor non-mobile element parameters (Ch. 4) X_1, X_2 and X_3 where they all turned out be positive indicating that its provenience from an igneous source (basalt).

On the other hand, the classification of basalts based upon a Pearce and Cann diagram denotes that most of samples fall on the within plate basalt field, and a lesser amount fall onto the low-K arc tholeiites. Trace element analyses indicate that the protolith of the amphibolite is both whithin-plate basalt (samples from this study and from Lucassen, et al. 1999) and low-K arc tholeiite (data from Baeza, L. 1984). These types of basalt can be found in an island arc setting or as a large igneous province setting in the continental crust.

The garnet amphibolite (FS-10-6C) has a $^{143}Nd/^{144}Nd$ ratio of *0.51246* , value comparable to continental flood basalts or subcontinental lithosphere. It also has an ϵNd t_0 value of -3.47 which is lower than expected for a basaltic protolith: this may indicate that even though the rock is a metabasite and should be somehow similar to a mantle source, it is highly differenciated inferring that the protolith is a within plate basalt with significal crustal contamination or several periods of recycling.

The tectonic setting during the sedimentation and accumulation of the protolith, corresponds to an active margin with convergence of oceanic crust depicted in a cartoon in Figure 7.1 where a combination of oblique convergence (probably coming from the NW) and anomalously shallow asthenosphere (Götze and Krause, 2002; Tomlinson et al., 2012) during the Late Caboniferous - Early Permian, may have contributed to the thinning of the continental crust creating a depocenter and a thin enough crust to allow the rise of mantle material.

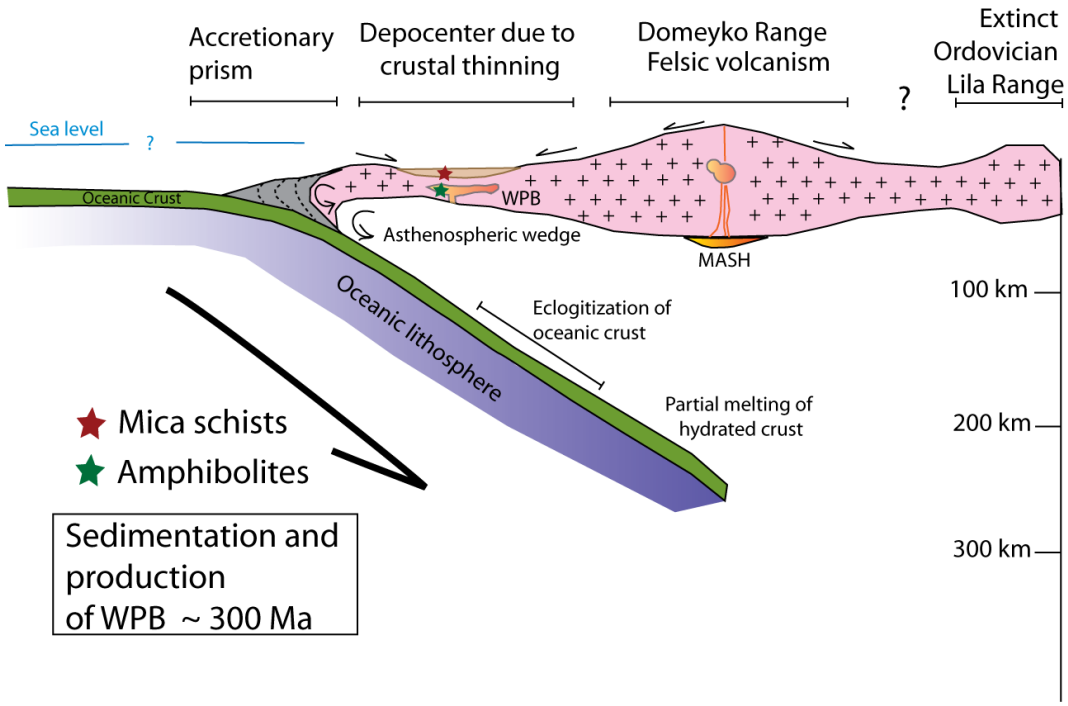

Figure 7.1: Active margin magmatism during the Carboniferous. Sedimentation and thinning of the forearc basin to allow within plate magmatism. WPB stands for *within plate basalts*.

An 'advancing subduction' is a plausible mechanism to shorten the forearc crust and to bring the sediments of the forearc basin into the trench and down the subduction channel. There are several parameters that can influence the advance of a subduction zone such as angle of the subducting slab, age of the subducting slab and subduction erosion (García, 2012). Table 7.1 shows a compilation of subduction erosion rates along the Chilean margin since the reactivation of subduction during the Jurassic at ca. 200 Ma (beginning of the Andean cycle (Charrier et al., 2007)).

Table 7.1: Subduction erosion rates along the Chilean margin. Modified from Kukowski and Oncken, *and references therein*, 2000.

Latitude (degrees S)	Time interval (Ma)	Subsidence rates (m/My)	Trench retreat (km/My)	Erosion rates (km3/Myr km
20	Since 8		1	37 - 40
22	Since 8			40 - 45
23.5	Since 20	200	1.25 - 1.75	45 - 50
21-26	Since 200		1.05 - 1.45	37 - 50
30	Since 15			84
33	Since 10	300 - 500	3 - 4	96- 428
36-40	11 - 3	200		25 - 35
47	4.2 - 1.5		8	231-443

7.2 Age of metamorphism

The multimethod approach used to determine the age of metamorphism in the mica schist and amphibolite of the LVMC consists of Sm-Nd dating in garnet-whole rock pairs for both rock types and U-Pb dating for zircon and titanite, for garnet mica schits and amphibolite respectively.

7.2.1 Age of metamorphism of the mica schist

From TIMS Sm-Nd whole rock-garnet dating, an isochron age of 380 ± 21 Ma, was obtained with an MSWD=2.0 for sample FS-10-09. On the other hand, U-Th-Pb SHRIMP ages obtained from two garnet mica schists (FO-09-08 and FO-09-13) show a large scatter in the dates obtained, from the Paleo-proterozoic to the Triassic (histograms from Fig. 5.2). This may be due to:

- the location of where the spot ages were taken in the crystal i.e. in some cases the center of a zircon will represent an age much older than its rim,
- the nature of the protolith: this has been an issue for a while since it was not known with certainty whether the protolith of the mica schist from the Limón Verde Metamorphic Complex (LVMC) is igneous or sedimentary.

For example: in Figure 7.2 there is a representative core and rim analysis of zircon #6 from sample FO-09-08 inset in the relative probability histogram versus age from the same sample. This zircon presents a core that may have crystallized at 682^oC (determined with the Ti thermometer) in an igneous event (seen by its concentric zoning and REE pattern) at 964 ± 10Ma during the Grenvillian orogen).

The rim of the same zircon has grown during metamorphism at 551^oC at 273 ± 5 Ma; its REE pattern shows a general depletion of REE consistent with metamorphic growth. Although, many other detrital zircons similar to the one presented in Fig. 7.2 show a widespread age spectra in their cores, it is seen that a large majority presents a metamorphic rim at ca. 280 Ma thus the age of metamorphism was calculated to be 281 ± 3 Ma in sample FO-09-08 and 278 ± 3 in sample FO-09-13.

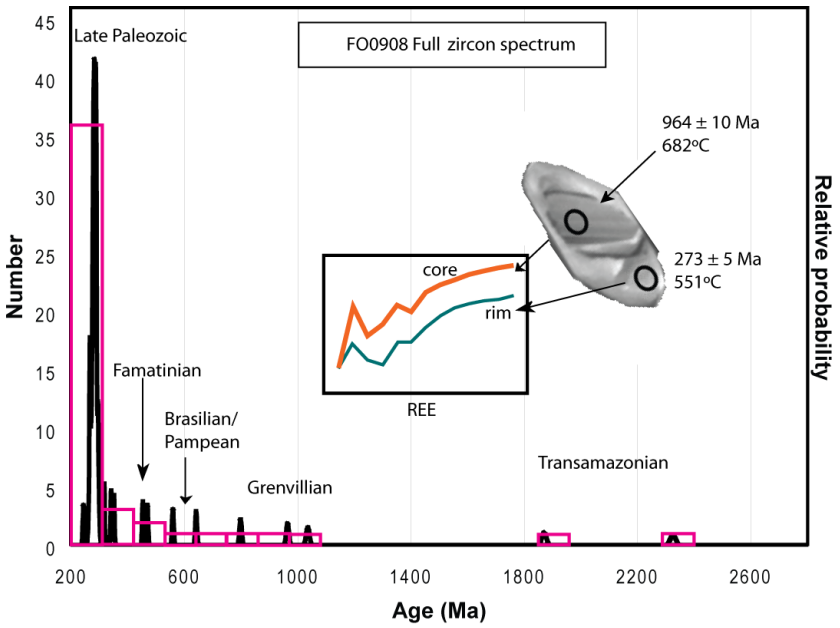

Figure 7.2: Representative zircon with inherited/igneous core and metamorphic rim from garnet mica schist sample (FO-09-08). Inset shows the difference in REE patterns.

The age ca. 380 Ma does not appear in the U-Pb in zircon age spectrum, thus there is no way to relate the age of metamorphism of garnet to a previous event, on top of that, the historical data of metamorphism favors the ca. 280 Ma age. Despite that the Sm-Nd isochron age show no concordance with U-Pb data of metamorphism in the mica schist samples, and are neither in agreement with Sm-Nd ages from Lucassen et al. (1999), they have similar Nd-depleted mantle model ages therefore they can be related to a similar crustal recycling process.

The ϵNd_{t1} of the mica schist (FS-10-09) at $t_1 = 280$Ma, is *-7.16*. This value is barely comparable to the ones obtained in the literature seen in the time versus ϵNd_t Figure 7.3 (Bahlburg, et al. 2009, *and references therein*). The values that are comparable are the ones from Huasco beds and Las Tórtolas Formation, but these correspond to age of deposition instead of metamorphism. There is more information needed to discuss this data.

7.2.2 Age of metamorphism of the amphibolite

The Sm-Nd whole rock-garnet isochron age of a garnet amphibolite (FS-10-16C) is 375 ± 13 Ma, with an MSWD of 0.86. Althought the MSWD of this age is low and may indicate a plausible age of metamorphism, it is at least 100 My off from the ages of metamorphism

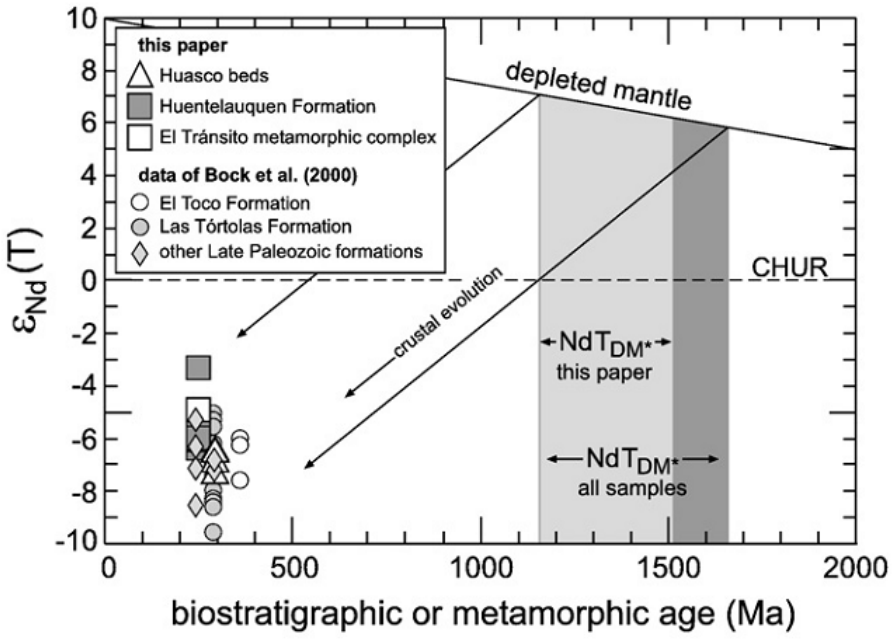

Figure 7.3: Time versus $\epsilon Nd_t diagram$. CHUR: Chondritic uniform reservoir. Epsilon Nd values were calculated to the time of deposition or metamorphism. Figure from Bahlburg, et al. 2009.

(also in amphibolite) obtained by Lucassen et al. (1999). These ages are 268 ± 19 Ma for a garnet-zoisite amphibolite and 271 ± 9 Ma in an amphibolite.

Because of the large disagreement in the above mentioned ages, a second method was used to date the metamorphism of amphibolites: this was U-Pb dating of metamorphic titanite from sample FS-10-02 by SHRIMP II. Where it was found that the likely crystallization date for the titanite is Triassic ca. 243 ± 26 Ma, generally in accord with the zircon data for FO-09-08 and FO-09-13. Despite the large error in the calculated age, the MSWD is only 0.66, proposing that the age of metamorphism is reliable.

Recall that the blocking temperature of the Sm-Nd system in whole rock-garnet pairs is ca. 600 ^{o}C, and that the blocking temperature in U-Pb in titanite is ca. 625 ^{o}C (Dickin, 2005). Then the ages of metamorphism should also be similar. Again, the ca. 380 Ma of metamorphism of the amphibolite is not favored here, but the age of 243 ± 26 Ma is preferred.

Finally, the Ar-Ar age in hornblende from the same amphibolite of 264 ± 1.2 is concordant with the age of metamorphism of U-Pb in titanite inferring that the age of metamorphism of the amphibolite unit is ca. 260 Ma. This will be further discussed in section 7.4.

7.3 PTX conditions of metamorphism

7.3.1 Grt-mica schist

The $Perple_{\chi}$ and classic geothermobarometry results from 2 samples (FS-10-09 and FO-09-08) were used to build the *pressure-temperature* path of the garnet mica schist unit. Isopleth intersection in the core and rims of garnet from sample FS-10-09 was not achieved i.e. the garnet component isopleths did not intersect in a single point (Fig. 6.3a-c), these point to a PT area of intersection. Nevertheless the Ferry & Spear Grt-Bt thermometer gives temperatures concordant with the isopleths intersection of biotite and white mica (Fig. 6.3d-f). Since these phyllosilicates are late phases and are in paragenesis with the rim of garnets, then they are associated to later stages of metamorphism. Sample FO-09-08, showed better garnet component isopleth intersection, were core and rim could easily be defined (shown in Figures 6.5e-f and blah from the appendix); also, this sample has two visible generation of garnets, where the smallest-second-generation can be related to the same stage of metamorphism as the rim from the larger garnets.

Garnets from the *garnet mica schist* samples present the strongest zoning patterns in their grossular component. Large deformed poikilitic garnets (around 1 mm in size) have cores enriched in Fe and Ca, and depletion of these elements towards the edges, only to be replaced by Mg. Small equant fresh garnets (around 400 μm in size) present a minor enrichment in Ca towards the rim, and depletion of Mn and Mg in the same direction (Figs. 4.3a and 4.4b. Another source of Ca in these samples are the many Ca-bearing phases enclosed in the garnet structure (apatite and titanite) and also as accessory minerals which may account for the free Ca in the matrix.

For a geodynamic interpretation, this is interpreted as a decrease in pressure and an increase in temperature during the growth of larger garnets, and an increase in pressure and decrease in temperature for the smaller garnets. A first order interpretation consists of a prograde path followed by a retrograde-high pressure path, or that, as seen in the rims from garnet in Figure 4.4b, this feature might also be a re-equilibration of Ca with the surrounding minerals from the matrix.

Only micas from garnet mica schist samples were imaged with X-rays (samples FS-10-09 and FO-09-08). Phengites shown zoning in Ti and Mg, with an enrichment towards the center

of the crystals. This zoning is not concentric, rather tabular, moreover it does not follow the alignment of the mica laths (Fig. B.4 from the Appendix). On the other hand, the zoning in Si shows a depletion towards the edges indicating a drop in pressure (Massonne, 2012; Powell and Holland. 2010; Spear, 1993). Considering these two characteristics of the phengite laths, it is likely that the center of the crystals formed under a set of PT and differencial stress different than the one seen in the rest of the sample denoting the occurrence of two episodes of strain with dynamic recrystallization.

There is no zoning in biotite. There is only minor chloritization in some edges or fractures in biotite laths.

Recent Zr-partition modeling studies (Corrie et al, 2012) suggest that there is a negative proxy for the growth of zircon in metamorphic environments above $ca.550^oC$ during prograde metamorphism, because the formation of omphacite and garnet (mostly Ca-rich garnet) incorporate increasingly higher concentrations of Zr causing zircon to dissolve. On the contrary, zircon is predicted to grow mainly on the cooling path, particularly during the crystallization of melt.

It is mentioned earlier that the large garnets from mica schists are broken down and present retrograde metamorphism (seen as chloritization). On top of that, both pseudosections created to similar garnet-mica schist samples show a melt curve appearing at fairly low temperatures (ca. 600^oC) indicating anatexis and migmatization in the samples. Therefore, it is plausible that the enrichment of REE can be due to garnet dissolution during retrograde metamorphism.

In the same figure, it is seen a small negative Nd anomaly (Fig. 5.4) that can be attributed to the same process. In the case that garnet may have liberated REE during retrograde metamorphism except for Nd may account for an excess of the element in garnet. Thus, it is very likely that the excess of Nd in garnet makes its Sm/Nd isochrons steeper hence giving ages much older than what they should represent.

A summary diagram for the garnet-mica schist is seen in Figure 7.4, where the orange stars represent core and rim values from sample FO-09-08 embedded in the PT field obtained by biotite-white mica interception from sample FS-10-09. Although the metamorphic path to get to the metamorphic peak is not known, it is calculated considering the PT data of core from garnet GT2 (600^oC and $14.6kbar$) which gives a geothermal gradient of $12^oC/km$.

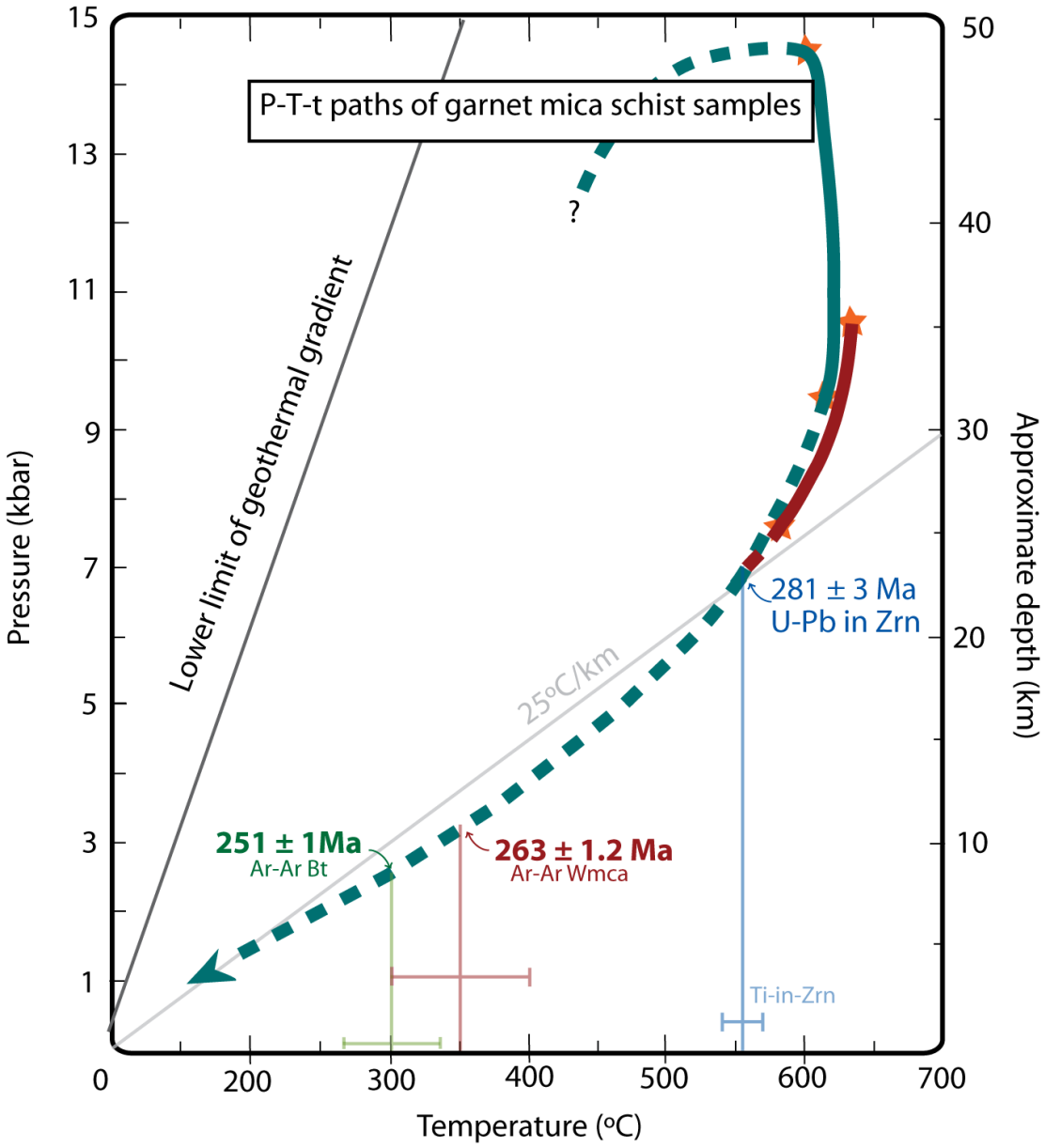

Figure 7.4: Pressure-Temperature-time path for garnet mica schist samples. Solid lines correspond to data obtained in perplex, dashed lines are inferred data. The orange stars represent the core and rim crystallization PT onset for garnets GT2 and GT3 from FO-09-08 embedded in the PT field from FS-10-09. Ar-Ar thermochronometers and their respective errors are lines intersecting the inferred retrograde path: Wmca in red and Bt in green. Ti in Zrn thermometer and error in blue.

The cold $12^oC/km$ geothermal gradient, is placed in the onset of subduction: particularly down the subduction channel where pelagic sediments contribute with fluids that lower the temperature (Ernst, 2005; Ernst,et al. 2009; Massonne, 2012). The 14.6 kbar can also be correlated to a depth of ca. 50 km, followed by a nearly isothermal decompression of ca. 20 km (increase of temperature of less than 50^oC). This is called exhumation with thermal relaxation (Peacock, 1989). After this point, there is no more geothermobarometry data, since the paragenesis of the sample records only the metamorphic peak with little retrograde metamorphism.

The retrograde path is inferred from a normal crust geothermal gradient of $25^oC/km$ (Ernst, 2009) with results to be shown in the section 7.4

7.3.2 Amphibolite

The building of a *pressure-temperature* path for the garnet amphibolite unit was also based upon classic geothermobarometry and forward modeling data from two samples: FS-10-16C and FO-09-07. The data from the Ferry & Spear Grt-Bt thermometer in sample FS-10-16C presents a core temperature much lower than the one obtained through garnet component isopleth intersection from both samples, the same happens with the data from the rim.

Although the amphiboles present in the analysed samples belong to the *Ca-hornblendes* (Deer at al, 1992; Hawthorne and Oberti, 2007), they tend to incorporate Na in their structure. This has been used in the past as a geobarometer, and finding Na-amphiboles in a sample is indicative of high pressure conditions of metamorphism (Deer, at al. 1992). It is likely that the incorporation of Na into the ferromagnesian amphibole structure indicates a high pressure environment of formation, in the upper amphibolite facies. It is seen in Figure 7.5 that the hornblende stability field for metabasites with Mid Ocean Ridge Basalt (MORB) composition, reaches higher temperatures and higher pressures than described in earlier literature. Although the amphibolite samples from this study do not have a MORB whole rock composition, the diagram is a good approximation for classification of the samples in this study: sample FS-10-16C falls in the *Grt-amphibolite* field and sample FO-09-07 fall in the *Hbl-eclogite*.

There is a large presence (up to 25%) of clinozoisite in the amphibolite samples, initially this was interpreted as that the rocks formed in conditions of high O_2 fugacity (Deer, et al.

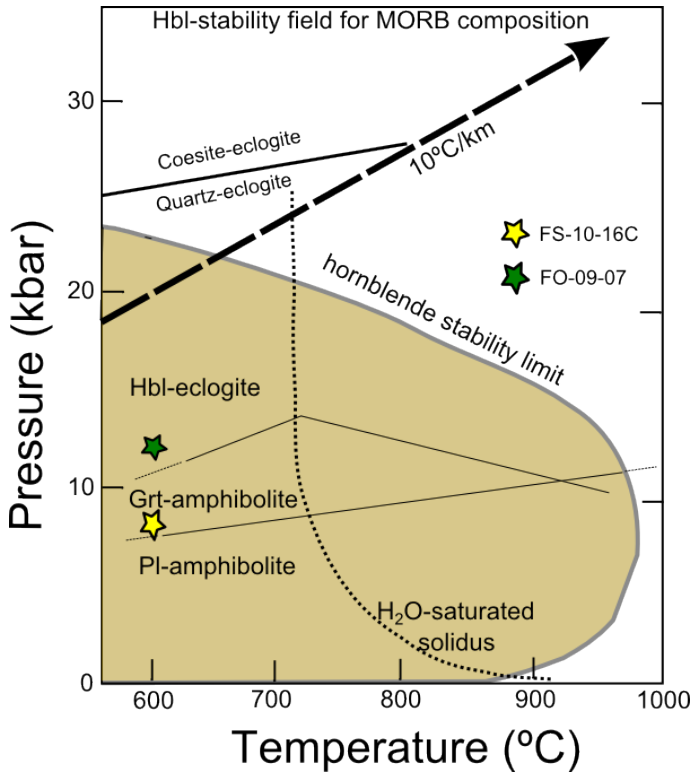

Figure 7.5: Hornblende (Ca-amphibole) stability diagram at medium to high temperatures for metabasites with MORB-like composition based on Ernst, 2009. The garnet-amphibolite samples from this study are shown as stars.

1992). Recent studies by Massonne (2012) in amphibolites and eclogites, show that the formation of clinozoisite-epidote at high pressures is due to fluid infiltration during exhumation. Since there is no direct way to quantify the amount of fluid at the pressures found (amount of water and carbon dioxide are independent variables in pseudosection calculations), a probable solution is that both parameters (fluid and oxygen) favored the formation of clinozoisite.

It turns out that oxygen is a major controller of the mineral paragenesis in each pseudosection. When modeling with different amounts of water and oxygen, there were major changes in the pseudosections (always considering the whole rock composition to remain constant). Oxygen in whole rock composition was calculated on the assumption that ca. 0.1% of the total Fe of a sample is *ferric*. For example: the garnet amphibolite sample FS-10-16C was calculated with $0.118\%O_2$ and sample FO-09-07 was calculated with $0.113\%O_2$. The set up of oxygen values, has a major chage in the almandine component of garnet.

One garnet-amphibolite sample (FS-10-16C) has one poikilitic garnet (Gt2) with white mica inclusions, in addition there are graphite inclusions in one of the crystals (Fig. 4.13). The growth of these crystals is layed out in Figure 7.6, where the composition of the center of

the garnet can be correlated with the composition of the center of the mica inclusion. These textural relationships were taken into account for the construction of isopleths, nevertheless, composition of the white mica does not fit the modeled pseudosection, then it is inferred that it is not in equilibrium with the bulk composition of the sample.

On the other hand, usually the appearance of graphite in metamorphic assemblages is an indication of protolith: carbon is often associated with organic material in a sedimentary environment. This rock is an amphibolite with an igneous protolith, which makes it unlikely for the graphite to come from an organic source but more of a devolatilization associated with prograde metamorphism (Winkler, H. 1979).

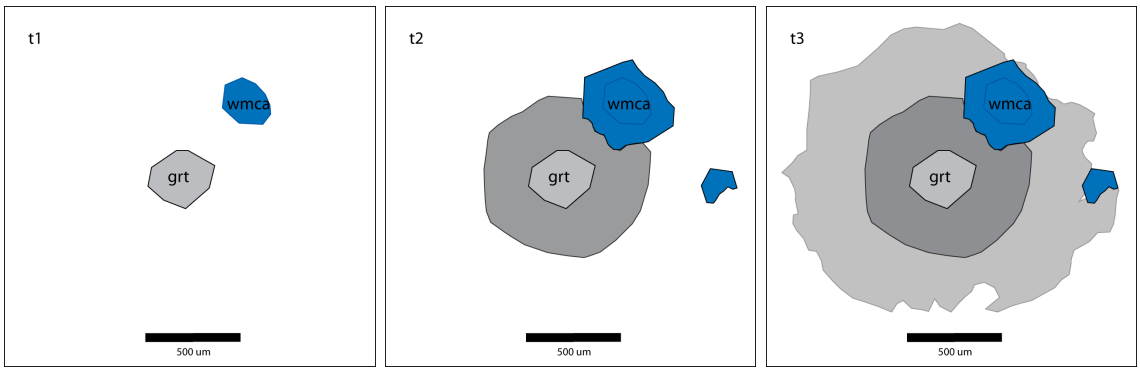

(a) t1 (b) t2 (c) t3

Figure 7.6: Interpretation of mineral growth in a poikiloblastic garnet (Fig. 4.13) with phengite inclusions from a garnet amphibolite (FS-10-16C). Grey colors indicate concentric zoning episodes.

In the *garnet amphibolite* samples, both large and small garnets are poikilitic and highly fractured. Fe content looks constant across the garnet, whereas Ca and Mn present minor variation. Ca looks constant to slightly enriched towards the rim, same as Mn. Which is interpreted as an increase in pressure and temperature on a prograde path. Both samples present different core-to-rim paths: FS-10-16C is anti-clockwise and FO-09-07 is clockwise as seen in Figure 7.7. The PT path was determined through garnet component isopleth intersection for garnet GT2 in sample FS-10-16C (Figs. 6.9a and b), where its core may have formed at a depth of ca. 21 km and bury isothermally to a depth of ca. 32 km. On the other hand, the garnets GT1 and GT3 analysed in sample FO-09-07, show intersections of $600-620^oC$ and $11.5-13.5kbar$(equivalent to for their cores, and 590^oC and $7kbar$ for their rim, equivalent to a exhumation or nearly 15 km. The PT paths are plot on Figure 7.7.

These rocks do not contain any retrograde metamorphic minerals, then the lack of a retrograde path leads to the vague assumption that they exhumed together. As mentioned earlier in the thermochronometry section, the age data for the amphibolite unit is confusing: error and closure temperatures overlap, lacking of a cooling history path. At the end, in the amphibolite unit it can only be obtained a PT field of peak metamorphism and be related to the ages with a large scatter thus an upper age of metamorphism of ca. 269 Ma.

7.3.3 Summary

The prograde metamorphic paths proved to be different for the different rock units. A rough approximation summary indicates that the general metamorphic path of the LVMC consists of a clockwise prograde trayectory. The first stage involves burial for all rocks to different depths, but with a similar geothermal gradient (12 and 15 $^oC/km$). With this, it is assumed that there is significant thickening of the crust then because thermal relaxation (heating) and erosion (decompression) of thickened continental crust take place simultaneously, the pressure during peak metamorphism is significantly less than the maximum pressure experienced by a metamorphic rock (Peacock, 1989) as seen in both rock units from the LVMC.

The PT information obtained from cores of garnet in amphibolite and mica schist provides the initial setting of metamorphism. A geotherm of $12^oC/km$ for the mica schist and a geotherm of $15^oC/km$ for the amphibolite sample are necessary to reach the PT of initial crystallization or garnets (recorded in cores). These geotherms are cool ones and regularly obtained in a subduction tectonic setting; particularly in the subduction channel (Willner et al., 2004; Massonne, H. 2012).

Although the magmatic arc is supossed to be active during this period, there is no evidence of magmatism or a magmatic arc in this area at ca. 280 Ma. (Mpodozis, 2013, *personal comm.*), but there is evidence of anatexis and fluid remobilization seen in the field and in thin section, in the mica schist unit (eg. Fig. 3.2) and also as quartz veinlets in the amphibolite sample.

It is pressumed that subduction was taking place at this time, in the meantime, a small terrane and/or volcanic island was approaching to the craton on top of the subducting oceanic crust. It is noted that peak metamorphism and thermal relaxation cooling started right after the 280 Ma for the mica schist at a depth of ca. 50 km. Instead, the amphibolite has a peak

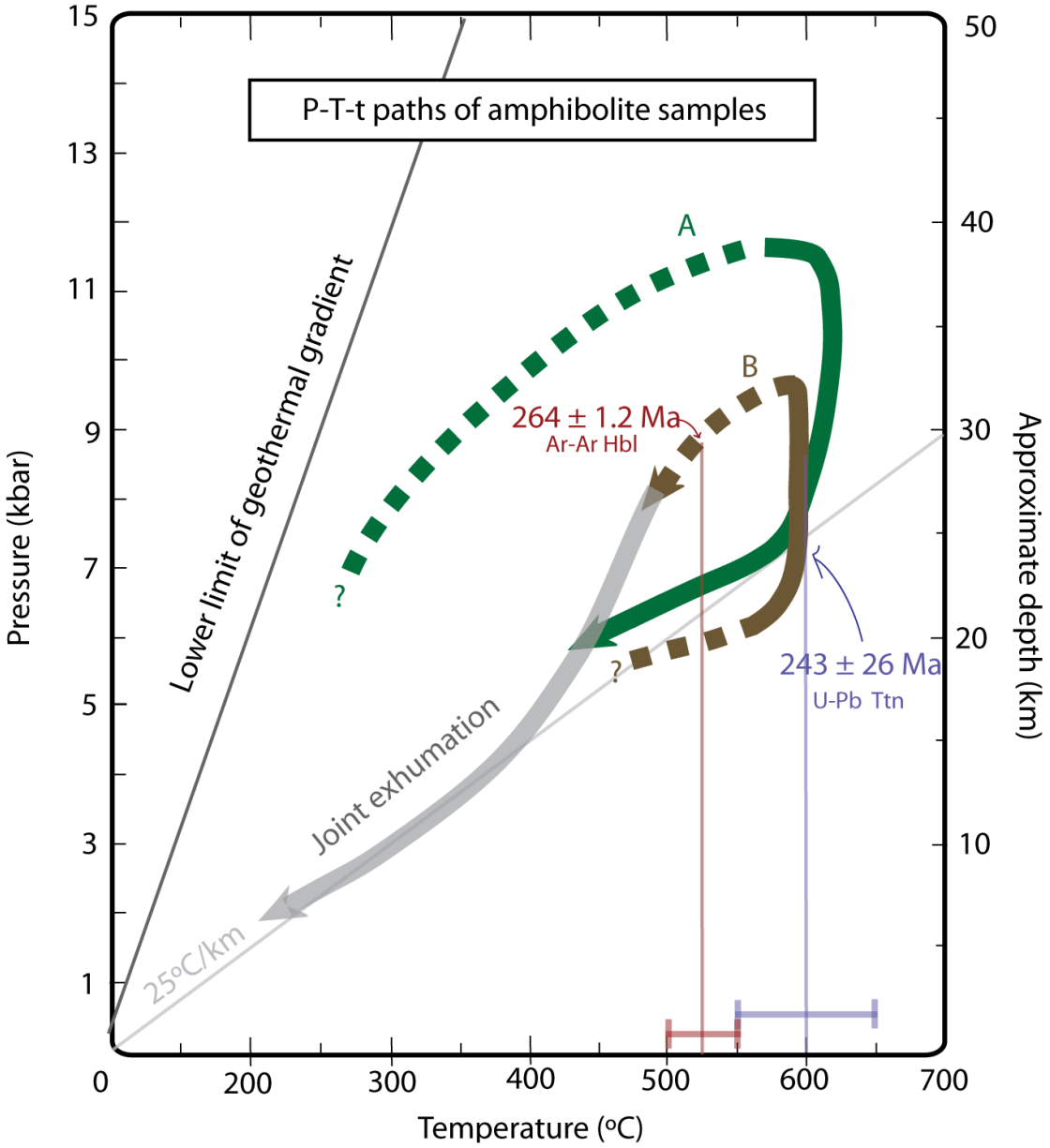

Figure 7.7: Pressure-Temperature-time path for amphibolite samples. Solid lines consist of data obtained through pseudosection and core to rim calculations. Dashed lines correspond to inferred data. A: Core-to-rim clockwise path in garnet GT1 from sample FO-09-07. B Core-to-rim anti-clockwise path in garnet GT2 from sample FS-10-16C. Closure temperature of the metamorphic minerals dated as shown as lines with their respective errors

.

metamorphism and cooling to start at ca. 260 Ma at a depth of ca. 40 km.

Then, the above mentioned rocks present a ca. 15 My difference between their metamorphic peaks, and at least 10 km of difference between their major depths of emplacement during metamorphism. Since they are not contemporaneous, these can not be assigned to the same period of metamorphism but perhaps to a genetic history similar in different times. What these rocks do have in common is the shape of their metamorphic path, encouraging a similar genetic history.

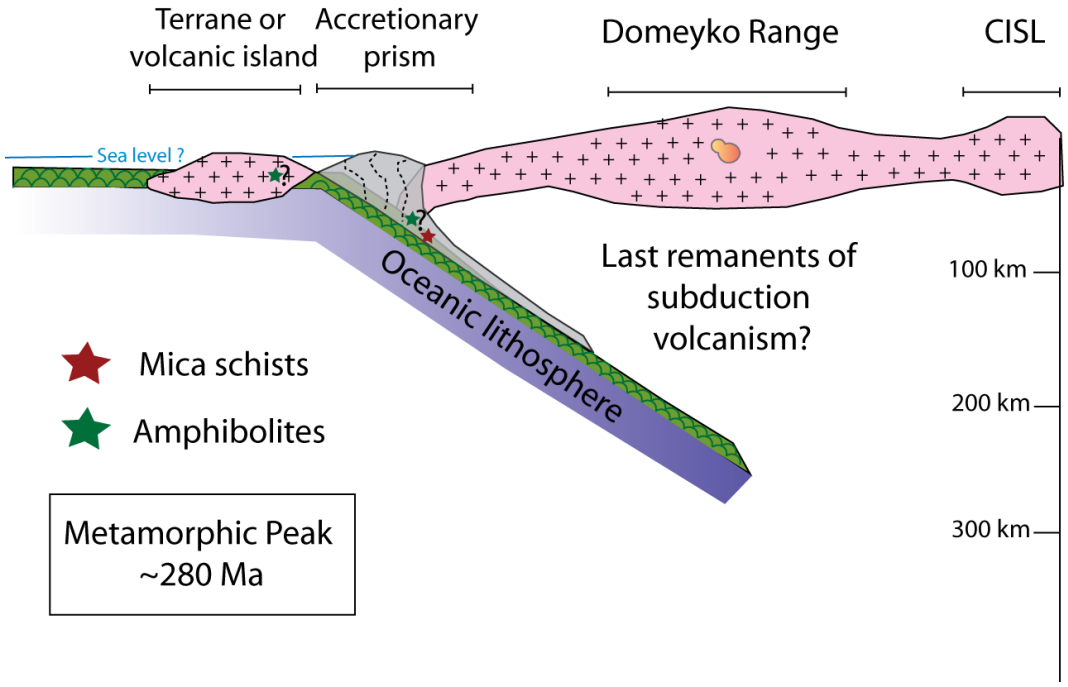

Figure 7.8: Active margin subduction during the mid-Permian. The metamorphic peak of the mica schist unit was reached at this point down the subduction channel. The metamorphic peak of the amphibolite units is at least 15 My younger than the one from the mica schist. It is also postulated in this image that the amphibolite can have a protolith either at the bottom of the fore-arc basin or in the volcanic island.

7.4 Exhumation and cooling history

It was found through pseudosection calculations that the mica schists never reached temperatures higher than 700^o and dating by U-Pb in zircon has a blocking temperature of ca.800^o (Hoskin and Schaltegger, 2002), then it was a problem to assign a temperature to the ages obtained through this method. To solve this problem, the Ti in zircon thermometer was the option to determine the temperature of crystallization of zircon, hence, the temperature of metamorphism at 281 ± 3 Ma was found to be 556 ± 7^oC (Fig. 7.2).

Table 7.2: Thermochronology and blocking temperatures of minerals used in this study.# indicates that the value corresponds to the Ti-in-Zircon thermometer instead of the blocking temperature

Sample	Method	Age(My)	error(My)	Blocking T(^{o}C)	error (^{o}C)
FO-09-08	U-Pb zircon	281	3	556 #	7
Mica Schist	Ar-Ar white mica	263	1.2	350	50
FS-10-09	Ar-Ar biotite	251.4	1	300	40
FS-10-02	U-Pb titanite	243	26	630	30
Amphibolite	Ar-Ar hornblende	264	1.2	530	30

On the other hand, U-Pb dating of titanite performed on an amphibole sample (FS-10-02) has given an age of 243 ± 26 Ma. The scatter in this sample is large because this age is determined through a 3D concordia linear regression including 2σ. The closure temperature of this system is 630 ± 30^oC (Dickin, 2005). On the contrary, Ar-Ar dating in hornblende (data in Table 7.2) seems to be very precise with an age of 264 ± 1.2Ma (2σ) that can be related to a closing temperature of the system at 530 ± 30^oC (Rollingson, 1993).

The petrography of this amphibolite shows that titanite is abundant in the sample and appears in contact or as inclusions in hornblende; thus, these ages were expected to be similar. It was found through modeling of $\#Mg$ that hornblende in contact with rims in garnet (last paragenesis of the samples FS-10-16C and FO-09-07) formed at temperatures no lower than 590^oC. This temperature is higher than its Ar-Ar blocking temperature, so that the Ar-Ar age represents the time of exhumation where it passed that isotherm. On the other hand, titanite may form as a product of retrograde metamorphism (Deer et al., 1993) then assigning a temperature to the age of metamorphism becomes a problem. Only based on textural relations, it is presumed that titanite formed after the crystallization of hornblende.

At the end, the error in the age of U-Pb dating in titanite is so large that includes the age (plus error) obtained from hornblende (Fig. 7.9b). Then these data can not produce a cooling history (it would have a heating gradient) but rather a range of ages that follow the metamorphic peak of the amphibolite unit.

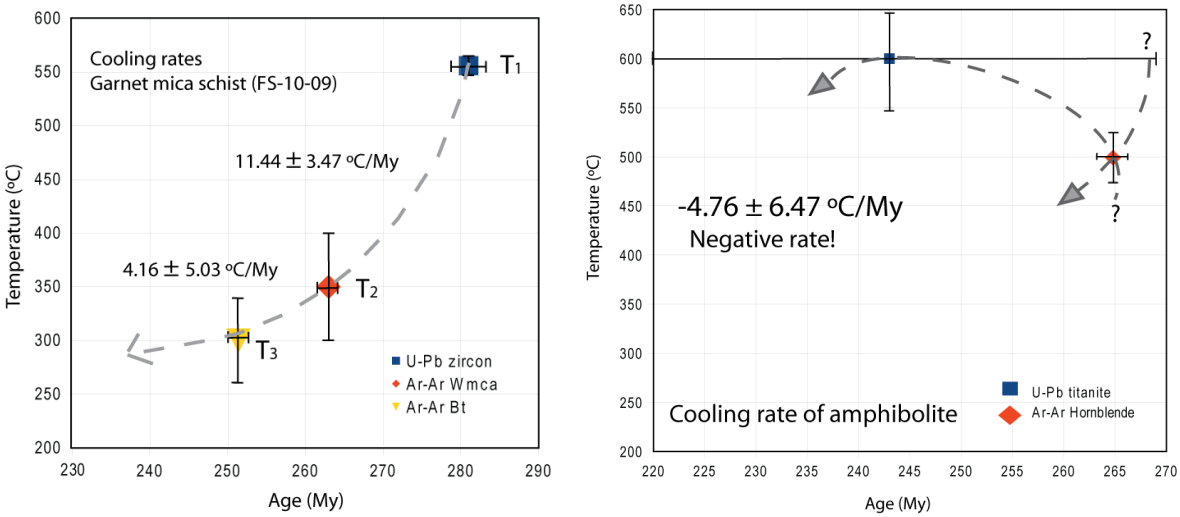

(a) Thermochronology of mica schist

(b) Thermochronology of amphibolite

Figure 7.9: a)Thermochronology and cooling rates of garnet mica schist sample FS-10-09. Ar-Ar systems consider closure temperatures whereas U-Pb in zircon considers temperature of crystallization determined by the *Ti-in-zircon* thermometer
b)Thermochronology of the amphibolite based upon U-Pb in titanite and Ar-Ar hornblende.

The cooling rates calculated could be calculated in the mica schist, where the first step ($T_{zr} \rightharpoonup T_{wmca}$) indicates a rate of $11.4 \pm 3.47^oC/My$ and a second step ($T_{wmca} \rightharpoonup toT_{bt}$) of $4.16 \pm 5.03^oC/My$. These rates are plot in Figure 7.9.

With these values and using a normal crust geothermal gradient of $25^oC/km$ (Ernst, 2009) calculated from the PT conditions of formation of garnet rims, the estimated exhumation rates are the following for the mica schist:

- $T_{zr} \rightharpoonup T_{wmca}$: 0.45 mm/yr
- $T_{wmca} \rightharpoonup T_{bt}$: 0.16 mm/yr

These rates are comparable to the ones obtained by Willner et al. (2004) through apatite fission track analysis for the Paleozoic accretionary complexes in central Chile (particularly in the Pichilemu area). They report rates of 0.25 mm/yr to 0.05 mm/yr, where the rates above 0.1 mm/yr are assigned to basal accretion who suggest that erosion in a tectonically

active area is an important unroofing process. The slower rates (less than 1 mm/yr) are related to gravitational isostatic compensation processes (Willner et al, 2004).

Uplift rates in the Altiplano-Puna are 0.2-0.3 mm/yr since the Miocene (Gregory-Wodzicki, 2000). According to the same author, there is a significant component of uplift due to erosion-driven isostatic rebound rather than mean surface uplift.

This work postulates the collision of a small terrane (or island arc), that based upon the models of Santosh et al, (2010) and Ernst (2005) would have provoked the exhumation of deep crustal levels through the suture zone: in this case, the Limón Verde metamorphic Complex (LVMC) would have exhumed through this suture (Fig. 7.10). Besides the LVMC, the material lying on top of the terrane that collided would have would be uplifted, for instance: deep marine sediments and turbidites, with little or no metamorphism, these units would be the Chañaral Mélange and, the Toco and Sierra del Tigre Formations (Bell, 1984).

During the last stages of collision, the oceanic slab will break off from the continental slab due to the gravity pull towards the mantle and its difference in density (continental crust is buoyant compared to oceanic crust (Burov et al. 2012). The breakoff, would create a rebound effect, similar to the 'coseismic' process that happens during an earthquake (Pardo, M. 2013 personal communication).

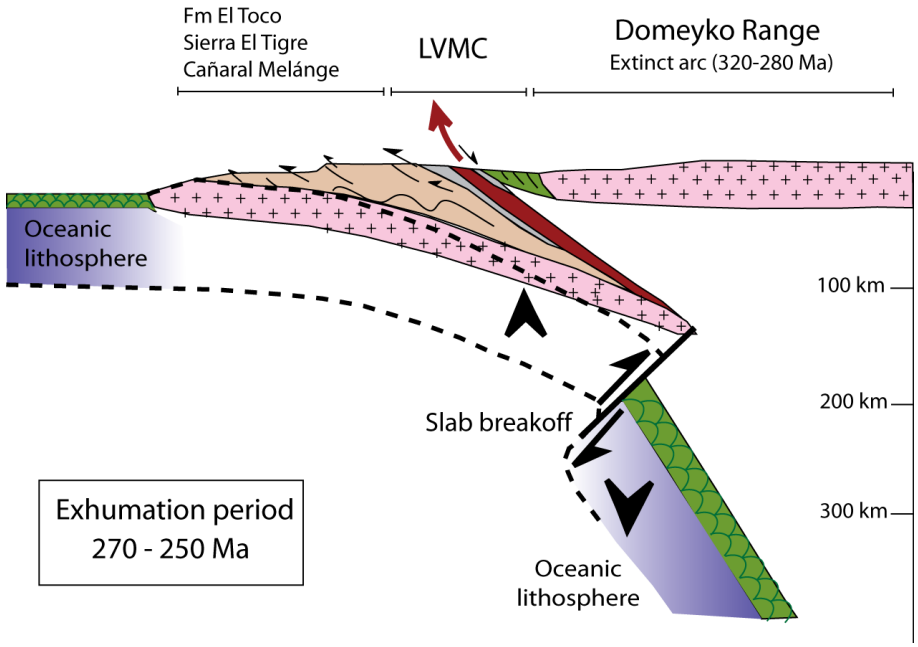

Figure 7.10: Exhumation model (modified after Santosh, et al. (2010)

It is normal for a collision zone to have a deformed ophiolite belt to mark the suture,

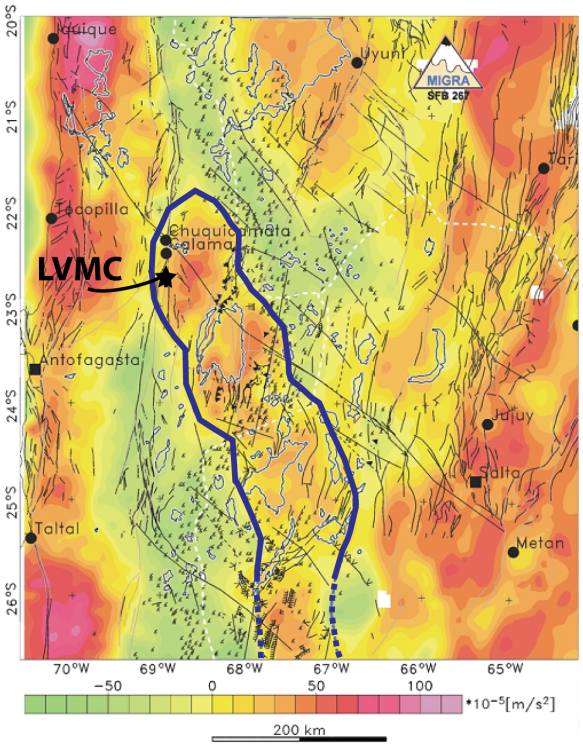

Figure 7.11: Isostatic residual gravity anomaly of the Central Andean Gravity High (CAGH), highlighed in blue (Gotze and Krausse, 2002).

an example of this is the Guarguarás Complex in Argentina, that would mark the suture of *Chilenia* (Massonne and Calderón, 2008). In the LVMC, it is not the case, because currently there is no visible evidence of the existance of an exotic terrane. However, an ultramafic crust has a density much higher than its surrounding continental crust; Götze and Krause (2002) postulate that the Andean Gravity High is an isostatic residual anomaly, and may indicate a relict of a subduction complex.

Tomlinson and Blanco (2010) postulate that the mechanism of exhumation of the rocks from the LVMC is through a *core complex* making an analog with the Laramide Orogen in southwest North America (Tomlinson, et al. 2012) in an extensional setting. This mechanism exhumes a large amount of material: hundreds of kilometers of deep crustal material (HP-UHP) where it is not the case in this area (Vernon and Clarke, 2008; Burov et al., 2012). In fact, one important characteristic of the LVMC is its size because it is very small (2 x 4 km of outcrop) and has no other rocks with the same genesis (depth of formation) in the area. Therefore, the hypothesis of the core complex as a way of exhuming these rocks is not favored here. On the other hand, thermo-mechanical numerical models by Burov, et al. (2012) on continental subduction and exhumation suggest collision as the most reliable mechanism to exhume HP-UHP units.

With the cooling rates obtained for the mica schist the time of exhumation can be constrained. If the rate obtained between $T_2 \rightharpoonup T_3$: 0.16 mm/yr (closure temperatures in Ar-Ar of white mica and biotite respectively) would have persisted unchanged, it would have taken 72 My to reach zero degrees, i.e. the mica schist would have been at the surface at 179 Ma during the lower Jurassic.

The global tectonic setting at ca. 250 Ma was that of a the supercontinent Pangea as seen in Figure 7.12, with a halt in subduction (Charrier et al., 2007; Ramos, 2008) where the Limón Verde Metamorphic Complex would be set in the western margin of Pangea what Cawood and Buchan (2007) call as the *Terra-Australis Orogen*.

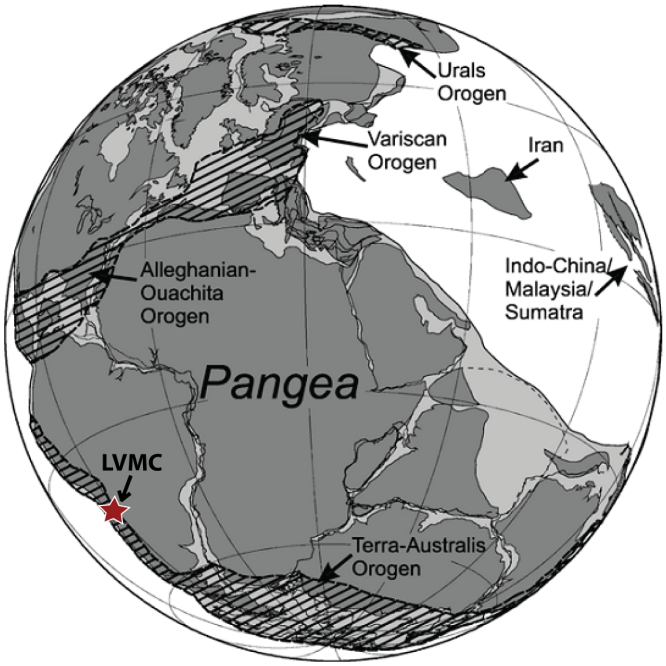

Figure 7.12: Global tectonic setting at 250 Ma with the Limón Verde Metamorphic Complex (LVMC) as part of the Terra Australis Orogen (Modified after Cawood and Buchan, 2007).

Previous authors set the end of exhumation and complete denudation of the LVMC at ca. 230 Ma. because a sedimentary unit assigned to the Late Triassic by previous authors lies unconformably over the mica schists (Baeza and Venegas, 1985; Marinovic, N. 1994). This suggests that the cooling rate increased. The age of this sedimentary unit is under revision (Duhart, 2013 *personal communication*), and until there is no reliable data (fission tracks in apatite from the LVMC or detrital zircon analysis in the sedimentary unit) the uplift and exhumation history will remain undetermined.

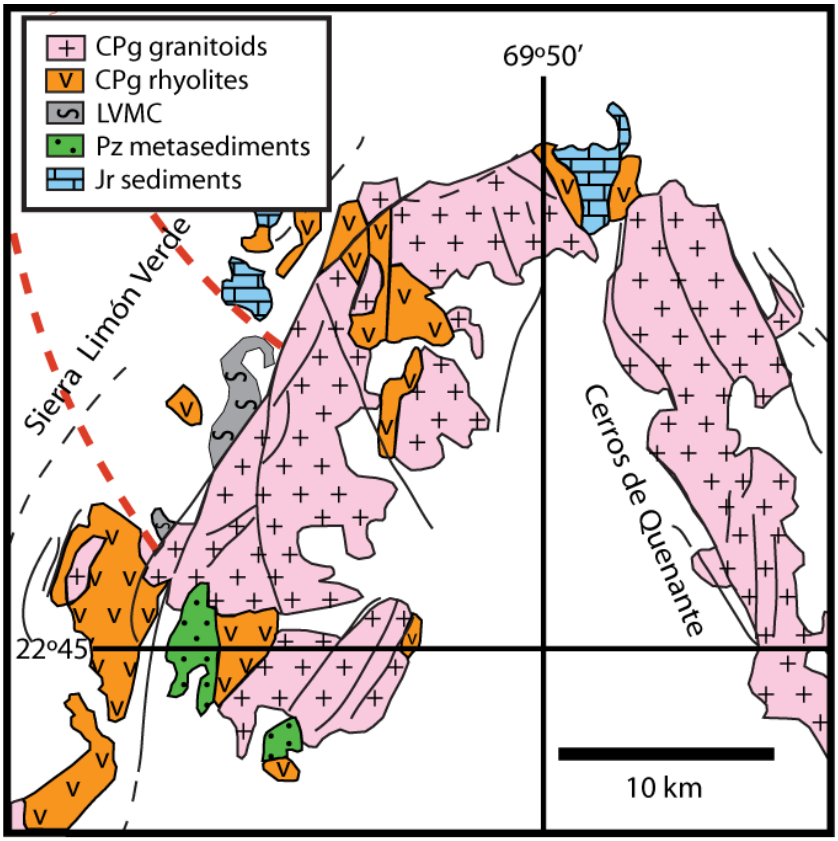

Figure 7.13: Limón Verde Range and geological units. This work postulates a major NW fault that puts in contact deep basement rocks with sedimentary units, the fault was active during the Triassic. Map based on Morandé, et al. 2012

7.5 Possible tectonic scenarios

In most of nothern and central Chile, there is a significant period of calc-alkaline magmatism during the late Carboniferous related to subduccion in the western margin of Gondwana (Lucassen et al. 1999; Charrier et al, 2004; Bahlburg et al. 2009). This period of continental convergence is called San Rafael-Gondwanide Orogeny in this region of South America. The Limón Verde Metamorphic Complex and its history suggest that it contributed to the accretionary process in that part of the margin. The rock assemblages present in the complex (amphibolites, mica schist and chert) suggest that these were part of an accretionary prism during the early metamorphic stages. With the current data available, there is no way of knowing whether if this was part of a frontal accretionary prism or a basal accretionary prism.

One of the definitions according to Bahlburg, et al. (2009) states that the mélanges occasionally contain mafic lavas of within-plate affinity and record at least two syn-sedimentary or two tectonic deformation events'. There is significant deformation of the rocks belonging to the complex, but the onset of deformation is poorly constrained because of the lack of structural data. Currently, only a NW trend in foliation and lineations of foliated rocks is seen in some outcrops, on top of that, there are many directions with no clear trend in the rest of the complex. In order to determine the deformation events, a thorough study of the structures in the complex in a 1:5000 scale is suggested.

Considering a continental geotherm, at ca. 263 Ma the mica schists were already at 3 kbar. If we consider a colder geothermal gradient, such as the one of a subduction zone (15C/Km) then, the mica schist would have been at ca. 7 kbar (21 km). This reasoning is actually not that far, from what it is obtained in the amphibolite sample. If the LVMC is considered as a structural unit by itself, it is logical for both rocks to have similar trajectories, but not be completely contemporaneous.

Three possible scenarios have been created to explain the tectonometamorphic history of the Limón Verde Metamorphic Complex, these are:

7.5.1 Scenario A

1. A forearc basin and within plate basalts (WPB) intruding the floor of the forearc basin to create the protolith

2. Subduction erosion to get protoliths into the channel, to later suffer subduction zone metamorphism (HP-LT)

3. Collision of an 'X'-like terrane to exhume the metamorphic rocks of the LVMC.

- Strenghts of the scenario: Can explain the PT gradients of metamorphism and its a plausible and efficient mechanism for exhumation of deep crustal rocks. Also the collision of a body would be supported by the migration of the magmatic arc to the west.

- Flaws of the scenario: There is no evidence of an exotic terrane. It can not explain the difference of 20 My. of metamorphism in the different rock units.

7.5.2 Scenario B

1. A forearc basin and simultaneous subduction erosion to bring down the sediments of the forearc onto the subduction channel.

2. Subduction erosion to get protoliths into the channel, to later suffer subduction zone metamorphism (HP-LT)

3. Collision of an island with within-plate basalt (WPB) material, of which, parts subducted down the channel, then the final collision exhumed the material.

- Strenghts of the scenario: Can explain the PT gradients of metamorphism and its a plausible mechanism for exhumation of deep crustal rocks. The subducting material and remobilization of an amphibolite slab may account for the anti-clockwise path of one of the (amphibolite) samples and the difference in ages between the different rock units.

  Also the collision of an exotic body would be supported by the migration of the magmatic arc to the west.

- Flaws of the scenario: There is no evidence of an exotic terrane.

7.5.3 Scenario C

1. A forearc basin and within plate basalts (WPB) in the floor of the forearc, basically a marginal basin.

2. Clossure of the marginal basin, creating the setting of metamorphism for the LVMC.

3. The complete clossure of the basin would extrude the LVMC.

- Strenghts of the scenario: It is fairly simple and does not need the collission of an exotic terrane to exhume the rocks.

- Flaws of the scenario: the geothermal gradients recorded at the cores of garnets are 12 and 15^{o}C/km. These gradients are only possible to achieve in a subduction zone where the isotherms are deviated from that of a normal crust of 25^{o}C/km (Ernst, 2009).

7.6 Sources of error and recommendations for future work

There are several sources of error in the present work, and something to take into account is that the sources of error are cumulative because many conclusions rely on data interpreted from other data. A good example is that, a 'garnet core-to-rim isopleth intersection' calculation relies on both modeling of the pseudosection with near-arbitrary parameters (like oxygen fugacity and amount of free water) and also on a structural formula calculated from electron microprobe data.

The sources of error can be summarized as:

- Analytical errors ('machine' errors, standards and detection limits)
- Error propagation due to modeling parameters (different use of constants, errors on analysis and grid refinement)
- State of the art (there are new experimental calibrations continuously appearing in the literature)

One important part of this study that was not completely understood is the Sm-Nd dating: the ages of metamorphism obtained with the garnet-whole rock isochron method are at least 100 My older than the ones obtained through U-Pb SHRIMP in zircon. This has been explained by an excess of Nd in the garnet at the time of growth, leaving a signature in the REE patterns in zircon crystallization. The explanation about involving Nd partitioning in zircon and garnet, and how it may make the age of metamorphism older in Sm-Nd studies is only valid for the mica schist. The garnet amphibolite sample also has an age of metamorphism ca. 380 Ma, there is no zircon to release Nd into the system. The second attempt of dating with Sm-Nd, gave an isochron age of 380 ± 21 for the garnet amphibolite, and 375 ± 13 for the garnet mica schist. These have MSWD values of 2.0 and 0.86 respectively, suggesting that they are reliable ages. There is an alternate option that may suit this results, which consists of the fact that these garnets may be detrital i.e. inherited from other sources indicating earlier events.

Exhumation rates are largely estimated: these were calculated under many assumptions, for instance, the value of the geothermal gradient for a normal crust was taken assuming

ideal conditions making a negative feedback cycle.

The structure of the LVMC is not know for certain, although previous authors state that these are intermixed slabs of rock, from a satellite image (not shown in this study), it is clear that the amphibolite unit is much more competent and has certain continuity in the outcrop. In this case, it is likely that the amphibolite unit followed a different exhumation path than the mica schist. Nevertheless, these seem to be part of the same orogenic event, and have similar characteristics of metamorphism. Therefore the realization of a 1:5000 structural map is suggested.

In terms of the tectonostratigraphic model, it does not account for the lack of continental basement or other crystalline rocks between the LVMC and the current coastline. The models are postulated in profile sections, that means, there is significant data to be added when taking into account the third (north-south) dimension; thus the geological interpretation of the area can be biased by this information. In order to determine the tectono-metamorphic history of this part of the country, thorough studies must be done in other basement rocks in this area.

Chapter 8

Conclusion

- The protoliths of the metamorphic units studied in this work correspond to a greywacke for the mica schist and a within-plate basalt for the amphibolite. Both rock types seem to have suffered crustal recycling processes.

- The maximum age of deposition of detrital zircon in the postulated depocenter is ca. 300 Ma, this age is similar to late stage magmatism from the Limón Verde Igneous Complex, or from the Rhyolites in the Cas Formation.

- The peak metamorphim of mica schist (P,T) was achieved in wet (ca. and above 5% H2O) conditions at ca. 280 Ma. according to U-Pb zircon ages. This is shown by textures of anatexis in some areas of the rock, and also in the REE patterns in zircon. Plus, it is reinforced by the PT realm of metamorphism modeled in the pseudosections at 14.5 kbar and ca. 600^{o}C, reaching to a max. temperature of ca. 650^{o}C. This is interpreted to be a depth of formation close to 50 kms.

- The peak metamorphic conditions of the amphibolite (P,T) were achieved also in wet conditions ca. 5% H2O and with high values of oxygen fugacity averaging 0.11%O_2 . The metamorphic peak of these samples are at a lower pressure(11.5 kbar), but similar temperature (650^{o}C) than the mica schist. Which is interpreted to a depth of formation of ca. 40 kms. On the other hand, the age of metamorphism is ca. 260 Ma. One of the amphibolite samples has an anti-clockwise path of metamorphism, which is interpreted to the remobilization of the slab.

- From only the mica schist samples it was possible to determine cooling rates. Two

steps were determined: $11.4 \pm 3.47^oC/My$ for the first step and $4.16 \pm 5.03^oC/My$ for a second. Considering the geothermal gradient of a normal continental crust (Ernst, 2009) of $25^oC/km$, the cooling rates are estimated exhumation rates of 0.45 mm/yr and 0.16 mm/yr respectively.

Therefore there are three possible geotectotic scenarios for the evolution of the LVMC:

1. Scenario A:

   -a forearc basin develops, with depocenter and thinning of the crust allowing the intraplate basalts to get closer to the surface.

   -these need to be subducted down the channel, indicating an erosive active margin,

   -after these reach peak metamorphic conditions, a small terrane (with continental crust) collides and extrudes slabs of the paleo-accretionary prism, creating a suture zone.

   -the ophiolite sequence characteristic of the collision zones, is not exposed in the area. Nevertheless, there is a positive gravity anomaly that can be interpreted as this rock type.

2. Scenario B:

   -zircon bearing sediments accumulate in the trench, and go down the subduction channel giving rise to the mica schists.

   -on top of the oceanic crust an extinct island arc approaches the continental margin where it collides.

   -this mechanism may account for the different pressures and age of metamorphism between rock types. Mica schist highest pressure is at 14.6 kbar whereas, the amphibolite highest pressure is at 11.7 kbar. The age of metamorphism is ca. 280 Ma for the mica schist, and ca. 260 Ma for the amphibolite.

   -due to the same collision, the mica schist and amphibolite extrude creating a suture zone.

   -the ophiolite sequence characteristic of the collision zones, is not exposed in the area. Nevertheless, there is a positive gravity anomaly that can be interpreted as this rock type.

3. Scenario C:

   -zircon bearing sediments accumulate in a forearc basin floored by within-plate basalts

   -there is a change in global tectonic conditions, then the marginal basin closes

   -closing of the marginal basin produces metamorphism and posterior extrusion of the LVMC.

In any case, it is necessary to consider a global tectonic setting where there is a high mantle activity, prior to the total amalgamation of Pangaea (Cawood and Buchan, 2007; Götze and Krause, 2002).

The postulated terrane and/or volcanic island is probably one of the last terranes amalgamated to this part of the continent as part of the Gondwanan Cycle and has a similar history than the X terrane.

Bibliography

ALLABY, M. 2008. Dictionary of Earth Sciences. Oxford Paperback Reference S. London, England.

ÁLVAREZ, J., MPODOZIS, C., ARRIAGADA, C., ASTINI, R., MORATA, D., SALAZAR, E., VALENCIA, V.A. and VERVOORT, J.D. 2011. Detrital zircons from late Paleozoic accretionary complexes in north-central Chile ($28^o - 32^o$S): Possible fingerprints of the Chilenia terrane. Journal of South American Earth Sciences. Vol.32, 4:460-476.

BAEZA, L., 1984. Petrography and Tectonics of the Plutonic and Metamorphic Complexes of Limon Verde and Mejillones Peninsula, Northern Chile. Dissertation zur Eerlangung des Grades eines Doktors der Naturwissenschaften der Geowissenschafltlichen Fakultät der Ebernhard-Karls-Universität Tübingen.

BAEZA, L. y VENEGAS, R. 1984. El basamento cristalino de la Sierra Limón Verde, II^a región de Antofagasta: Consideraciones genéticas. Revista Geológica de Chile, 22:25-34.

BAHLBURG, H., VERVOORT, J.D., DU FRANE, A., BOCK, B., AUGUSTSSON, C. and REIMANN, C. 2009. Timing of crust formation and recycling in accretionary orogens: Insights learned from the western margin of South America. Earth Science Reviews Vol 97: 215-241.

BELL, C.M. 1984. Deformation produced by the subduction of a Palaeozoic turbidite sequence in northern Chile. Journal of the Geological Society, Vol. 101: 339-347.

BRANDELIK, A. 2008. CALCMIN^{TM}, an EXCEL^{TM} Visual Basic application for calculating mineral structural formulae from electron microprobe analyses. Computers and Geosciences. Vol. 35, Issue 7:1540-1551.

BRAUN, J., Van Der BEEK, P. and BATT, G. 2006 Quantitative Thermochronology. Cambridge University Press, UK.

BUROV, E., FRANCOIS, T. YAMATO, P. and WOLF, S. 2012. Mechanisms of continental subduction and exhumation of HP and UHP rocks. Gondwana Research. In Press.

CAWOOD, P.A. and BUCHAN, C. 2007. Linking accretionary orogenesis with supercontinent assembly. Earth Science Reviews, Vol. 82: 217-256.

CHARRIER, R., PINTO, L. and RODRIGUEZ, M.P. 2007. Tectonostratigraphic evolution of the Andean Orogen in Chile. Chapter Three, The Geology of Chile Ed. Teresa Moreno and Wes Gibbons. The Geological Society of London.

CHERNIAK, D.J. and WATSON, E.B. 2000. Pb diffusion in zircon. Chemical Geology, 172: 5-24.

CONNOLLY, J.A.D. 1990. Multivariable phase diagrams, an algorithm based on generalized thermodynamics. American Journal of Science 290(6):666-718.

CORFU, F., HANCHAR, J.M., HOSKIN, P.W.O. and KINNY, P. 2003. Atlas of Zircon Textures. Chapter 16 ZIRCON. Reviews of Mineralogy and Geochemistry Vol 53:183-214.

CORRIE, S., KOHN, M.J. and MARKLEY, C. 2012. Zirconium partitioning in metamorphic minerals and growth of metamorphic zircon. American Geophysical Union Fall Meeting. San Francisco. Poster.

DEER, W.A., HOWIE, R.A. and ZUSSMAN, J. 1992. An introduction to The Rock-Forming Minerals II edition. Pearson London. UK.

DICKIN, A.P. 2005. 2nd Edition Radiogenic Isotope Geology. Cambridge University Press. United Kindom.

DUCEA, M.N., GANGULY, J., ROSENBERG, E.J., PATCHET, P.J. CHENG, W. and ISACHSEN, C. 2003. Sm-Nd dating of spatially controlled domains of garnet single crystals: a new method of high temperature thermochronology.

ERNST, W.G. 2005. Alpine and Pacific Style of Phanerozoic Mountain Building: subduction-zone petrogenesis of continental crust. Terra Nova Vol. 17:165-188.

ERNST, W.G. 2009. Subduction-zone metamorphism, calc-alkaline magmatism, and convergent-margin crustal evolution. Gondwana Research, Vol 18, Issue 1:8-16.

GARCÍA, A. 2012. Curso metamorfismo como herramienta geodinámica [online] `http://www.ugr.es/~agcasco/personal/` [seen on: January, 2013].

GREGORY-WODZICKI, K. 2000. Uplift history of the Central and Northern Andes: A review. GSA Bulletin. Vol. 112, No. 7:1091-1105.

GÖTZE, H-J. and KRAUSE, S. 2001 The Andean gravity high, a relict of an old subduction complex? Journal of South American Earth Sciences, Vol 14: 799-811.

HAWTHORNE, F.C. and OBERTI, R. 2007 Classification of Amphiboles. Reviews in Mineralogy and Geochemistry. Vol. 67, pp. 55-88.

HELLMAN, P.H. and GREEN, T.H. 1979 The role of sphene as an accesory phase in the high-pressure partial melting of hydrous mafic compositions. Earth and Planetary Science Letters. Vol. 42, Issue 2: 191-201.

HERVÉ, F., MUNIZAGA, F., MARINOVIC, N., HERVÉ, M., KAWASHITA, K., BROOK, M. and SNELLING, N. 1985 Geocronología Rb-Sr y K-Ar del basamento cristalino de la Sierra Limón Verde, Antofagasta, Chile. In Congreso Geológico Chileno, No. 4. Antofagasta.

HERVÉ, F. 1982 Condiciones de formación de complejos metamórficos chilenos a partir de la química de anfíbolas en metabasitas. 3er Congreso Geológico Chileno, II, pp. D93-D115.

HERVÉ, F., FAUNDEZ, V., CALDERÓN, M., MASSONNE, H-J. and WILLNER, A. 2007 Metamorphic and plutonic basement complexes. Chapter Two, The Geology of Chile Ed. Teresa Moreno and Wes Gibbons. The Geological Society of London.

JANSSEN, C., HOFFMANN-ROTHE, A., TAUBER, S. and WILKE, H. 2002. Internal structure of the Precordilleran fault system (Chile) - insights from structural and geophysical observations. Journal of Structural Geology, Vol. 24: 123-143.

KLEIMAN, L. and JAPAS, M.S. 2009. The Choiyoi volcanic province at $34^oS - 36^oS$ (San Rafael, Mendoza, Argentina): Implications for the Late Palaeozoic evolution of the southwestern margin of Gondwana. Tectonophysics Vol. 473:283-299.

KOHN, Matthew J. 2009. Model of garnet differential geochronology. Geochimica et Cosmochimica Acta 73:170-182.

KUKOWSKI, N. and ONCKEN, O. 2005. Subduction Erosion - the 'Normal' Mode of Fore-Arc Material Transfer along the Chilean Margin? Chapter Ten, The Andes Ed. Oncken, O., Chong, G., Franz, G., Giese, P., Götze, H-J., Ramos, V. and Wigger, P.

LOCOCK, Andrew J. 2008. An Excel spreadsheet to recast analyses of garnet into end-member components, and a synopsis of the crystal chemistry of natural silicate garnets. Computers and Geosciences 34: 1769-1780.

LUCASSEN F., FRANZ, G. and LABER, A. Permian high pressure rocks- the basement of the Sierra de Limón Verde in Northern Chile. Journal of South American Earth Sciences 12:183-199. 1999.

LUCASSEN, F., BECCHIO, R., WILKE, H.G., FRANZ, G., THIRLWALL, M.F., VIRAMONTE, J. and WEMMER, K. 2000. Proterozoic-Paleozoic development of the basement of the Central Andes ($18^o - 26^oS$)- a mobile belt of the South American craton. Journal of South American Earth Sciences, Vol. 13: 697-715.

LUDWIG, K. 2012. User's Manual for Isoplot 3.75, A geochronological tool kit for Microsoft Excel. Berkeley Geochronology Center Special Publication No. 5. Berkeley, CA.

MASSONNE, H-J. and CALDERÓN, M. 2008. P-T evolution of metapelites from the Guarguaraz Complex, Argentina: evidence for Devonian crustal thickening close to the western Gondwana margin. Revista Geológica de Chile, Vol. 35 (2): 215-231.

MASSONNE, H-J. 2012. Formation of Amphibole and Clinozoisite-Epidote in Eclogite owing to Fluid Infiltration during Exhumation in a Subduction Channel. Journal of Petrology, doi:10.1093.

MARINOVIC, Nicolas and LAHSEN, Alfredo. HOJA CALAMA. 1984 Servicio Nacional de Geología y Minería.

MORANDÉ, J., MPODOZIS, C., VALENCIA, V., ARRIAGADA, C. and MARQUARDT, C. 2012. Las Diamictitas de la Sierra Limón Verde, Antofagasta: Evidencias de Glaciación Neoproterozoica en el Norte de Chile?

MPODOZIS, C. and KAY, S. 1992. Late Paleozoic to Triassic evolution of the Gondwana margin: Evidence from Chilean Frontal Cordilleran batholiths (28^oSto31^oS). Geological Society of America Bulletin, v. 104: 999-1014.

NIEMEYER, Hans W. 1989. El Complejo Igneo-Sedimentario del Cordón de Lila, Región de Antofagasta: Significado Tectónico. Revista Geológica de Chile, 16(2): 163-181.

PARRISH, R.R. and NOBLE, S.R. 2003. Zircon U-Th-Pb Geochronology by Isotope Dilution-Thermal Ionization Mass Spectrometry (ID-TIMS). Chapter 3, ZIRCON. Reviews of Mineralogy and Geochemistry Vol 53: 183-214.

POWELL, R. and HOLLAND, T. 2010. Using equilibrium thermodynamics to understand metamorphism and metamorphic rocks. Elements Vol. 6, pp. 309-314.

RAMOS, V. A. 2008. The Basement of Central Andes: The Arequipa and Related Terranes. Annual Reviews of Earth and Planetary Sciences. 36:289-324.

ROLLINGSON, H. 1993. Using Geochemical Data: Evaluation, Presentation, Interpretation. Pearson, United Kindom.

SHAW, D.M. and KUDO, A.M. 1965. A test of the discriminant function in the amphibolite problem. Mineralogical Magazine Vol. 34:423-459.

SANTOSH, M., MARUYAMA, S., KOMIYA, T. and YAMAMOTO, S. 2010. Orogens in the evolving Earth: from surface continents to 'lost continents' at the core-mantle boundary. Geological Society, London, Special Publications v. 338: 77-116.

SILLITOE, R. H. 2010. Porphyry Copper Systems. Economic Geology Vol. 105: 3-41.

SPEAR, F.S. 1993. Metamorphic Phase Equilibria and Pressure-Temperature-Time Paths.

TOMLINSON, A. and BLANCO, N. 2002. Geología de la franja El Abra-Chuquicamata, II Región ($21^o45' - 22^o30'$). Informe registrado $IR - 07\#\#$. Servicio Nacional de Geología y Minería. Corporación Nacional del Cobre.

TOMLINSON, A., BLANCO, N., GARCÍA, M., BAEZA, L., ALCOTA, H., ALCOTA, H., LADINO, M. PÉREZ DE ARCE, C., FANNING, C.M. and MARTIN, M.W. 2012. Permian Exhumation of metamorphic complexes in the Calama area: Evidence for flat-slab subduction in northern Chile during the San Rafael tectonic phase and origin of the Central Andean Gravity High. In Congreso Geológico Chileno, No. 13. Antofagasta.

VERNON, R.H. and CLARKE, G.I. 2008. Principles of Metamorphic Petrology. Cambridge University Press. United Kindom.

WATSON, E.B., WARK, D.A. and THOMAS, J.B. 2006. Crystallization thermometers for zircon and rutile. Contributions to Mineralogy and Petrology, Vol. 151: 413-433.

WILLNER, A.P., THOMSON, S.N, KRONER, A., WARTHO, J., WIJBRANS J.R. and HERVÉ, F. 2005. Time Markers for the Evolution and Exhumation History of a Late Paleozoic Paired Metamorphic Belt in North-Central Chile (34-35 30'S). Journal of Petrology Vol. 46, 9:1835-1858.

WU, C-M. and ZHAO, G. 2006. Recalibration of the Garnet-Muscovite (GM) Geothermometer and the Garnet-Muscovite-Plagioclase-Quartz (GMPQ) Geobarometer for Metapelitic Assemblages. Journal of Petrology, Vol. 47, No. 12, pp. 2357-2368.

Appendix A

Nomenclature

Table A.1: Mineral abbreviations used in this thesis document. In this list mineral names are arranged in alphabetical order. This nomenclature is based upon the IUGS Subcomission on the Systematics of Metamorphic Rocks: Web version 01.02.07.

Mineral name	Abbreviation	Mineral name	Abbreviation
Actinolite	Act	Limonite	Lm
Albite	Ab	Magnetite	Mag
Alkali feldspar	Afs	Margarite	Mrg
Allanite	Aln	Mica	Mca
Almandine	Alm	Muscovite	Ms
Aluminosilicate	Als	Olivine	Ol
Annite	Ann	Omphacite	Omp
Anorthite	An	Opaque mineral	Op
Apatite	Ap	Orthoamphibole	Oam
Biotite	Bt	Paragonite	Pg
Calcite	Cal	Phengite	Phg
Carbonate	Cb	Phlogopite	Phl
Chlorite	Chl	Plagioclase	Pl
Chloritoid	Cld	Prehnite	Prh
Clinoamphibole	Cam	Pumpellyite	Pmp
Clinozoisite	Czo	Pyrope	Prp
Edenite	Ed	Quartz	Qtz
Epidote	Ep	Rutile	Rt
Feldspar	Fsp	Sericite	Ser
Garnet	Grt	Sillimanite	Sil
Graphite	Gr	Smectite	Sme
Grossular	Grs	Smectite	Sme
Hematite	Hem	Spinel	Spl
Hastingsite	Hs	Titanite	Ttn
Hornblende	Hbl	Ulvoespinel	Usp
Illite	Ill	White mica	wmca
Ilmenite	Ilm	Zeolite	Zeo
K-feldspar	Kfs	Zircon	Zrn
Kyanite	Ky	Zoisite	Zo

Appendix B

Electron Microprobe Analysis Data and Structural Formulae

For complete sets of electron microprobe data (spreadsheets with analyses and structural formule, BSE images and X-ray intensity maps) visit

`https://www.dropbox.com/sh/upm3e53ps45nn1g/5rm2rabhh4`.

Table B.1: Sumple number and corresponding parageneses of samples used in this study.

Sample number	Rock type	Paragenesis
FO-09-07	Grt-amphibolite	$Grt + Czo + Amp + Bt + Qtz \pm Ttn \pm Rt$
FO-09-08	Grt-mica schist	$Grt + Bt + Wmca + Qtz \pm Pl \pm Ttn \pm Rt$
FO-09-13	Grt-mica schist	$Grt + Czo + Wmca + Qtz + Pl \pm Rt$
FS-10-02	Amphibolite	$Amp + Czo + Qtz + Ttn \pm Rt$
FS-10-09	Grt-mica schist	$Grt + Bt + Wmca + Qtz \pm Ttn \pm Rt$
FS-10-16A	Grt-bt schist	$Grt + Czo + Bt + Czo + Pl + Qtz \pm Aln$
FS-10-16C	Grt-amphibolite	$Grt + Czo + Bt + Amp + Qtz \pm Ttn \pm Rt$

Table B.2: Representative analyses of garnet

X	FS09GT1-6	FS09GT1-20	FS16a-gt1-7	FS16a-#2	FS16a#12	FS16cgt1-23	FS16c-gt2#7	FS1016c-gt2#12
Na2O	0.008	0.007	0.02	0.02	0.04	0.00	0.02	0.07
SiO2	37.570	36.806	36.92	36.79	36.79	37.34	37.05	37.03
TiO2	0.048	0.070	0.10	0.12	0.02	0.08	0.12	0.11
Al2O3	21.277	21.071	21.44	21.21	21.53	21.46	20.98	20.62
V2O3	0.000	0.000	0.00	0.00	0.00	0.00	0.00	0.00
Cr2O3	0.000	0.000	0.00	0.00	0.00	0.00	0.00	0.00
Fe2O3	1.059	1.122	0.64	0.80	0.39	0.96	1.39	1.07
FeO	29.535	32.038	25.92	27.56	26.45	27.50	27.68	26.06
MnO	0.615	0.279	1.34	1.75	1.62	1.37	1.95	3.67
MgO	5.012	3.439	4.03	4.31	3.69	4.57	3.03	2.70
CaO	5.709	5.937	9.15	6.96	8.88	7.52	8.72	8.15
Na2O	0.000	0.000	0.00	0.00	0.00	0.00	0.00	0.00
Total	100.825	100.762	99.55	99.50	99.38	100.80	100.92	99.40
Si	5.808	5.733	5.7343	5.7476	5.7327	5.7397	5.7501	5.9004
Ti	0.006	0.008	0.0113	0.0141	0.0018	0.0096	0.0142	0.0134
sum4	5.814	5.742	5.7457	5.7617	5.7344	5.7493	5.7644	5.9139
Al	3.877	3.868	3.9248	3.9058	3.9542	3.8890	3.8381	3.8721
Fe3	0.123	0.132	0.0752	0.0942	0.0458	0.1110	0.1619	0.1279
sum6	4.000	4.000	4.0000	4.0000	4.0000	4.0000	4.0000	4.0000
Fe2	3.819	4.174	3.3669	3.6009	3.4463	3.5351	3.5934	3.4724
Mg	1.155	0.799	0.9340	1.0033	0.8578	1.0469	0.7001	0.6416
Ca	0.946	0.991	1.5224	1.1645	1.4817	1.2392	1.4501	1.3907
Mn	0.081	0.037	0.1767	0.2313	0.2142	0.1788	0.2563	0.4953
sum8	6.000	6.000	6.0000	6.0000	6.0000	6.0000	6.0000	6.0000
components								
grossular	0.158	0.165	0.2537	0.1941	0.2470	0.2065	0.2417	0.2318
pyrope	0.193	0.133	0.1557	0.1672	0.1430	0.1745	0.1167	0.1069
almandine	0.636	0.696	0.5612	0.6001	0.5744	0.5892	0.5989	0.5787
spessartine	0.013	0.006	0.0294	0.0385	0.0357	0.0298	0.0427	0.0826
xAl	0.969	0.967	0.9812	0.9764	0.9886	0.9723	0.9595	0.9680

Table B.3: Representative microprobe analyses of white mica

X	FS09wm5-6	FS09wm5-13	FS09wm4-18	FS16C-wm-grf1	FS16c2-wm3	FS16a-wm1-11	FS16awm1-20
SiO2	47.32	46.90	47.12	46.99	46.33	46.39	47.38
TiO2	1.03	0.53	0.96	0.56	0.51	0.69	0.62
Al2O3	32.44	33.12	32.12	33.59	33.12	32.34	32.08
FeO	1.46	1.34	1.43	1.29	1.27	1.37	1.42
MnO	0.01	0.02	0.02	0.00	0.07	0.01	0.02
MgO	2.03	1.76	2.00	1.78	1.74	1.97	2.04
CaO	0.00	0.00	0.00	0.02	0.01	0.00	0.03
Na2O	0.94	1.35	1.14	1.55	1.43	1.14	1.11
K2O	9.75	9.38	9.54	9.42	9.03	9.47	9.07
BaO	0.39	0.44	0.45	0.55	0.51	0.63	0.54
F-	0.05	0.21	0.04	0.00	0.16	0.01	0.23
H2O	4.48	4.38	4.45	4.51	4.37	4.42	4.36
Total_corr.	99.88	99.32	99.25	100.26	98.46	98.43	98.81
Si	6.297	6.277	6.316	6.248	6.249	6.282	6.352
Al_T	1.703	1.723	1.684	1.752	1.751	1.718	1.648
sum4	8.000	8.000	8.000	8.000	8.000	8.000	8.000
Al_O	3.386	3.501	3.391	3.512	3.515	3.443	3.420
Ti	0.103	0.053	0.097	0.056	0.052	0.070	0.063
Fe2	0.162	0.150	0.161	0.144	0.143	0.155	0.159
Mn	0.001	0.002	0.002	0.000	0.008	0.001	0.002
Mg	0.403	0.352	0.400	0.353	0.350	0.398	0.407
sum6	4.055	4.058	4.050	4.064	4.066	4.067	4.051
Ca	0.001	0.000	0.000	0.003	0.001	0.000	0.004
Ba	0.021	0.023	0.023	0.029	0.027	0.033	0.028
Na	0.241	0.349	0.296	0.401	0.375	0.300	0.289
K	1.656	1.601	1.632	1.598	1.554	1.637	1.551
sum8	1.918	1.973	1.952	2.031	1.957	1.970	1.872
F	0.021	0.090	0.018	0.000	0.069	0.004	0.098
Cl	0.000	0.000	0.000	0.000	0.001	0.000	0.001
H	3.979	3.910	3.981	4.000	3.930	3.996	3.902
Components							
MUSCOVITE	0.624	0.606	0.593	0.587	0.596	0.604	0.578
WM_PHLOGOPITE	0.028	0.029	0.025	0.032	0.033	0.034	0.026
AL_CELADONITE	0.114	0.105	0.121	0.099	0.099	0.114	0.139
FE_AL_CELADONITE	0.046	0.045	0.049	0.040	0.040	0.044	0.054
PARAGONITE	0.126	0.177	0.152	0.197	0.192	0.152	0.155
Si pfu	3.149	3.138	3.158	3.124	3.125	3.141	3.176

Table B.4: Representative microprobe analyses of biotite

X	FS09bt4-20	FS09bt3-18	FS16c-bt1-2	FS16C-bt-6	FS16C-bt-8	FS16a-bt2-13	FS16a-bt2-23
SiO2	36.06	36.68	37.36	37.17	37.20	36.48	35.99
TiO2	1.94	1.54	1.61	1.53	1.53	2.55	1.81
Al2O3	16.87	17.12	17.09	17.78	17.07	16.64	16.96
FeO	17.28	15.92	14.29	15.25	15.34	16.83	16.11
MnO	0.21	0.17	0.10	0.20	0.08	0.21	0.19
MgO	11.62	12.86	14.29	12.92	13.47	11.64	12.64
CaO	0.06	0.03	0.03	0.13	0.01	0.04	0.03
Na2O	0.08	0.18	0.16	0.20	0.14	0.11	0.18
K2O	8.98	9.05	9.29	8.58	9.40	9.82	9.32
BaO	0.12	0.23	0.27	0.23	0.24	0.17	0.32
F-	0.22	0.00	0.02	0.00	0.00	0.02	0.18
Cl-	0.01	0.00	0.00	0.00	0.00	0.00	0.00
H2O	3.78	3.94	4.00	3.98	3.98	3.92	3.82
Total_corr.	97.14	97.71	98.49	97.97	98.46	98.43	97.48
Si	2.78	2.79	2.80	2.80	2.80	2.78	2.76
Al_T	1.22	1.21	1.20	1.20	1.20	1.22	1.24
Ti	0.11	0.09	0.09	0.09	0.09	0.15	0.10
Al_O	0.31	0.32	0.31	0.37	0.32	0.28	0.29
Fe2	1.11	1.01	0.89	0.96	0.97	1.07	1.03
Mn	0.01	0.01	0.01	0.01	0.01	0.01	0.01
Mg	1.34	1.46	1.60	1.45	1.51	1.32	1.45
sum6	2.89	2.89	2.89	2.88	2.89	2.83	2.89
Na	0.01	0.03	0.02	0.03	0.02	0.02	0.03
K	0.88	0.88	0.89	0.82	0.90	0.96	0.91
Ba	0.00	0.01	0.01	0.01	0.01	0.01	0.01
sum8	0.90	0.91	0.92	0.87	0.93	0.98	0.95
H	1.95	2.00	2.00	2.00	2.00	1.99	1.96
components							
xAl	0.16	0.16	0.15	0.19	0.16	0.14	0.15
X Mg	0.55	0.59	0.64	0.60	0.61	0.55	0.58
Al T (12O)	2.44	2.42	2.41	2.41	2.40	2.44	2.48

Table B.5: Representative microprobe analyses of clinozoisite in sample FS10-16A

X	FS10-16a-czo-10	FS10-16a-ep2-3	FS10-16a-czo-1-5	FS10-16a-czo-10
SiO2	38.00	36.64	37.56	37.83
TiO2	0.09	0.17	0.27	0.05
Al2O3	32.61	28.85	28.50	32.37
Fe2O3	1.37	5.48	6.78	1.42
Mn2O3	0.00	0.11	0.10	0.00
MgO	0.04	0.17	0.06	0.01
CaO	24.62	21.90	23.83	24.37
Na2O	0.02	0.00	0.01	0.02
H2O	1.94	1.85	1.91	1.93
Total	98.69	95.18	99.02	97.99
Total_corr.	98.69	95.18	99.02	97.99
Si	2.9360	2.9632	2.9471	2.9425
Ti	0.0049	0.0102	0.0161	0.0026
Al	2.9693	2.7496	2.6359	2.9672
Fe3	0.0795	0.3336	0.4004	0.0833
Mn3	0.0000	0.0065	0.0058	0.0000
Mg	0.0050	0.0207	0.0064	0.0014
sum6	3.0587	3.1206	3.0646	3.0546
Ca	2.0383	1.8979	2.0034	2.0312
Na	0.0034	0.0000	0.0014	0.0027
sum8	2.0417	1.8979	2.0047	2.0339
H	1.0000	1.0000	1.0000	1.0000

Table B.6: Representative analyses of feldspar

X	02-flds-4	02-flds-4	16C-flds-7	16C-flds-1	FS16a-fld1-10	FS16a-flds-26
SiO2	64.69	62.51	64.68	63.85	60.79	64.07
Al2O3	18.00	23.40	18.15	22.58	23.70	21.87
Fe2O3	0.16	0.37	0.44	0.00	0.04	0.02
MgO	0.00	0.00	0.15	0.00	0.00	0.00
CaO	0.02	4.74	0.04	3.80	5.48	3.30
Na2O	0.18	9.22	0.16	9.92	8.56	9.73
K2O	16.65	0.08	16.26	0.09	0.06	0.05
BaO	0.33	0.00	0.36	0.00	0.00	0.00
Total	100.08	100.32	100.23	100.25	98.62	99.05
Si	3.00	2.76	2.99	2.82	2.74	2.85
Al	0.98	1.22	0.99	1.17	1.26	1.15
Fe3	0.01	0.01	0.02	0.00	0.00	0.00
su1	3.99	4.00	4.01	3.99	3.99	4.00
Ba	0.01	0.00	0.01	0.00	0.00	0.00
Ca	0.00	0.22	0.00	0.18	0.26	0.16
Na	0.02	0.79	0.01	0.85	0.75	0.84
K	0.99	0.00	0.96	0.01	0.00	0.00
su2	1.01	1.02	0.98	1.03	1.01	1.00
components						
Anorthite	0.01	0.22	0.01	0.17	0.26	0.16
High albite	0.02	0.78	0.01	0.82	0.74	0.84
K feldspar	0.98	0.00	0.98	0.00	0.00	0.00

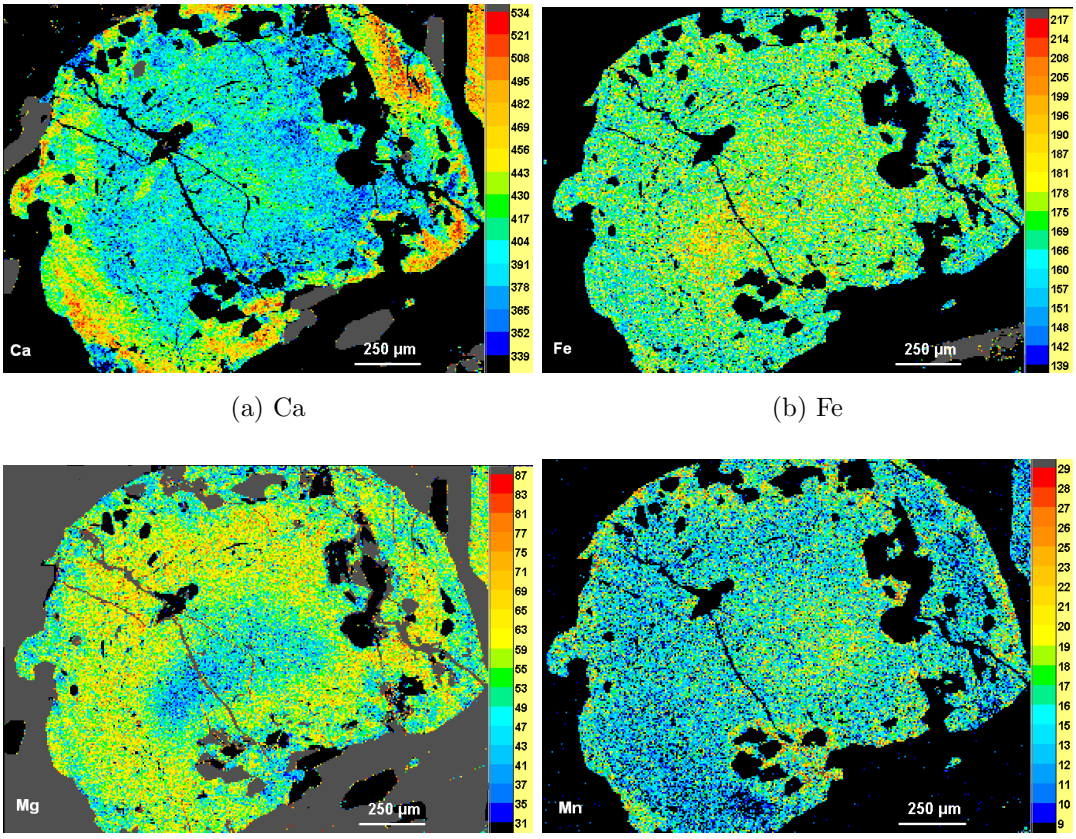

(a) Ca

(b) Fe

(c) Mg

(d) Mn

Figure B.1: Elemental maps for Garnet #1 in sample FS-10-16A, for the elements Ca, Fe, Mg and Mn

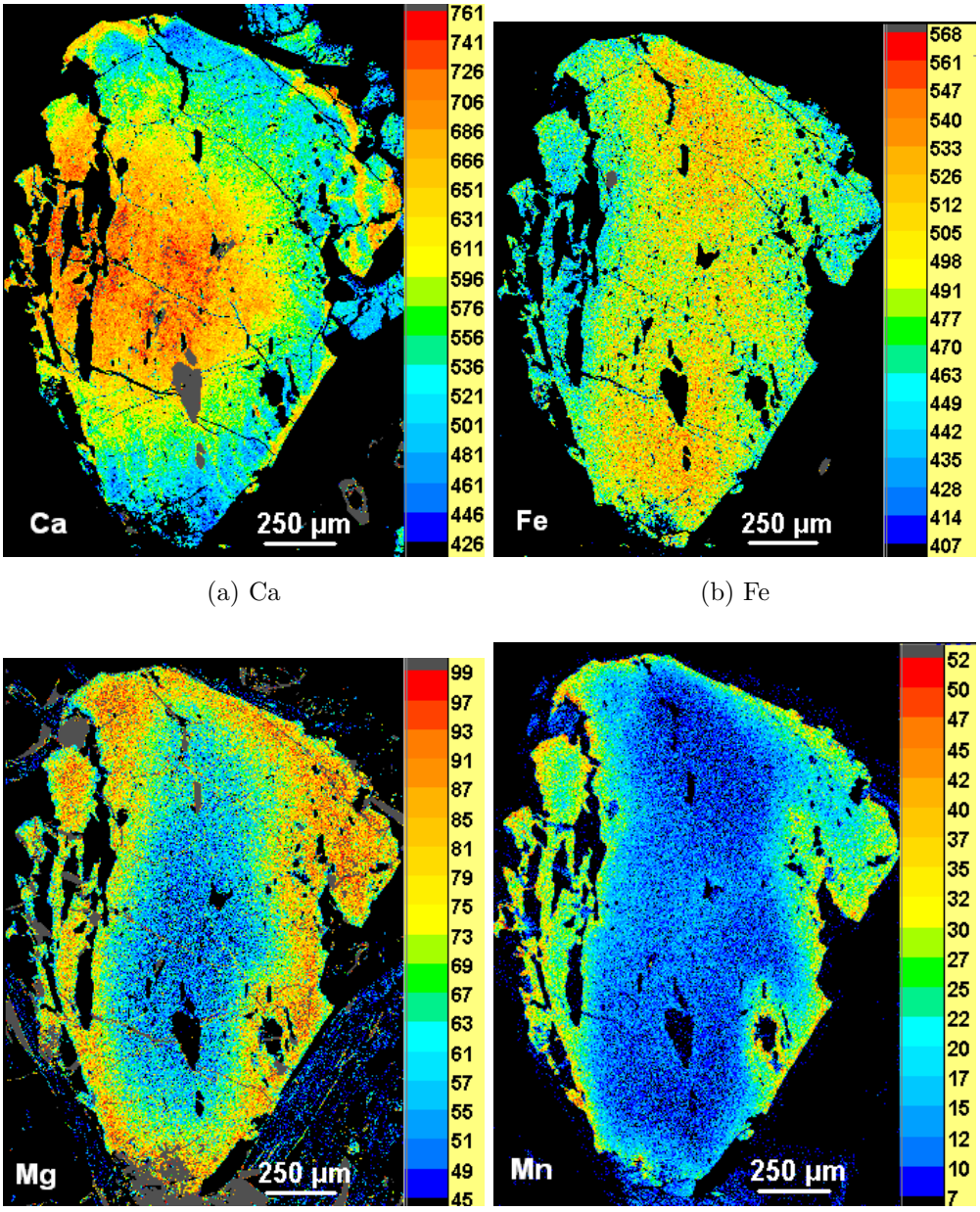

(a) Ca

(b) Fe

(c) Mg

(d) Mn

Figure B.2: Elemental maps for Garnet #1 in sample FS-10-09, for the elements Ca, Fe, Mg and Mn

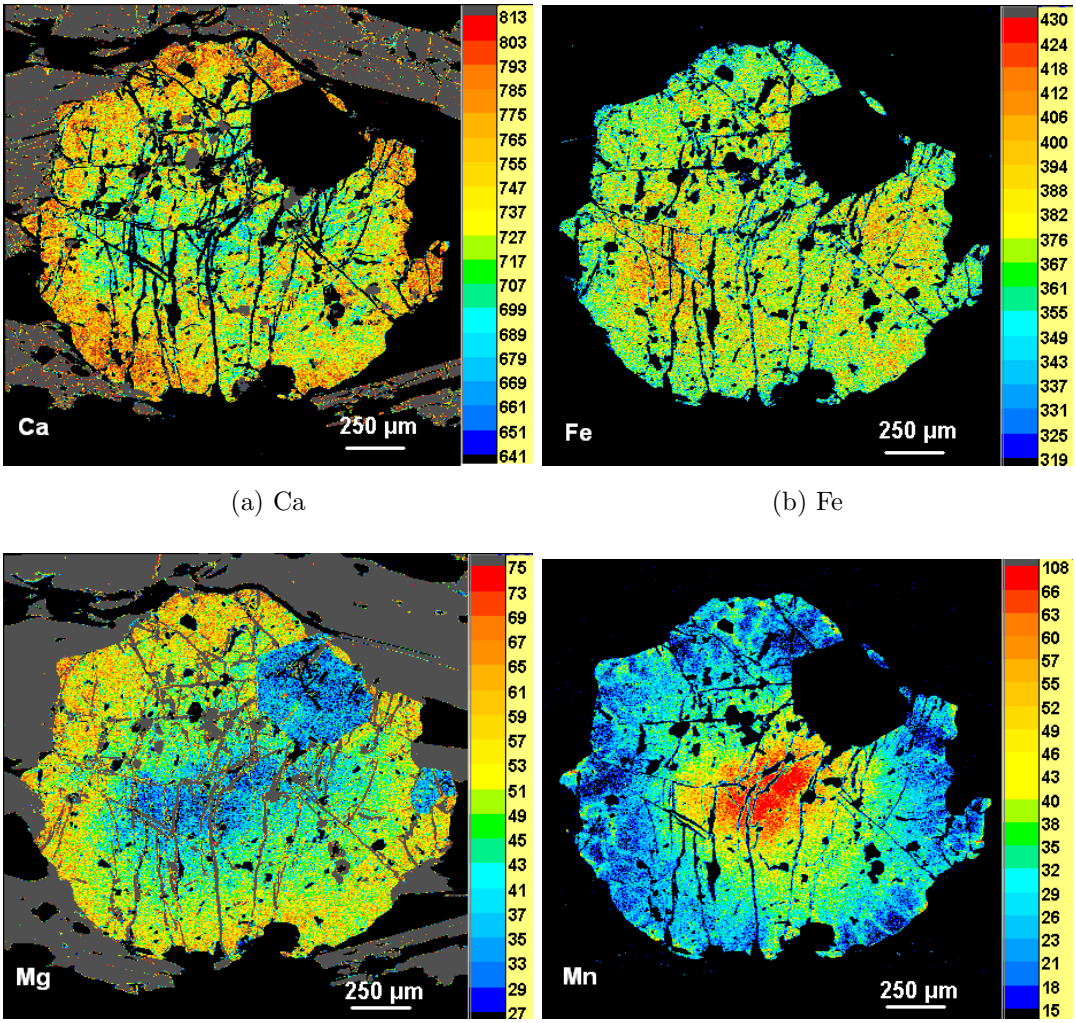

(a) Ca (b) Fe

(c) Mg (d) Mn

Figure B.3: Elemental maps for Garnet #2 in sample FS-10-16C, for the elements Ca, Fe, Mg and Mn

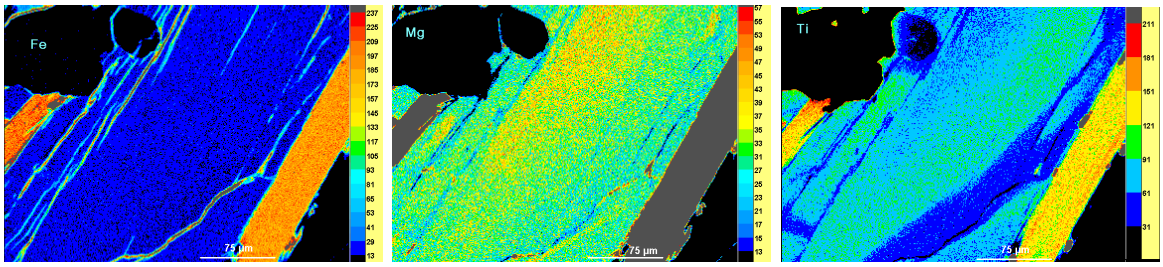

(a) Fe (b) Mg (c) Ti

Figure B.4: Elemental maps for Phengite #1 in sample FS-10-09, for the elements Fe, Mg and Ti

Appendix C

Generic script for PerpleX calculations

```
hp02ver.dat     thermodynamic data file
print    | print generates print output
plot     | no_plot suppresses plot output
solution_model1.dat     solution model file, blank = none
FS1016C_mar13
perplex_option.dat     computational option file
    5 calculation type: 0 - composition, 1 - Schreinemakers, 3 - Mixed, 4 - gwash,
    5 - gridded min, 7 - 1d fract, 8 - gwash 9 - 2d fract, 10 - 7 w/file input
    0 unused place holder, post 06
    0 unused place holder, post 06
    0 unused place holder, post 06
    0 unused place holder, post 06
    0 unused place holder, post 06
    0 unused place holder, post 06
    0 unused place holder, post 06
    0 unused place holder, post 06
    0 unused place holder, post 06
    0 number component transformations
   15 number of components in the data base
    1 component amounts, 0 - molar, 1 weight
    0 unused place holder, post 06
    0 unused place holder, post 06
    0 unused place holder, post 05
```

```
    0 ifug EoS for saturated phase
    2 gridded minimization dimension (1 or 2)
    0 special dependencies: 0 - P and T independent, 1 - P(T), 2 - T(P)
 0.00000      0.00000      0.00000      0.00000      0.00000
 Geothermal gradient polynomial coeffs.

begin thermodynamic component list
SIO2  1  53.2890    0.00000      0.00000     weight amount
TIO2  1  1.69200      0.00000      0.00000     weight amount
AL2O3 1  12.2050      0.00000      0.00000     weight amount
FEO   1  10.5880      0.00000      0.00000     weight amount
MGO   1  8.94000      0.00000      0.00000     weight amount
CAO   1  7.56800      0.00000      0.00000     weight amount
NA2O  1  1.23900      0.00000      0.00000     weight amount
K2O   1  1.20900      0.00000      0.00000     weight amount
MNO   1  0.15600      0.00000      0.00000     weight amount
O2    1  0.11800      0.00000      0.00000     weight amount
H2O   1  2.99700      0.00000      0.00000     weight amount
end thermodynamic component list

begin saturated component list
end saturated component list

begin saturated phase component list
end saturated phase component list

begin independent potential/fugacity/activity list
end independent potential list

begin excluded phase list
tip
tbi
qfm
mthm
zo
h2oL
ab
rieb
```

```
mrb
cumm
grun
ann1
mic
end excluded phase list

begin solution phase list
Gt(HP)
Stlp(M)
Opx(HP)
IlGkPy
MtUl(A)
Ctd(HP)
Carp
Pheng(HP)
Mica(M)
feldspar
Ep(HP)
Omph(HP)
GlTrTsPg
TiBio(HP)
Chl(HP)
end solution phase list

 15000.0   973.00   0.00000000  0.0000      0.0000     max p, t, xco2, u1, u2
   000.0   273.00   0.00000000  0.0000      0.0000     min p, t, xco2, u1, u2
 0.0000    0.0000   0.00000000  0.0000      0.0000     unused place holder post 06

 2  1  4  5  3   indices of 1st & 2nd independent & sectioning variables
```